Geometric Effects on Maximum Power Absorption Efficiency for a Single, Two-Dimensional Heaving Body

A THESIS SUBMITTED TO THE GRADUATE DIVISION OF THE UNIVERSITY OF HAWAI'I IN PARTIAL FULFILLMENT OF THE REQUIREMENTS FOR THE DEGREE OF

MASTER OF SCIENCE

IN

CIVIL ENGINEERING

August 2012

By

Rachael Hager

Thesis Committee:

Michelle H. Teng, Chairperson
R. Cengiz Ertekin
Gerard Nihous
Amarjit Singh

ACKNOWLEDGEMENTS

I would like to begin by saying how truly grateful I am for all those that have helped me along the way. To Professor Teng for her constant guidance and support. Professor Ertekin and Professor Nihous who have taken hours of their lives to teach me about waves. To Nelson Fernandez who has been my partner on the experimental side since the beginning, and Ame Masutomi who greatly contributed in the final stages of the experiment. A special thank you to Richard Carter who has been a mentor for me in both the theoretical and experimental aspects of this project. He has not only been a patient teacher, but an amazing friend. In general all those in the Hydraulics lab I would like to thank for their contributions to my project in the past two years. On the experimental aspect of the project I am thankful to Mitch Pinkerton, Austin Rogers, and Brian Kodama for not only their aid in setting up the experiment, but for their indispensable advice. On the numerical side of the project a very special thank you goes to Danny Lee and Dylan Hunt for their hours helping me with computer problems, without either of them the numerical work would never have even begun. I would like to thank Janis Kusatsu and Amy Fujishige for their great work. Thank you to the REIS program, in particular Professor Kuh and Robert McGehee for their continuous support. Additionally thank you to Dr. Luis Vega and the Hawaiian National Marine Renewable Energy Center for their continuous support.

In general, thank you to all my friends for their support and kindness. Thank you to Professor Chin Wu at the University of Wisconsin-Madison for his past advice and knowledge. A special thank you to Alvina Lutu-Perelini who has made me feel that I not only have a best friend in Honolulu, but a family. Finally, I would like to dedicate this thesis to my family; mother, Roberta Hager; father, Michael Hager; and brother, Tom Hager. There are not even words to show how grateful I am that they are in my life, but thank you.

ABSTRACT

Numerical simulations are carried out to study the effects of body geometry on maximum power absorption efficiency. Diffraction theory is used to study two-dimensional, single, surface-piercing, heaving bodies impinged by regular, harmonic, linear waves. The complex amplitude of the excitation force in the heave direction is calculated numerically using AQWA. Additionally, a wave flume experiment is proposed to measure the complex amplitude of the excitation force in the heave direction, in order to study the maximum power absorption efficiency.

From the complex amplitude of the excitation force (X_i), the radiated wave amplitudes at positive infinity (α_+) and negative infinity (α_-) are calculated using:

$$X_i = \frac{2\rho A \alpha g C_g i}{\omega}$$

The maximum power absorption efficiency for a given frequency is then calculated using:

$$\lambda = \frac{|\alpha_+|^2}{|\alpha_+|^2 + |\alpha_-|^2}$$

The radiated wave amplitude at positive infinity is calculated from the amplitude of the excitation force as a wave impinges the curved face of the body. Rotating the body 180° and measuring the amplitude of the excitation force yields the radiated wave amplitude at negative infinity.

Results indicate concave bodies experience the greatest excitation force and convex bodies yield the higher maximum power absorption efficiency, under the condition that the wavelength is relatively short and the draft and waterline cross-sectional area remain constant. For long waves, the geometric effect becomes insignificant.

Contents

LIST OF TABLES

Table **Page**

LIST OF FIGURES

Figure **Page**

NOMENCLATURE

A=incident wave amplitude
$\alpha_{+\infty}$= radiated wave amplitude at positive infinity in two dimensions
$\alpha_{-\infty}$= radiated wave amplitude at negative infinity in two dimensions
B =body length
B_{ij}=damping coefficient
C=phase velocity
C_g=group velocity
d=water depth
D = draft
ρ= water density
E=wave energy
F=total hydrodynamic force
F_D=diffraction force
F_I=Froude-Krylov force
F_H=hydrostatic force
F_R=radiated wave force
F_T=total force
F_w=excitation force
f_{ij}=complex force coefficient
g=gravitational acceleration
H=wave height
$i = \sqrt{-1}$
k=wave number
k_{ij}=hydrostatic stiffness
KE=kinetic energy
L=wavelength
λ=maximum power absorption efficiency
M_H=hydrostatic moment
M_T=total moment
M_W=excitation moment
M_{ij}=added-mass coefficient
m_{ij}=mass or mass moment
n=unit normal
η= water surface elevation
p_T=total fluid pressure
p_a=atmospheric pressure
P_{max}=maximum absorbed power
P_w=power flux of wave
PE=potential energy of wave
P=absorbed wave power
r=moment arm
S=body surface
TE=total energy of wave
T=wave period
U_n=normal velocity of water column
U_j=velocity
$\forall$ =volume
X_i =complex amplitude of the excitation force
W= body width
ω=wave frequency
ψ=stream function
Φ=real part of the complex total wave potential
Φ_D= real part of the complex diffraction potential
Φ_I= real part of the complex incident potential
Φ_R= real part of the complex radiation potential
ϕ_D =spatial part of the complex diffraction potential
ϕ_I =spatial part of the complex incident potential
ϕ_R =spatial part of the complex radiation potential
ϕ_j = real part of the complex radiation potential in j^{th} mode
φ_I =real part of the spatial part of the complex incident potential
ξ=complex amplitude of body motion
ζ=normalized frequency

CHAPTER 1. INTRODUCTION

1.1 Interest in Wave Energy

The increase of oil prices in response to the Arab-Israeli war of 1973 initially prompted interest in wave energy. A barrel of oil in mid-1973 cost $2.90, by December of the same year the cost had risen to $11.65 per barrel (Ross, 1995). This excitement in wave energy was further stimulated by Salter's *Nature* article in 1974, introducing Salter's Duck achieving 90% power absorption efficiency (Falnes, 2007). As oil prices declined in the 1980's, so did funding for wave energy.

Increases in population, standard of living, and dependency on technology indicate a future increase in energy demand (Fujita, 2002). This increase in energy coupled with recent concern for climate change and rising oil prices has again generated interest in wave energy. Establishment of projects such as: the European Marine Energy Centre, EquiMar, SuperGen, Wave Hub, and Marine Energy Accelerator indicates a growing support for wave energy research and development in Europe (Drew, 2009).

The United States participation in the development of wave energy conversion (WEC) devices has been low thus far. Between 1979 and 1996, the U.S. Department of Energy (DOE) only contributed about $1.5 million dollars to wave-related activity (Brooke, 2003). However, in 2008 the DOE created two National Marine Energy Centers in partnership with the University of Hawaii, Oregon State University, and the University of Washington (McCormick and Ertekin, 2009). The program aims to research power generation form various forms of ocean energy (McCormick and Ertekin, 2009). Although private companies, such as Ocean Power Technologies Inc. (OPT) and Aqua Energy Group, have been working in the United States on wave energy projects, they have yet to produce any published results.

1.2 Advantages of Wave Energy

Advantages of harnessing wave energy versus other forms of renewable energy are:

- Far propagation
- Seasonal compatibility
- Low atmospheric emissions

1.2.1 Wave Propagation

Waves are able to propagate long distances with little energy loss (Clément, 2002). Swells can have wavelengths of 100 to 500 meters in deep water, and wind waves can have wavelength ranging a few meters to 500m in deep water depending on wind speed (Falnes, 2007).

1.2.2 Seasonal Compatibility

The seasonal variability of wave energy tends to follow the electricity demand in high latitudes, where there is a higher population density (Clément, 2002). The wave power level is highest in the winter when electricity demand increases due to heating and lighting loads (Cruz, 2008).

1.2.3 Low Atmospheric Emissions

It is difficult to fully recognize the environmental impacts of WEC devices due to a lack of ocean testing for substantial lengths of time. However, WEC devices are expected to have few environmental impacts, in particular, low atmospheric emissions (Clément, 2002). WEC devices would produce no atmospheric emissions while generating electricity, however, emissions would occur during installation, maintenance, and decommission (Cruz, 2008). In 1998 Thorpe carried out a lifecycle emissions evaluation of various energy sources, including nearshore WEC devices. The results are presented in Figures 1.1 to 1.3, confirming WEC devices would have relatively low atmospheric emissions.

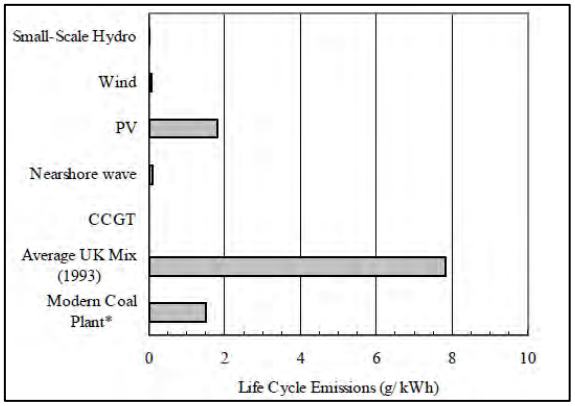

Figure 1. 1 Comparison of Life Cycle Emissions of SO_x (Thorpe, 1999)

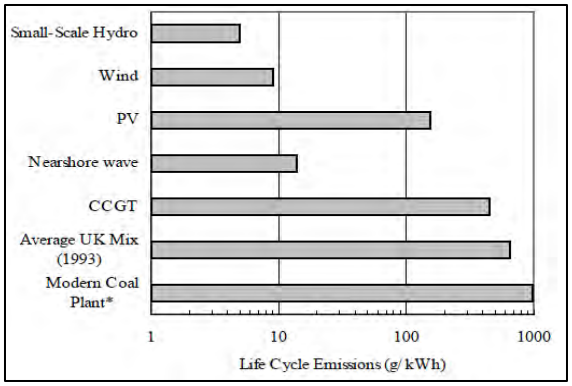

Figure 1.2 Comparison of Life Cycle Emissions of CO_2 (Thorpe, 1999)

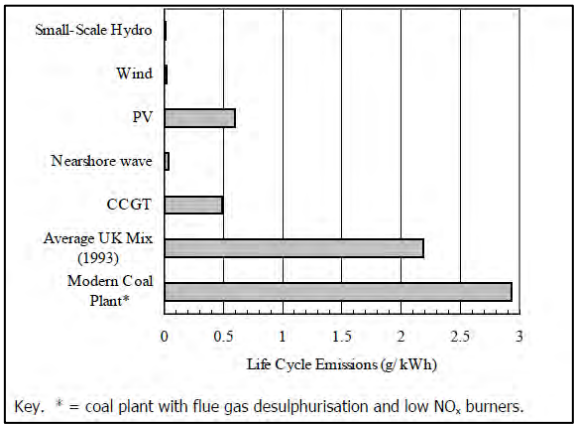

Figure 1.3 Comparison of Life Cycle Emissions of NO_x (Thorpe, 1999)

1.3 Challenges for Wave Energy

Challenges presented with wave energy conversion include:

- Cost
- Durability
- Frequency issues
- Variability

1.3.1 Cost

In 1992 and 1999 Thorpe performed a cost report on wave energy for the UK's Department of Trade and Industry. Thorpe analyzed the cost of electricity generated and the internal rate of return

for various projects. Included in the cost of electricity generation are the capital cost, operation and maintenance (O&M) cost, the annual running cost, and the average annual power output. The capital cost, installation cost, and O&M cost are presented in Figures 1.4 to 1.6. A cost comparison from Thorpe's data is presented in Table 1.1.

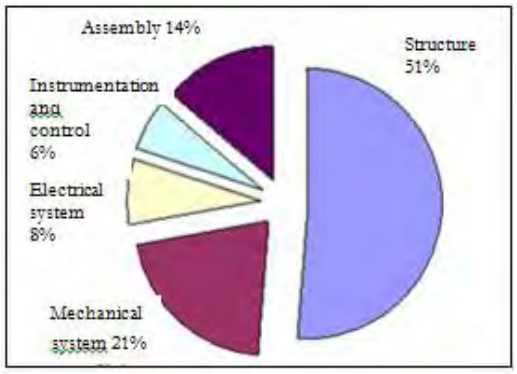

Figure 1. 2 Capital Cost Breakdown/Unit (Thorpe, 1999)

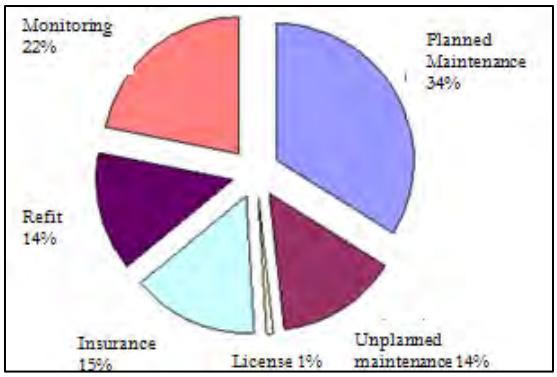

Figure 1. 5 O&M Cost/Unit (Thorpe, 1999)

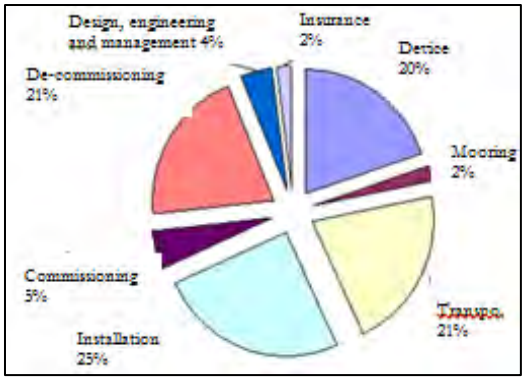

Figure 1.6 Capital Cost for Installation Breakdown/ Unit (Thorpe, 1999)

Table 1.1 Wave Energy Conversion Device Costs (Thorpe, 1999) (Discount rate of 8%)

Device	Capital Cost	O&M Cost	Additional Annual Cost	Average Annual Power Output	Electricity Cost
Limpet	850,000-1,160,000 pounds	23,000 pounds		206 kWh	6.5 pounds/kWh
Osprey	36.8 million pounds	388 thousand pounds	365,000 pounds		5.0 pounds/kWh
Duck (1998)	2.4 billion pounds /334 ducks	74 million pounds/yr.		2 GW/334 ducks	5.3 pounds/kWh
PS Frog	1.1 million	44,000 pounds	21,000 pounds		2.0

	pounds				pounds/kWh
McCabe Wave Pump	1 million pounds/yr.	30,000 pounds	15,000 pounds		5.3 pounds/kWh
IPS Buoy	3.5 million pounds	46,000 pounds	21,000 pounds	7.77 GWh	2.5 pounds/kWh

Bedard and Hagerman (2004) also performed a cost assessment of WEC devices for E2-EPRI in 2004; the results are given in Table 1.2. The Carbon Trust calculated the average cost for wave energy is 25 – 91 US cents/kWh. For comparison, the average cost for wind and solar energy are 4 US cents/kWh and 19 US cents/kWh, respectively (Callaway, 2007). Improvements in structural costs, capture efficiency, turbine efficiency, and plant cost have the most potential for cost reduction (Thorpe, 1999).

Table 1.2 Device Cost (Bedard and Hagerman, 2004)

Device	Cost (2004 US dollar)	Included in Cost
AquaBuoy	$3 million	Structure, Mooring, Installation, Cable,
Energetch	$2.5-3 million/device	Structure
Seadog	$3 million/system	Structure, Installation
Ocean Power	$2-3 million/device	Structure
Orecon	$3 million/device	Structure, Installation, Cable
Teamwork	$4-6 million/device	Structure
Wave Dragon	$10-12 million/device	Structure

External costs associated with WEC devices may include: visual impacts, higher noise levels, impacts on biotic system, and marine pollution (Cruz, 2008). Airborne noise may potentially be reduced using acoustic muffling techniques, and may be masked by the noise of waves and the wind (Brooke, 2003). However, underwater noise is able to propagate far and may potentially impact marine mammal communication; this needs to be further studied (Cruz, 2008). With respect to impacts on biotic system, WEC devices may affect the turbidity, sediment deposition, and population of benthic flora and fauna (Cruz, 2008). Marine

pollution would occur from hydraulic oil spills; fail-safe systems and the use of biodegradable oils would reduce this threat (Brooke, 2003).

1.3.2 Durability

Structural challenges include: extreme wave conditions, corrosion, and leakage. Extreme wave conditions may cause stroke overextension or slamming (Backer, 2009). Stroke overextension refers to exceeding the natural motion of the body. Slamming occurs when the body re-enters the water after losing contact with the surface, causing fatigue (Backer, 2009). These extreme loads can be difficult to predict, and may be up to 100 times the mean load (Clément, 2002). Corrosion also causes fatigue, although ceramic coating offers some solution to the problem (Drew, 2009). For example, in 2003 the Nissum Bredning had to be brought back to shore due to a rusty screw, which could have been prevented had stainless steel been used (Callaway, 2007). Leakage of pumps or hydraulic fluids may also cause concern; in 2007 the Aqua Buoy sank due to a pump failure (Callaway, 2007).

1.3.3 Frequency Issues

The frequency of waves are challenging for multiple reasons: a lack of compatibility with electric generators, a lack of compatibility with bodies, and a narrow bandwidth (Falcão, 2010). Generators typically require frequencies 500 times greater than the frequency provided by waves (Clément, 2002). For a single body impinged on by a harmonic wave, resonance between the body and wave is optimal. However, unless the body is large (lengths greater than 10m) or supplementary weight is added, wave frequencies are typically too low to resonate with the body (Falcão, 2010). For small bodies, the resonance bandwidth is

narrow creating a limited number of optimal conditions. Phase control methods, such as latching, may be used to mediate these problems.

1.3.4 Variability

The wave power is variable on multiple time scales: wave to wave, hour to hour, month to month, etc. (Falcão, 2010). However, power supply needs to be smooth and constant, thus, requiring a storage device or an array of bodies (Drew, 2009). The average power level may also be overestimated with seasonal variability and extreme conditions making it difficult to design for a particular wave climate. Wave direction is also variable, thus the WEC devices either need to align in a position to most often capture the wave's power or need to be symmetrical (Drew, 2009).

1.4 Potential Location for Wave Energy

Drew (2009) considers locations with average power levels of 30 – 70kW/m suitable for wave energy harvesting; typically these occur at latitudes of 40° – 60° seen in Figure 1.7. Suitable locations include Western Europe, the Pacific Northwest of America, South America, South Africa, and Australia with a higher resource in the southern hemisphere (Cruz, 2008). Tropical waters typically rate poorly with average power levels of 15 – 20kW/m. Factors to consider in conjunction with wave power levels are population density and seasonal variation. Although the southern hemisphere has the best wave resources, there is a higher energy demand in the northern hemisphere.

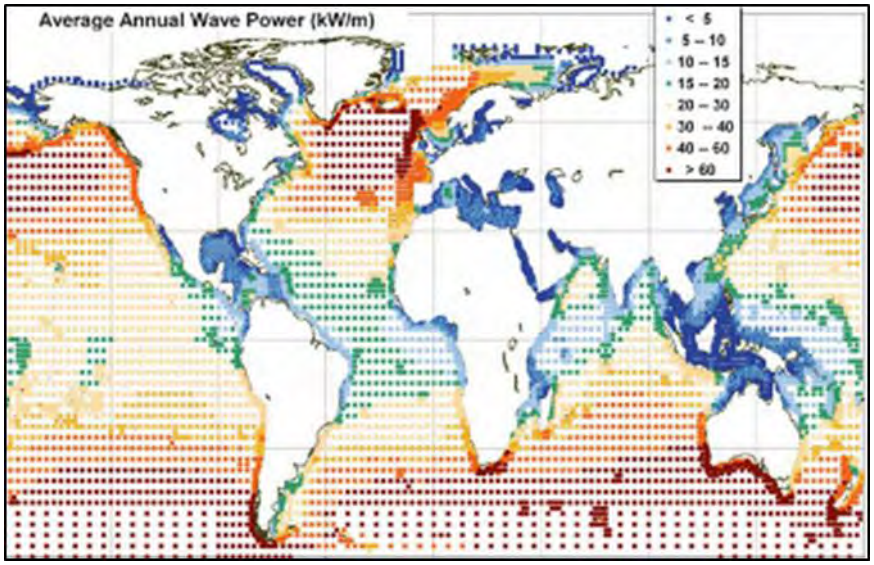

Figure 1. 7 Average Annual Wave Power (kW/m) (Cruz, 2008)

High seasonal variation creates design and reliability issues. According to Falnes (2007) winter waves can contain up to 5 – 10 times the average energy of summer waves. The seasonal variation can be seen in Figures 1.8 and 1.9. The southern hemisphere also has a smaller seasonal variation, making locations such as South America, Africa, and Australia more desirable for wave energy extraction.

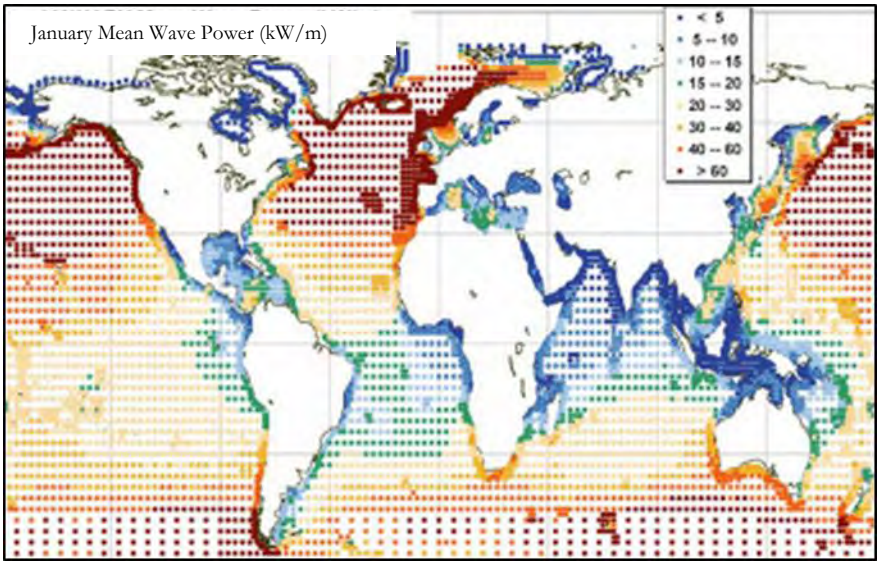

Figure 1. 8 January Mean Wave Power (kW/m) (Cruz, 2008)

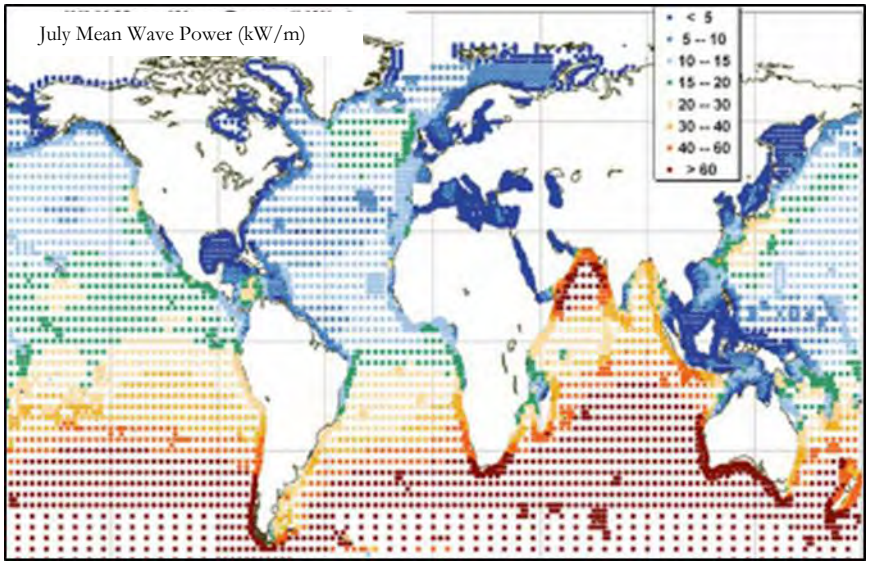

Figure 1.9 July Mean Wave Power (kW/m) (Cruz, 2008)

1.5 Literature Review

The beginning pioneers of wave energy include Masuda, Salter, Budal, Mei, Newman, Falnes, and Evans (Falcão, 2010). Beginning in the 1970's theoretical work was studied for single, point absorbers with one degree of freedom in regular, linear waves with a linear generator. The theory is similar to that of ship hydrodynamics, which had been well established. Eventually, theoretical work was done with regards to oscillating water columns, point absorbers with multiple degrees of freedom, and arrays of buoys. Jefferys later addressed the issue of nonlinear power take-off systems (Falcão, 2010).

Experimental work was pioneered by Masuda in the 1940's, and Salter's Wave Power Group in the 1970's at the University of Edinburgh. In the 1980's Budal and Falnes also began experimental work on control mechanisms for point absorbers in irregular waves, so as to operate in the most efficient frequency. Areas in need of further research include: phase control, environmental impacts, maintenance, and power take-off systems (Falcão, 2010).

Backer (2009) numerically and experimentally studied the damping force, tuning force, excitation force, and absorbed power for heaving point absorbers under regular and irregular wave conditions. A cone-cylinder and hemisphere-cylinder were studied with varying drafts and waterline cross-sectional area. Additionally, Backer (2009) studied the effects of slamming, stroke, and force restrictions on power absorption efficiency, excitation forces, damping forces, and tuning forces.

1.6 Objective of the Present Study

This project is inspired by Salter's 1974 paper and Backer's 2009 Ph.D. thesis. The purpose of this thesis is to study the effects of geometry on maximum power absorption efficiency for a single, two-dimensional, surface-piercing, heaving body impinged by a linear, regular, harmonic wave. In particular, the geometry of asymmetric bodies is explored. The goal is to study the effects of a body's geometry on maximum power absorption efficiency for a sample group. The uniqueness of this work is the method used to calculate the maximum power absorption efficiency by calculating the radiated wave amplitude at positive and negative infinity.

The diffraction problem for various two-dimensional bodies is studied numerically. An experiment to study the diffraction problem is also proposed. AQWA version 14.0 is the software used to evaluate a wider range of bodies. The numerical model has been verified by comparing results with the experimental results of Nojiri and Muryama (1975) and the numerical results of Koo and Kim (2005) for a fixed barge model. The excitation force is found numerically, which is used to calculate the radiated wave amplitudes at positive and

negative infinity. Thus, the maximum power absorption efficiency is calculated, and the various bodies may be compared in terms of efficiency. This work will hopefully have implications for wavemakers, wave energy conversion devices, and breakwater systems. With respect to WEC devices, this work mostly closely relates to terminators, which will be defined in Chapter 2.3.

CHAPTER 2. WAVE ENERGY CONVERSION DEVICE CLASSIFICATION

Current devices are listed and classified in Table 2.1. The classification systems are further defined below, this is by no means an exhausted list of all classification systems. The information in this chapter is a collection of the work done by Price (2009) and Carter (2005).

2.1 Location

Locations to place WEC devices are:

- Shoreline
- Nearshore
- Offshore

2.1.1 Shoreline

Shoreline devices are embedded into the coast, such as the Limpet, an OWC device in the U.K. (http://www.wavegen.co.uk/contact.htm). They are relatively cheap to maintain and install. It is also less expensive to transmit energy due to the relative proximity to the utility network (Drew, 2009). Shoreline devices are subject to a less powerful wave regime due to shoaling, friction, wave breaking, reflection, etc. This reduces the likelihood of the devices damaged by extreme wave conditions. However, there is less energy that could potentially be harvested. They are also site-specific, and thus cannot be mass produced. Additionally there are aesthetic and noise impacts on nearby communities with shoreline devices (Drew, 2009).

2.1.2 Nearshore

Nearshore devices are typically in relatively shallow water, approximately 20 meters deep. Again the devices are relatively easy to maintain and install compared to offshore devices.

These too are subjected to a less powerful wave regime (Drew, 2009). An example of a nearshore device is the OSPREY (Clément, 2002).

2.1.3 Offshore

Offshore devices are installed in deep water, approximately 40 meters or deeper. The higher energy waves are offshore, however, these devices are more expensive to deploy and maintain (Falcão, 2010). Since these devices also experience the higher energy waves, they also are most subjected to destructive conditions (Drew, 2009). Examples of offshore devices include the Archimedes Wave Swing and Pelamis (Clément, 2002).

2.2 Mode of Motion

Mode of motion describes which and how many degrees of freedom the device has. There are six potential degrees of freedom; the first three listed are translational and the latter three are rotational, as seen in Figure 2.1:

- Surge
- Sway
- Heave
- Roll
- Pitch
- Yaw

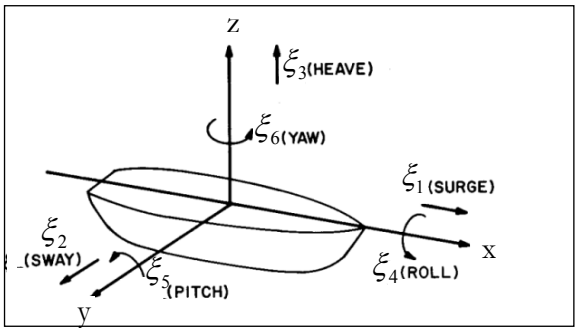

Figure 2.1 Modes of Motion (Newman, 1977)

2.3 Orientation

Orientation is defined as the direction of the device with respect to the incoming wave. Orientation can be further categorized as:

- Point Absorbers
- Attenuators
- Terminators

2.3.1 Point Absorbers

Point absorbers are devices with dimensions much shorter than the wavelength, and are thus non-directional (Newman, 1977). Point absorbers can further be classified as floating, heaving devices or submerged, pressure differential devices. Floating, heaving devices can also be either partially or fully submerged. An example of a point absorber is the Powerbuoy (Drew, 2009).

2.3.2 Attenuators

Attenuators are parallel to the wave propagating direction. Their lengths are typically comparable or longer than the wavelengths. Attenuators typically move via the motion of the wave. The most notable is Pelamis depicted in Figure 2.2 (Drew, 2009).

Figure 2.2 Pelamis (ecogeek.com)

2.3.3 Terminators

Terminators are perpendicular to the wave propagating direction. Their lengths are also comparable or longer than the wavelengths. Salter's Duck depicted in Figure 2.3 is an example of a terminator (Drew, 2009).

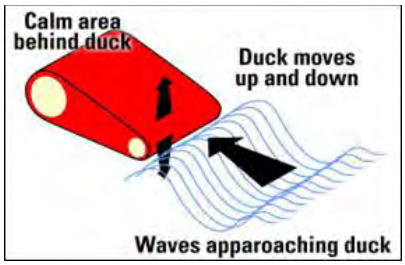

Figure 2.3 Salter's Duck (http://www.jeron.je/anglia/learn/sec/science/sn005/page02.htm)

2.4 Operating Principles

Operating principles include (Drew, 2009):

- Oscillating Water Columns
- Oscillating Bodies
- Overtopping Devices

2.4.1 Oscillating Water Column

An oscillating water column (OWC) has two main components a partially submerged capture chamber and a bidirectional turbine. The rise and fall of the water level increases and decreases the air pressure. The change in air pressure rotates a turbine sitting above the capture chamber. A typical shore-based OWC device is presented in Figure 2.4. The Limpet is an example of an OWC device.

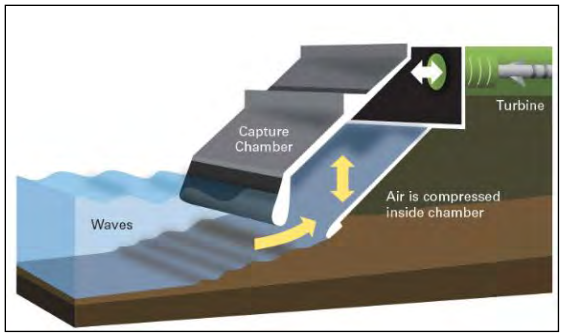

Figure 2.4 Oscillating Water Column (http://www.esru.strath.ac.uk)

2.4.2 Oscillating Bodies

Oscillating bodies can further be categorized as floating, oscillating devices; oscillating wave surge converters; or submerged pressure differential devices. Floating, oscillating devices can either be fully or partially submerged. The kinetic energy of the waves moves the device. Multiple power take-off systems can be used for these devices. Examples of floating, oscillating devices include: Pelamis, PowerBuoy, and Searev (Falcão, 2010).

An oscillating wave surge convertor also moves due to the kinetic energy of the wave. The oscillating wave surge convertor is hinged to the sea bed, and is also a terminator since it is positioned perpendicular to the incoming waves depicted in Figure 2.5. As the device oscillates it drives two hydraulic pistons, which are coupled with a hydraulic turbine. An example is the Aquamarine Power Oyster (Drew, 2009).

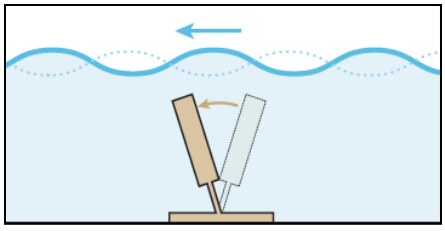

Figure 2.5 Oscillating Wave Surge Converter (Callaway, 2007)

A submerged pressure differential device is composed of a chamber fixed to the seabed and a cylinder which heaves presented in Figure 2.6. The cylinder heaves due to the change in water pressure between wave crests and troughs (Drew, 2009). Either a hydraulic system or a linear generator is used as a power take-off system. Maintenance is difficult since these devices are fixed to the seabed, but are less exposed to damaging conditions (Drew, 2009). An example is the Archimedes Wave Swing.

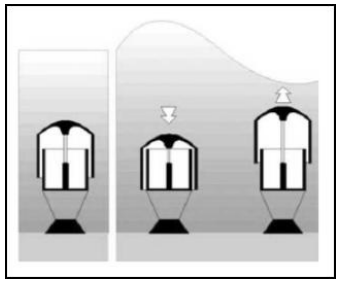

Figure 2.6 Submerged Point Absorber
(http://ikionrenewableenergy.wordpress.com/category/uncategorized/)

2.4.3 Overtopping Devices

Overtopping devices capture incoming waves, and allow the elevated water to exit back into the ocean via a funnel (Drew, 2009). As the water exits the device, it drives a turbine. The turbine then acts on a generator similar to a hydroelectric dam. Figure 2.7 illustrates a typical overtopping device. Examples include the Wave Dragon and the Sea Slot Cone (Drew, 2009).

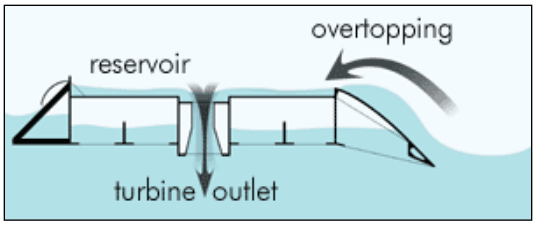

Figure 2.7 Overtopping Device (http://science.howstuffworks.com)

2.5 Reference Point

Means of reaction refers to the relative motion between the primary interface and the power take-off system (Price, 2009). Means of Reaction can be further categorized as:

- Fixed
- Referenced
- Inertial

2.5.1 Fixed

A fixed reference point from the WEC device is typically the seabed or shoreline. For static coupling this requires a rigid mooring system, and for a dynamic coupling it requires a taut system.

2.5.2 Referenced

A referenced point refers to a neighboring body that also experiences an excitation force. A taut or slacked mooring system is used for a referenced point. Pelamis uses such a reference point. Each cylinder experiences a different force, thus driving the hydraulic fluid.

2.5.3 Inertial

An inertial reference point refers to a primary interface that does not experience an excitation force. For example a water column would be an inertial reference point.

2.6 Mooring Systems

Mooring systems used include (Price, 2009):

- Rigid

- Taut
- Slack

2.6.1 Rigid

A rigid mooring system is embedded into the ground or shoreline. A rigid mooring system is required when the motion of the WEC device is statically coupled to the seabed (Price, 2009). Examples include the Limpet, Archimedes Wave Swing, and the Aquamine Power Oyster.

2.6.2 Taut

A taut mooring system uses an elastic but tightly stretched connection. It is used when the device does not need to move, but cannot be fixed to the bottom of the sea. A taut mooring system is required when the WEC device is dynamically coupled to the seabed (Price, 2009). The Wave Dragon is an example of a tautly moored device.

2.6.3 Slack

A slack-mooring system maintains the device's station, but allows for the device to move. A slack-mooring system is required when the means of reaction is either referenced or inertial (Price, 2009). Often these mooring systems are associated with offshore devices (Price, 2009). An example of a slack-mooring system is Pelamis.

2.7 Power Take-Off System (P.T.O.)

Power take-off systems transfer the wave's mechanical energy to electrical energy. Power take-off system classifications include (Drew, 2009):

- Hydraulic System

- Linear Generator
- Turbine
- Rotary Generator

2.7.1 Hydraulic System

Hydraulic systems are used for large forces at slow speeds, such as those experienced in deep water (Drew, 2009). Hydraulic systems are well suited to incorporate a variety of methods to smooth the power levels, such as storage and latching (Drew, 2009). The waves move hydraulic cylinders, which pump hydraulic fluid to a hydraulic motor. The hydraulic motor then drives a rotary generator. One particular concern with hydraulic systems is the leakage of hydraulic fluid. Pelamis uses a hydraulic system.

2.7.2 Linear Generator

Linear generators are now being considered due to breakthroughs in magnetic material and frequency converting electronics (Drew, 2009). A linear generator induces a current by moving a magnet through a solenoid, as seen in Figure 2.8. It is more simplistic compared to a turbine or hydraulic system, and thus requires less maintenance work. Linear generators would be applicable to offshore devices where maintenance work is more difficult. The Archimedes Wave Swing uses a linear generator.

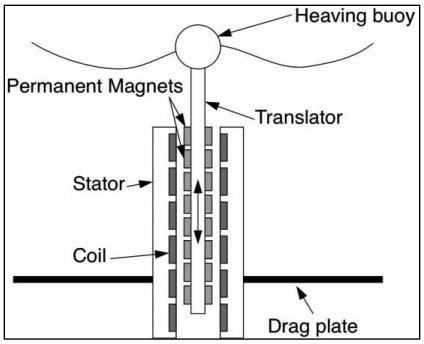

Figure 2.8 Linear Generator (Drew)

2.7.3 Turbine

Turbines are driven by either water or air, and are coupled to a generator (Drew, 2009). An advantage of turbines is they can offer regulation over wave power variation by controlling the volume of the fluid (Brooke, 2003). WEC devices require special bidirectional turbines, such as the Wells Turbine. Oscillating water columns and overtopping wave devices use bidirectional turbine systems.

2.7.4 Rotary Generator

Rotary generators have potential use when coupled with turbines. These types of devices are popular with wind energy, and have thus been extensively studied for renewable energy sources (Drew, 2009).

Table 2. 1 WEC Classifications

Device	Anaconda	AquaBuoy	Archimedes Wave Swing	Backward Bent Duct Buoy
Company	Checkmate Seaenergy UK Ltd.	Finavera	AWS Ocean Energy	National Institute of Ocean Technology
Submerged /Partially Submerged	Submerged	Partially	Submerged	Partially
Location	Offshore	Offshore	Offshore	Offshore
Mode of Motion	Heave	Heave	Heave	Pitch/ Heave
Orientation	Attenuator	Point Absorber	Point Absorber	Terminator
Operating Principle	Oscillating Body	Oscillating Body	Oscillating Body	OWC
Reference Point	Referenced	Referenced	Inertial	Inertial
Mooring	Slack	Rigid	Rigid	Slack
P.T.O.	Hydraulic System	Hydraulic System + Piston	Linear Generator	Turbine + Generator

Device	Energetech OWC	FO3	IPS Buoy	Limpet	Manchester Bobber	McCabe Wave Pump	Mighty Whale	Mutriku
Company	Energetech Australia Pty. Ltd.	Fobox AS	Interproject Service (IPS) AB	Voith Hydro Wavegen	Manchester Bobber	Hydam Technology	JAMSTEC	Ente Vasco de la Energía
Submerged /Partially Submerged	Partially	Partially	Submerged	Partially	Partially	Partially	Partially	Partially
Location	Shoreline	Nearshore	Offshore	Shoreline	Offshore	Offshore	Offshore	Nearshore
Mode of Motion	Heave	Heave	Heave	Heave	Heave	Pitch	Heave	Heave
Orientation	Terminator	Point Absorber	Point Absorber	Terminator	Point Absorber	Attenuator	Terminator	Terminator
Operating Principle	OWC	Oscillating Body	Oscillating Body	OWC	Oscillating Body	Oscillating Body	OWC	OWC
Reference Point	Inertial	Referenced	Inertial	Inertial	Inertial	Inertial	Inertial	Inertial
Mooring	Rigid	Slack	Rigid	Rigid	Rigid	Slack	Taught	Rigid
P.T.O.	Turbine + Generator	Hydraulic System	Piston	Turbine + Generator	Linear Generator	Hydraulic System	Turbine + Generator	Turbine + Generator

Device	Oceanlinx	Osprey	Oyster	Pelamis	Pico	PowerBuoy	PS Frog	Salter's Duck	Sakata	SEADOG	SEARVEV	Sper Buoy
Company	Oceanlinx	Wavegen of Inverness	Aquamarine Power	Pelamis Wave Power	Instituto Superior Tecnico	Ocean Power Technologies	Lancaster University	University of Edinburgh	Japanese Ministry of Transport	Independent Natural Resources	Ecole Centrale de Nantes	Embley Energy
Submerged /Partially Submerged	Partially	Partially	Partially	Partially	Partially	Submerged	Partially	Partially	Partially	Partially	Partially	Partially
Location	Offshore	Nearshore	Nearshore	Offshore	Shoreline	Offshore	Offshore	Offshore	Nearshore	Nearshore	Offshore	Offshore
Mode of Motion	Heave	Pitch Heave	Pitch	Pitch Heave	Heave	Heave	Pitch/Surge	Pitch	Heave	Heaving	Pitching	Heaving
Orientation	Terminator	Terminator	Terminator	Attenuator	Terminator	Point Absorber	Point Absorber	Terminator	Terminator	Point Absorber	Point Absorber	Terminator
Operating Principle	OWC	OWC	Oscillating Body	Oscillating Body	OWC	Oscillating Body	Oscillating Body	Oscillating Body	OWC	Oscillating Body	Oscillating Body	OWC
Reference Point	Inertial	Inertial	Fixed	Referenced	Inertial	Inertial	Referenced	Referenced	Inertial	Inertial	Referenced	Inertial
Mooring	Taught	Rigid	Rigid	Slack	Rigid	Rigid	Slack	Slack	Rigid	Rigid	Slack	Taught
P.T.O.	Turbine + Generator	Turbine + Generator	Hydraulic System	Hydraulic	Turbine + Generator	Linear Generator	Hydraulic System	Hydraulic System	Turbine + Generator	Piston	Hydraulic System	Turbine + Generator

Device	SSG	TAPCHAN	WaveBob	Wave Dragon	Wave Plane	Wave Rider	Wave Roller	Wave Rotor	WaveStar
Company	Wave Energy AS	Norwave	WaveBob Limited	Wave Dragon	WavePlane Production	SeaVolt Technologies	AW Energy	Ecofys	Wave Star Energy ApS
Submerged /Partially Submerged	Partially	Partially	Partially	Partially	Partially	Partially	Submerged	Partially	Partially
Location	Shoreline	Shoreline	Offshore	Offshore	Nearshore	Nearshore	Nearshore	Offshore	Nearshore
Mode of Motion	-	-	Heave	Heave/ Surge	-	-	Pitch	Roll	Heave
Orientation	Terminator	Terminator	Point Absorber	Terminator	Terminator	Point Absorber	Terminator	Point Absorber	Point Absorber
Operating Principle	Overtopping Device	Overtopping Device	Oscillating Body	Overtopping Device	Overtopping Device	Oscillating Body	Oscillating Body	Oscillating Body	Oscillating Body
Reference Point	Inertial	Inertial	Referenced	Inertial	Inertial	Fixed	Fixed	Inertial	Inertial
Mooring	Rigid	Rigid	Slack	Slack	Taught	Taught	Rigid	Rigid	Fixed
P.T.O.	Turbine	Turbine + Generator	Hydraulic System	Turbine	Turbine	Hydraulic System	Hydraulic System	Turbine	Hydraulic System

CHAPTER 3. THEORY AND GOVERNING EQUATIONS

3.1 Governing Equation and Boundary Conditions

Linear potential theory is applied in this study. The following derivation of the incident wave potential assumes a two-dimensional Cartesian coordinate system (x, z) with a vertical z-axis positive in the upward direction. The unit normal vector, $\vec{n}$, is positive leaving the fluid. The still water level is set at z=0. Figure 3.1 depicts the problem. Assumptions made with linear potential theory as used here are as follows:

1. H/d << 1
2. H/L << 1
3. Constant atmospheric pressure at free-surface
4. Impervious seabed and body
5. Irrotational flow ($\nabla \times \vec{U} = 0$)
6. Inviscid fluid
7. Incompressible fluid ($\nabla \cdot \vec{U} = 0$)
8. Constant water depth
9. Waves are periodic in time and along the x-axis
10. Surface elevation, $\vec{\eta}$, travels solely along the x-axis
11. No overtopping of waves
12. Boundary conditions are linearized, and are satisfied on z=0 rather than z=η
13. The body is rigid and is subject to small motions along the free-surface

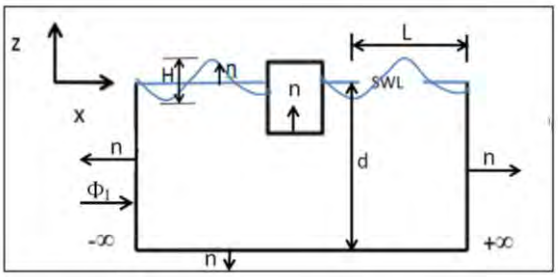

Figure 3. 1 Two Dimensional Single, Heaving Body

By assuming the flow is irrotational, the fluid velocity may be described by the velocity potential:

$$\vec{U} = \nabla\Phi \quad (1)$$

where Φ denotes the real part of the complex velocity potential, ϕ denotes the spatial part of the complex potential, and φ denotes the spatial part of the real part of the complex potential[1].

$$\Phi = \left(\varphi e^{-i\omega t}\right)$$

$$\Phi = \Re\left(\phi e^{-i\omega t}\right)$$

The total potential per unit wave amplitude is:

$$\Phi_T = \Re\left\{\left(\left(\phi_D + \phi_I\right) + \sum_j \xi_j \phi_j\right) e^{-i\omega t}\right\} \quad (2) \qquad \text{for j=1,3,5}$$

where ϕ_D denotes the diffraction potential, ϕ_I denotes the incident potential, and ϕ_j denotes the radiation potential in the j^{th} direction. These will be further defined in sections 3.3.2 and 3.3.3.

Combining the continuity equation and Eq. (1) results in the governing equation, namely Laplace's equation:

$$\nabla^2\Phi = \frac{\partial^2\Phi}{\partial x^2} + \frac{\partial^2\Phi}{\partial z^2} = 0 \quad (3) \qquad \text{in the fluid domain}$$

Laplace's equation must be satisfied by all potentials listed in Eq. (2).

Kinematic Free-Surface Boundary Condition (k.f.s.b.c.)

The k.f.s.b.c. states that the normal velocities of the fluid particles and the boundary surface are equal at the free-surface. The k.f.s.b.c. is derived from the material derivative:

Let

[1] $\Re$ denotes the real part of the equation

$$F(x,z,t) = z - \eta = 0$$

$$\frac{DF}{Dt} = \frac{\partial F}{\partial t} + \vec{u} \cdot \nabla F = 0$$

$$-\frac{\partial \eta}{\partial t} + \frac{\partial \Phi}{\partial z} - \frac{\partial \eta}{\partial x}\frac{\partial \Phi}{\partial x} = 0 \qquad (4) \qquad \text{on } z=\eta$$

The third term in Eq. (4) is a higher-order term, and is neglected to linearize the boundary condition. Therefore, Eq. (4) is approximated as:

$$\frac{\partial \Phi}{\partial z} = \frac{\partial \eta}{\partial t} \qquad (5) \qquad \text{on } z=0$$

Dynamic Free-Surface Boundary Condition (d.f.s.b.c.)

The d.f.s.b.c. states that the pressure on the free-surface must be atmospheric, and is derived from Euler's integral:

$$-\frac{1}{\rho}(p - p_a) = gz + \frac{\partial \Phi}{\partial t} + \frac{1}{2}\nabla\Phi \cdot \nabla\Phi \qquad (6)$$

The surface tension is insignificant, and thus the pressure immediately below the free-surface is equal to the atmospheric pressure, reducing Eq. (6) to:

$$\frac{\partial \Phi}{\partial t} + \frac{1}{2}\nabla\Phi \cdot \nabla\Phi + g\eta = 0 \qquad (7) \qquad \text{on } z=\eta$$

The velocity term is neglected because it is a higher-order term, resulting in:

$$\eta = \frac{-1}{g}\frac{\partial \Phi}{\partial t} \qquad (8) \qquad \text{on } z=0$$

Although the nonlinear free-surface boundary conditions are imposed on the free-surface, they are evaluated on z=0 by noting that the unknown surface elevation differs from the still water level at a higher-order (Mei, 1989). Laplace's equation is thus also evaluated at -d<z<0.

Combining Eq. (5) and Eq. (8) results in the following combined linearized free-surface boundary condition:

$$g\frac{\partial \Phi}{\partial z}+\frac{\partial^2 \Phi}{\partial t^2}=0 \qquad (9) \qquad \text{on } z=0$$

The combined free-surface boundary condition must be satisfied by all potentials listed in Eq. (2).

Seabed Boundary Condition (s.b.b.c)

The s.b.b.c. states that there is no normal flow through the seabed:

$$\frac{\partial \Phi}{\partial z}=0 \qquad (10) \qquad \text{on } z=-d$$

The s.b.b.c. must be satisfied by all potentials listed in Eq. (2).

Body Boundary Condition (b.b.c)

The b.b.c. similarly states that fluid cannot pass through an impervious body. Below S denotes the control surface of the body. For a fixed body the total potential must satisfy:

$$\frac{-\partial \Phi_I}{\partial n}=\frac{\partial \Phi_D}{\partial n} \qquad (11) \qquad \text{on S}$$

For a body with a velocity, U_i, the radiation potential must satisfy:

$$\frac{\partial \varphi_i(x,z,t)}{\partial x_i}=U_i n_i \quad (12) \qquad \text{on S} \qquad \text{for i=1, 3,5}$$

where, φ_i denotes the radiation potential per unit wave amplitude in the surge, heave, and pitch directions, which are denoted by i=1, 3, and 5, respectively. Applying Kirchhoff decomposition Eq. (12) may be written as:

$$\frac{\partial \varphi_i}{\partial n} = n_i \qquad (13) \qquad \text{on S} \qquad \text{for i=1, 3}$$

$$\frac{\partial \varphi_i}{\partial n} = (r \times n)_{i-3} \qquad (14) \qquad \text{on S} \qquad \text{for i=5}$$

where, $\vec{r}$ denotes the moment arm.

Radiation Condition

Finally, the radiation condition must be satisfied by the diffraction and radiation potentials. The radiation condition for the two-dimensional case is:

$$\frac{\partial \varphi(x,z)}{\partial x} \mp ik\varphi(x,z) \to 0 \qquad (15) \qquad \text{as } x \to \pm\infty$$

3.2 Solving for the Incident Wave Potential

Separation of variables is used to solve for the incident potential:

$$\Phi = f(x,z,t) \to \Phi = \Re\{X(x)T(t)Z(z)\} \qquad (16)$$

Substituting Eq. (16) into Eq. (3) results in two ordinary differential equations:

$$\frac{d^2Z}{dz^2} - K^2 Z(z) = 0 \qquad (17)$$

$$\frac{d^2X}{dx^2} + K^2 X(x) = 0 \qquad (18)$$

where, K is a separation constant. The solutions to the ordinary differential equations are:

$$X(x) = B \cdot \cos(kx) + C \cdot \sin(kx) \qquad (19)$$

$$Z(z) = De^{kz} + Ee^{-kz} \qquad (20)$$

where, B, C, D, and E are constants to be determined. The velocity potential for a regular, progressive wave assumes the form:

$$\Phi(x,z,t) = \Re\left\{Z(z)e^{i(kx-\omega t)}\right\} \quad (21)$$

Substituting Eq. (20) into Eq. (21) results in:

$$\Phi = \Re\left\{\left(De^{kz} + Ee^{-kz}\right)e^{i(kx-\omega t)}\right\} \quad (22)$$

In order to avoid an unbounded motion in the case that $d \to \infty$, E goes to 0:

$$\Phi = \Re\left\{De^{kz}e^{ikx-i\omega t}\right\} \quad (23)$$

The surface elevation for a two-dimensional, periodic, progressive wave is:

$$\eta(x,t) = A\cos(kx - \omega t) = \Re\left\{Ae^{i(kx-\omega t)}\right\} \quad (24)$$

Note this thesis assumes a right-running incident wave. The parameter A is the amplitude of the wave, i.e., half the wave height, H. The parameter k denotes the wave number, or number of waves per unit wavelength, L:

$$k = \frac{2\pi}{L} \quad (25)$$

The parameter ω denotes the angular frequency, or the number of waves per unit period, T:

$$\omega = \frac{2\pi}{T} \quad (26)$$

Combining Eq. (8) and Eq. (24) at z=0, x = 0, and t=0; results in:

$$A = \frac{-1}{g}\frac{\partial \Phi}{\partial t} \quad (27)$$

Taking the time derivative of Eq. (23) at z=0, x=0, and t=0 results in:

$$\frac{\partial \Phi}{\partial t} = -Di\omega \quad (28)$$

Combining Eq. (27) and Eq. (28) results in:

$$D = \frac{-Agi}{\omega} \quad (29)$$

The two-dimensional real part of the complex incident wave potential, Φ_I, is:

$$\Phi_I = \Re\left\{ \frac{-iAg}{\omega} e^{kz} e^{i(kx-\omega t)} \right\} \qquad (30)$$

If the water depth, d, is finite, then the depth parameter, e^{kz}, is rewritten as $\frac{\cosh(k(z+d))}{\cosh(kd)}$, satisfying the seabed boundary condition:

$$\Phi_I = \frac{Ag}{\omega} \frac{\cosh(k(z+d))}{\cosh(kd)} \sin(kx-\omega t)$$

To satisfy the free-surface boundary condition, the phase velocity is described by the dispersion relation:

$$C = \frac{\omega}{k} = \left(\frac{g}{k} \tanh(kd) \right)^{1/2} \qquad (31)$$

Energy, however, does not travel at the phase velocity. Rather, energy travels at the group velocity, which is seen in a kinematic or dynamic view. The kinematic view is presented below. A band of waves with similar lengths and traveling in a similar direction at a group velocity, C_g, comprise a wave envelope:

$$C_g = \frac{\partial \omega}{\partial k} \qquad (32)$$

Then Eq. (32) converges to:

$$C_g = \frac{d\omega}{dk} = \frac{C}{2}\left(1 + \frac{2kd}{\sinh(2kd)} \right) \qquad (33)$$

Figure 3.2 depicts the individual waves moving with a phase velocity traveling in a band with a group velocity.

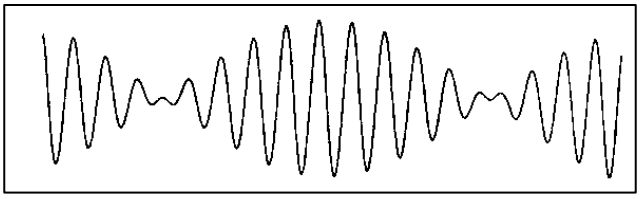

Figure 3. 2 Individual waves travel at a phase velocity, as wave groups travel at group velocity (Newman, 1977)

The wave slope and wave dispersion dictate the applicability of linear wave theory. The wave slope is the wave height to wavelength ratio; it is assumed to be extremely small in linear wave theory. Linear wave theory is typically only applicable in deep and intermediate water depths, where deep water is defined as $\frac{depth}{wavelength} > 0.5$, and intermediate water by $0.05 < \frac{depth}{wavelength} < 0.5$. The limitation of linear wave theory with respect to the wave slope and wave dispersion is presented in Figure 3.3.

This thesis terms the ratio of the characteristic body length to the wavelength as the diffraction parameter. Diffraction theory is applicable when the structure length spans a significant portion of the wavelength, and thus incoming waves undergo scattering. The goal of this study is to detect geometric effect on wave power absorption, and thus diffraction theory is applied.

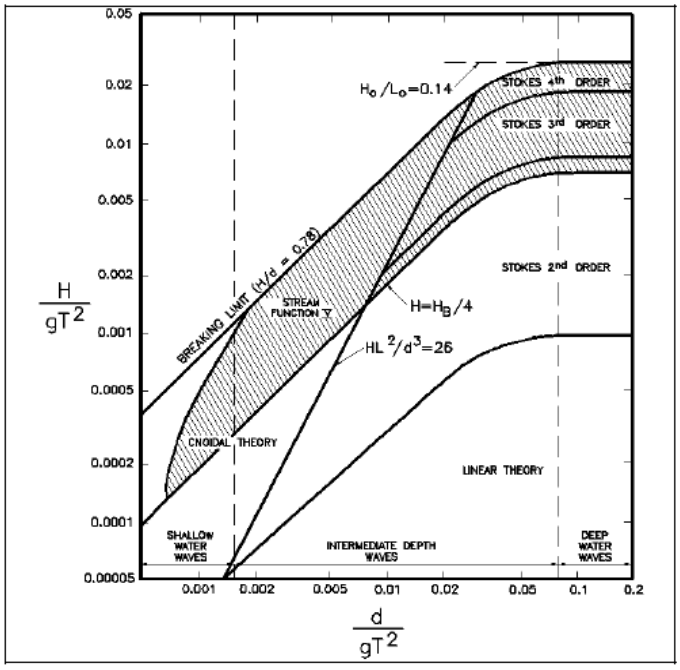

Figure 3. 3 Range of Suitability for Various Wave Theories (Le Méhauté, 1979)

3.3 Force on Bodies

This section presents general hydrodynamic concepts for a two-dimensional, floating body. The governing equation is linear, and by assuming the waves are small the boundary conditions are linearized. Thus, allowing various properties of wave-body interaction to be superposed. Therefore, the total force on a body can be decoupled into hydrostatic and hydrodynamic forces. The total force per unit wave amplitude is:

$$F_{T_i} = -\rho g \int_S z n_i dS - \rho \Re\left\{-i\omega e^{-i\omega t}\int_S (\phi_D + \phi_I) n_i dS\right\} - \rho \Re\left\{\sum_j -i\omega \xi_j e^{-i\omega t}\int_S \phi_j n_i dS\right\} \quad (34)$$

for j=1, 3, 5
i=1, 3

where, ξ_i denotes the complex amplitude of the body in the j[th] direction. The total moment per unit wave amplitude with a moment arm, $\vec{r}$, is:

$$M_{T_k} = -\rho g \int_S z \varepsilon_{ijk} r_i n_j dS - \rho \Re\left\{-i\omega e^{-i\omega t}\int_S (\phi_I + \phi_D) \varepsilon_{ijk} r_i n_j dS\right\} - \rho \Re\left\{\sum_j -i\omega \xi_j e^{-i\omega t}\int_S \phi_j \varepsilon_{ijk} r_i n_j dS\right\} \quad (35)$$

for j=1, 3, 5
i=5

where ε_{ijk} is the permutation symbol. Force in the surge and heave direction is denoted by i= 1 and 3, respectively. Moment in the pitch direction is denoted by i=5. Motion in the surge, heave, and pitch directions is denoted by j=1, 3, and 5, respectively. The first terms in Eq. (34) and Eq. (35) are the hydrostatic force and moment, respectively, and the latter two terms are the hydrodynamic forces and moments. The hydrodynamic forces can further be decoupled in the diffraction and radiation forces, respectively, as shown below:

$$\vec{F} = (\vec{F}_D + \vec{F}_I) + \vec{F}_R \quad (36)$$

The total force and moment with a moment arm, $\vec{r}$, are determined by integrating the total fluid pressure over the wetted surface:

$$F_{T_i} = -\int_S p_T n_i dS \quad (37)$$

$$M_{T_k} = -\int_S p_T \varepsilon_{ijk} r_i n_j dS \quad (38)$$

The total fluid pressure is calculated by applying Eq. (37) to the linearized Euler's integral.

$$p_T = \Re\left\{-\rho\left(gz + \frac{\partial \Phi_T}{\partial t}\right)\right\} = -\rho g z - \rho \Re\left\{\left((\phi_D + \phi_I) + \sum_j \xi_j \phi_j\right)(-i\omega)e^{-i\omega t}\right\} \quad (39) \quad \text{for j=1,3,5}$$

3.3.1 Hydrostatic Forces and Moments

The hydrostatic force is:

$$\vec{F}_H = -\rho g \iint_S z\vec{n} dS \quad (40)$$

The hydrostatic moment is:

$$\vec{M}_H = -\rho g \int_S z(\vec{r} \times \vec{n}) dS \quad (41)$$

The hydrostatic force and moment largely describe the buoyancy force and moment, which is canceled for an unrestrained body by its weight (Newman, 1977). The buoyancy term

results from the increase in pressure with depth applying an upward force on a body. Evaluating the integrand at $0<z<\eta$ results in higher order terms, and are thus neglected.

3.3.2 Diffraction Problem

The diffraction problem considers a fixed body impinged by an incident wave, which is diffracted by the body. The diffraction potential describes only the diffracted waves. Thus, the total potential is obtained by superimposing the incident and diffraction potentials:

$$\Phi_T = \Phi_I + \Phi_D \quad (42)$$

Applying the incident potential to the linearized Euler's integral and integrating the pressure over the wetted surface area results in the Froude-Krylov force. Similarly, applying the diffraction potential to the linearized Euler's integral and integrating the pressure over the wetted surface area results in the diffraction force. Superimposing the Froude-Krylov and diffraction force results in the total excitation force. The excitation force per unit wave amplitude is:

$$F_{w_i} = -\rho \Re\left\{ -i\omega e^{-i\omega t} \int_S (\phi_D + \phi_I) n_i dS \right\} \quad (43)$$

Rewriting Eq. (44) in terms of the complex amplitude of the excitation force, X_i, results in:

$$F_{w_i} = -\Re\left\{ i\omega X_i e^{-i\omega t} \right\} \quad (44)$$

where,

$$X_i = -\rho \int_S (\phi_D + \phi_I) n_i dS \quad (45)$$

Similarly, the excitation moment per unit wave amplitude is:

$$M_{w_k} = -\rho \Re\left\{ -i\omega e^{-i\omega t} \int_S (\phi_D + \phi_I)\varepsilon_{ijk} r_i n_j dS \right\} \quad (46)$$

3.3.3 Radiation Problem

The radiation problem considers a body oscillating via an external force in calm water. As the body enters the water, a wave is radiated. The radiation force per unit amplitude in the i[th] component due to the motion in the j[th] direction is:

$$F_{R_i} = -\rho \Re\left\{ \sum_j -i\omega e^{-i\omega t} \xi_j \int_S \phi_j n_i dS \right\} \quad (47)$$

Recall that the body boundary condition for the radiation potential may be written as:

$$\frac{\partial \phi_i}{\partial n} = n_i \qquad \text{on S}$$

Surge, heave, and pitch, are denoted by i and j=1, 3 and 5. Thus, Eq. (47) may be rewritten as:

$$F_{R_i} = -\rho \Re\left\{ \sum_j -i\omega e^{-i\omega t} \xi_j \int_S \frac{\partial \phi_i}{\partial n} \phi_j dS \right\} \quad (48)$$

where, Eq. (48) may be rewritten in terms of the complex force in the i[th] direction due to motion of unit amplitude in the j[th] direction (Newman, 1977):

$$F_{R_i} = -\Re\left\{ \sum_j e^{-i\omega t} \xi_j f_{ij} \right\} \quad (49)$$

Let,

$$f_{ij} = -\rho(-i\omega)\int_S \frac{\partial \phi_i}{\partial n} \phi_j dS = -\omega^2 M_{ij} - i\omega B_{ij} \quad (50)$$

$$U_j = \Re\left(-i\omega \xi_j e^{-i\omega t}\right) \quad (51)$$

Thus, Eq.(49) may be written as:

$$F_{R_i} = \left\{ -\sum_j (M_{ij}\dot{U}_j + B_{ij}U_j) \right\} \quad (52)$$

where, B_{ij} denotes the damping coefficient, which represents a reduction in harmonic oscillation via energy extraction. The variable M_{ij} denotes the added-mass coefficient, which describes the inertial and mass forces. Note B_{ij} and M_{ij} are symmetric tensors as given in Appendix A. M_{ij} and B_{ij} are functions of frequency of oscillation, the geometry, displacement, water depth, and distancing to surrounding bodies.

Damping Coefficient for a two-dimensional single, heaving body

Recall the boundary conditions are at the seabed, the body, and positive and negative infinity along the x-axis. The derivation is given in Appendix A. The damping coefficient for a two-dimensional, heaving body is:

$$B_{ij} = \frac{\rho g C_g \left(|\alpha_+|^2 + |\alpha_-|^2 \right)}{\omega^2} \quad (53)$$

3.3.4 Haskind-Hanaoka Relationship

When the diffraction potential is unknown, the excitation force may still be calculated if the radiation and incident potentials are known using the Haskind-Hanaoka relationship (Newman, 1977). Recall the complex amplitude of the excitation force per unit wave amplitude is:

$$X_i = -\rho \int_S (\phi_D + \phi_I) n_i dS \quad (54)$$

Due to Kirchhoff decomposition, recall:

$$n_i = \frac{\partial \phi_i}{\partial n}$$

Additionally, recall the total potential must satisfy the body boundary condition:

$$\frac{-\partial \phi_I}{\partial n} = \frac{\partial \phi_D}{\partial n} \qquad \text{on S}$$

Applying Eq. (13) to Eq. (54) the complex amplitude of the excitation force results in:

$$X_i = -\rho \int_S (\phi_I + \phi_D) \frac{\partial \phi_i}{\partial n} dS \qquad (55)$$

$$X_i = -\rho \int_S \phi_I \frac{\partial \phi_i}{\partial n} + \phi_i \frac{\partial \phi_D}{\partial n} dS \qquad (56)$$

Substituting Eq. (11) into Eq. (56), the complex amplitude of the excitation force per unit wave amplitude is:

$$X_i = -\rho \int_S \left(\phi_I \frac{\partial \phi_i}{\partial n} - \phi_i \frac{\partial \phi_I}{\partial n} \right) dS \qquad (57)$$

Complex amplitude of the excitation force for a two-dimensional single, heaving body

The spatial part of the complex incident and radiation potentials in two-dimensions are:

$$\phi_I = \frac{-gAi}{\omega} \frac{\cosh(k(z+d))}{\cosh(kd)} e^{ikx}$$

$$\phi_R = \frac{-g\alpha_+ i}{\omega} \frac{\cosh(k(z+d))}{\cosh(kd)} e^{-ikx}$$

As given in Appendix A, by use of the Haskind-Hanaoka relationship, the complex amplitude of the excitation force for a two-dimensional body is:

$$|X_i| = \frac{2\rho A \alpha_+ g C_g i}{\omega} \qquad (58)$$

3.4 Equations of Motion

The equations of motion for a freely-floating, stable body are derived from equating Eq. (34) with Newton's second law of physics, $F_{T_i} = m_{ij}\ddot{\xi}_j$. The mass matrix, m_{ij}, for a two-dimensional body is:

$$m_{ij} = \begin{bmatrix} m & 0 & 0 \\ 0 & m & 0 \\ 0 & 0 & I_{22} \end{bmatrix}$$

where, m denotes the mass of the body and I_{22} denotes the mass moment of inertia with respect to the z-axis. Rewrite Eq. (34) as:

$$F_{T_i} = m_{ij}\ddot{\xi}_j = -k_{ij}\xi_j + X_j e^{-i\omega t} - M_{ij}\ddot{\xi}_j - B_{ij}\dot{\xi}_j$$

where, k_{ij} is the hydrostatic stiffness matrix. Thus, the time-dependent equations of motion per unit wave amplitude assuming harmonic oscillation is:

$$X_i e^{-i\omega t} = (m_{ij} + M_{ij})\ddot{\xi}_j + B_{ij}\dot{\xi}_j + k_{ij}\xi_j \quad (59) \quad \text{for j=1, 3, 5}$$

The amplitude of the motion is written in terms of the complex amplitude of motion, $\xi_j^{\,0}$:

$$\xi_j = \xi_j^0 \cdot e^{-i\omega t}$$

The equation of motion in the frequency domain per unit wave amplitude is:

$$\xi_j^{\,0} = \sum \frac{X_i}{\left[-\omega^2(m_{ij} + M_{ij}) - i\omega B_{ij} + (k_{ij})\right]} \quad (60) \qquad \text{for j=1, 3, 5}$$

3.5 Wave Energy

The total energy per unit area depth-averaged is:

$$TE = KE + PE = \frac{\rho}{2}\int_{-d}^{0}\frac{1}{2}V^2 dz + \frac{\rho}{L}\int_{0}^{L}\int_{0}^{A\sin(kx)} gzdzdx \qquad (61)$$

Note harmonic waves can either be time-averaged or averaged over a wavelength. The potential energy due to wave motion is only applicable at $0<z<\eta$. The potential energy is the work done to elevate the fluid particles from wave trough to crest (Falnes, 2007). The potential energy per unit surface area is (Newman, 1977):

$$PE = \frac{\rho}{L}\int_{0}^{L}\int_{0}^{A\sin(kx)} gzdzdx = \frac{\rho g A^2}{2L}\int_{0}^{L}\sin^2(kx)dx \qquad (62)$$

$$PE = \int_{0}^{2\pi}\frac{\rho g A^2}{2kL}\sin^2(kx)d(kx)$$

$$\int_{0}^{2\pi}\sin^2(kx)d(kx) = \pi$$

$$PE = \frac{\rho g H^2}{16} \qquad (63)$$

The kinetic energy is due to the moving fluid (Falnes, 2007). The kinetic energy term is applicable at $-d<z<\eta$, however, the higher-order terms are neglected. Thus, the kinetic energy per unit surface area is evaluated at $-d<z<0$ (Newman, 1977):

$$KE = \frac{\rho}{2}\int_{-d}^{0}(u^2 + w^2)dz \qquad (64)$$

$$\varphi_I = \frac{Ag}{\omega}e^{kz}\sin(kx)$$

$$u = \frac{\partial\varphi}{\partial x} = \frac{gAk}{\omega}e^{kz}\cos(kx)$$

$$w = \frac{\partial\varphi}{\partial z} = \frac{gAk}{\omega}e^{kz}\sin(kx)$$

$$KE = \frac{\rho g^2 A^2 k^2}{2\omega^2} \int_{-d}^{0} e^{kz} dz$$

$$KE = \frac{\rho H^2 g}{16} \qquad (65)$$

The average potential and kinetic energy are equal, following the principle of equipartition of energy. Thus, the total energy per unit surface area is:

$$TE = \frac{\rho H^2 g}{8} \qquad (66)$$

3.6 Power Flux

Power flux is the time derivative of the energy flux. The power flux of the incident wave is:

$$P_w = \frac{dE}{dt} = \rho \frac{d}{dt} \int_{\forall} \left(\frac{1}{2} V^2 + gz \right) d\forall = \rho \int_{\forall} \frac{\partial}{\partial t} \left(\frac{1}{2} V^2 + gz \right) d\forall + \rho \int_{S} \left(\frac{1}{2} V^2 + gz \right) U_n dS \qquad (67)$$

where, U_n is the normal velocity of the vertical surface of the water column (Newman, 1977). If the column moves at a constant velocity then the energy entering and leaving the column is equal, and thus the last term of Eq. (67) is null (Newman, 1977). The vertical position is time independent, thus the latter term in the final volume integrand of Eq. (67) is also null.

$$P_w = \rho \int_{\forall} \frac{\partial}{\partial t} \left(\frac{1}{2} V^2 \right) d\forall = \rho \int_{\forall} \frac{\partial}{\partial t} \left(\frac{1}{2} \nabla \Phi_I \cdot \nabla \Phi_I \right) d\forall \qquad (68)$$

where,

$$\frac{\partial}{\partial t} \left(\frac{1}{2} \nabla \Phi_I \cdot \nabla \Phi_I \right) = \nabla \Phi_I \cdot \nabla \frac{\partial \Phi_I}{\partial t} = \frac{\partial \Phi_I}{\partial t} \nabla^2 \Phi_I + \nabla \Phi_I \cdot \nabla \frac{\partial \Phi_I}{\partial t} - \frac{\partial \Phi_I}{\partial t} \nabla^2 \Phi_I = \nabla \cdot \left(\frac{\partial \Phi_I}{\partial t} \nabla \Phi_I \right) - \frac{\partial \Phi_I}{\partial t} \left(\nabla^2 \Phi_I \right)$$

The last term vanishes due to Laplace's equation, $\nabla^2 \Phi_I = 0$. Thus, Eq. (68) is:

$$P_w = \rho \int_{\forall} \nabla \cdot \left(\frac{\partial \Phi_I}{\partial t} \nabla \Phi_I \right) d\forall \qquad (69)$$

Applying Gauss's divergence theorem to Eq. (69) results in:

$$P_w = -\rho \int_S \frac{\partial \Phi_I}{\partial t} \frac{\partial \Phi_I}{\partial n} dS \qquad (70)$$

If the column moves with a constant velocity along the x-axis, the power flux of the incident wave across a fixed control surface is:

$$\frac{\partial \Phi_I}{\partial t} = -Ag \frac{\cosh(k(z+d))}{\cosh(kd)} \cos(kx - \omega t)$$

$$\frac{\partial \Phi_I}{\partial x} = \frac{Agk}{\omega} \frac{\cosh(k(z+d))}{\cosh(kd)} \cos(kx - \omega t)$$

Thus:

$$P_w = \frac{\rho g^2 A^2 k}{2\omega} \frac{1}{\cosh^2(kd)} \int_{-d}^{0} \cosh^2(k(z+d)) dz \quad (71)$$

Note higher order terms are neglected, and thus, the power of the wave is integrated from -d to 0 with respect to the z-axis.

$$\langle P_w \rangle = \frac{\rho g^2 A^2}{2\omega} \frac{\tanh(kd)}{2} \left(1 + \frac{2kd}{\sinh(2kd)}\right)$$

$$\langle P_w \rangle = \frac{\rho g A^2}{2} C_g = \frac{\rho g H^2}{8} C_g \qquad (72)$$

3.7 Absorbed Wave Power

The time-averaged wave power absorbed for a single, heaving body is[2] (Evans, 1976):

$$\langle P \rangle = \frac{1}{T} \int_0^T \Re\{(X + F_r) e^{-i\omega t}\} \Re\{U_o e^{-i\omega t}\} dt \qquad (73)^3$$

where,

$$U = \Re(U_o e^{-i\omega t})$$

Thus,

---

[2] The superimposed bar indicates a complex conjugate

[3] < > indicates a time averaged term

$$\langle P \rangle = \frac{1}{2} \Re\left\{ (X + F_r)\overline{U_o} \right\}$$

As previously defined:

$$F_r = (-BU_o - M\dot{U}_o)$$

$$\langle P \rangle = \frac{1}{2} \Re\left\{ (X + (-BU_o - M\dot{U}_o))\overline{U_o} \right\}$$

$$\left\langle \dot{U}_o U_o \right\rangle = 0$$

Thus,

$$\langle P \rangle = \frac{1}{2} \Re\left\{ X\overline{U_o} \right\} - \frac{1}{2} BU_o\overline{U_o}$$

$$\langle P \rangle = \frac{X\overline{X}}{8B} - \frac{B}{2}\left(U_o - \frac{X}{2B} \right)\left(\overline{U_o} - \frac{\overline{X}}{2B} \right) \qquad (74)$$

The real interest is to optimize the power, thus the latter term should go to zero so that $\langle P \rangle$ is maximized. Therefore, the maximum absorbed power is:

$$\langle P \rangle_{\max} = \frac{|X_i|^2}{8B_{ij}} \qquad (75)$$

Maximum power absorption occurs at:

$$U_j = \frac{X_i}{2B_{ij}} \qquad (76)$$

Maximum power absorbed for a two-dimensional, heaving body

Recall

$$B_{ij} = \frac{\rho g C_g}{\omega^2}\left(|\alpha_+|^2 + |\alpha_-|^2 \right)$$

$$X_i = \frac{2\rho g A \alpha_+ C_g i}{\omega}$$

Thus,

$$\langle P \rangle_{\max} = \frac{1}{2}\rho g A^2 C_g \frac{|\alpha_+|^2}{\left(|\alpha_+|^2 + |\alpha_-|^2\right)} \qquad (77)$$

3.8 Maximum Power Absorption Efficiency

The goal of this thesis is to study the maximum power absorption efficiency for variously shaped bodies. The maximum power absorption efficiency, λ, is the ratio of mean power absorbed by the body to the mean power in unit crest length of a regular wave-train.

$$\lambda = \frac{P_{\max}}{P_w} \qquad (78)$$

Maximum Power absorption efficiency for a two-dimensional single, heaving body

Combinng Eq. (72), Eq. (77), and Eq. (78) reults in the maximum power absportion efficiency for a two-dimensional, single, heaving body:

$$\lambda = \frac{|\alpha_+|^2}{\left(|\alpha_+|^2 + |\alpha_-|^2\right)} \qquad (79)$$

It is apparent from Eq. (79) that directionality of the radiated wave is desirable. With a symmetric body, the radiated wave amplitude will be equal at positive and negative infinity, thus reducing the maximum power absorption efficiency to 50% (Falnes, 2007). However, if the wave is only radiated in the positive direction the maximum power absorption efficiency is theoretically 100% (Falnes, 2007). This directionality of the radiated wave accounts for the success of Salter's Duck, and is further explored in this work (Falnes, 2007).

CHAPTER 4. NUMERICAL SIMULATIONS

The software package AQWA v.14.0 by ANSYS is used to analyze the diffraction problem for a single, two-dimensional body impinged by a regular, harmonic, linear wave. AQWA applies the Green Function Method to solve for hydrodynamic and hydrostatic quantities. More specifically, AQWA-LINE evaluates the linear response of a fixed body subjected to regular, linear waves using diffraction theory, as presented in Chapter 3.

4.1 Numerical Procedure

AQWA is used to solve for the excitation force for 39 bodies. The excitation force is calculated as the incident wave approaches the body from 0° and 180°. Where, the excitation force measured as the wave impinges the body's curved face is denoted as 0°, and the excitation force measured as the wave impinges the body's flat face is denoted 180°. The complex amplitude of the excitation force is then used to calculate the radiated wave amplitude at positive and negative infinity with Eq. (58):

$$X_i = \frac{2\rho A \alpha_+ g C_g i}{\omega}$$

where, the group velocity is calculated using Eq. (33):

$$C_g = \frac{\omega}{k}\frac{1}{2}\left(1 + \frac{2kd}{\sinh(2kd)}\right)$$

Using the radiated wave amplitude at positive and negative infinity, the maximum power absorption efficiency is calculated with Eq. (79):

$$\lambda = \frac{\alpha_+^2}{\left(|\alpha_+|^2 + |\alpha_-|^2\right)}$$

4.2 AQWA Modeling Procedure

The user builds a project by adding and combining Analysis Systems in the ANSYS Workbench, as seen in Figure4.1. The user selects an Analysis System template from the

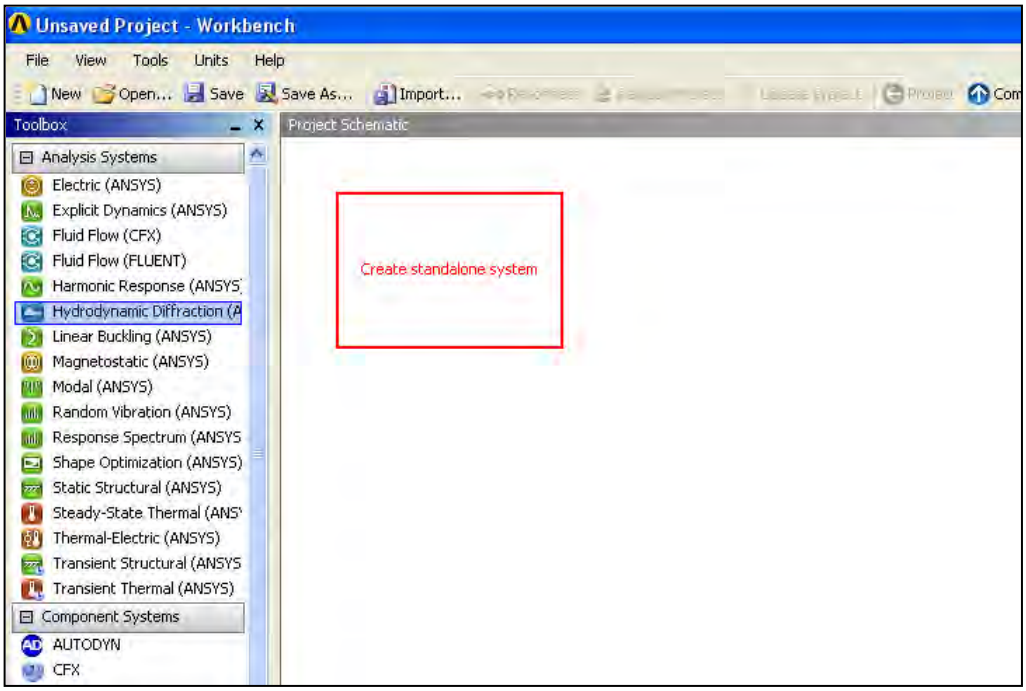

Figure 4. 1 ANSYS Workbench

Toolbox on the right-hand side of the Workbench by either dragging the system to the Project Schematic or double-clicking on the Analysis System. A green box indicates possible drop targets, which becomes red when the mouse is over a possible drop target, as seen in Figure 4.1. In this thesis the Hydrodynamic Diffraction (AQWA) system is used.

The system is a block of cells, as seen in Figure 4.2. The output from upstream cells is input data to downstream cells. Data are also shared from left to right. The user can either double-click or right-mouse click a cell to modify it. Double-clicking a cell will initiate the default action. A right-mouse click will generate a context menu, as seen in Figure 4.2.

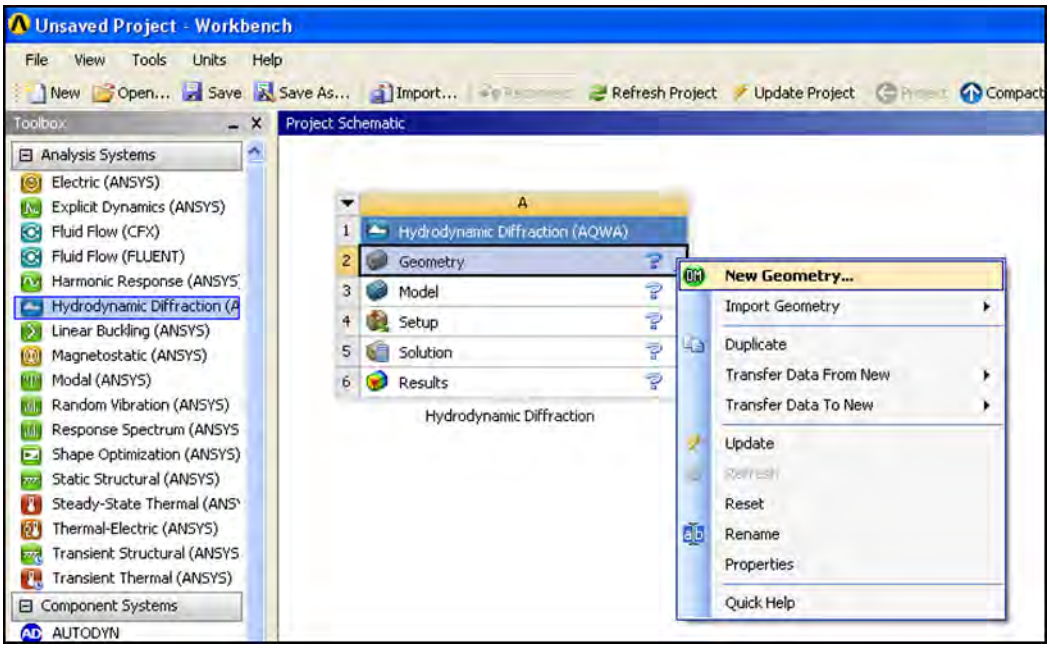

Figure 4. 2 Modifying Analysis System Cells

If a template is added by double-clicking the system in the toolbox then it does not share information with other systems in the Workbench. Dragging a system onto the cell of a system in the Project Schematic will allow for data sharing between systems, as seen in Figure 4.3. A connection with square terminals indicates data sharing between two systems. A connection with round terminals indicates upstream data of one system is shared with downstream data of a second system.

An icon on the right side of each cell will indicate the status of the cell. The following is not an exhausted list of status icons, but includes the most common icons.

: Required upstream data does not exist.

: Upstream data is changed, and thus the cell needs to be refreshed.

: The cell's input parameters are current, but need to be corrected.

: Local data has changed, and the cell's output needs to be regenerated.

: The output is current and there are no input errors.

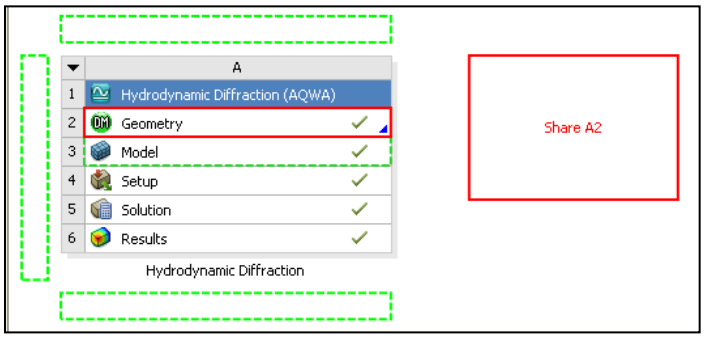

Figure 4. 3 System Data Sharing

4.2.1 Geometry Cell

Double-clicking the Geometry cell will launch a data-integrated workspace called Design Modular, as seen in Figure 4.4. In Design Modular the body is drawn, which will be imported into the mesh cell. To create the bodies the following steps are taken:

1. Select the desired units.
2. Highlight the **ZX Plane** in the **Tree Outline** and select the  icon in order to work in the ZX Plane, as seen in Figure 4.5.
3. Select the **Sketching** tab on the bottom of the Tree Outline. Note the user defines the body's position with respect to the global coordinate system when sketching the body. Additionally, the user will later specify the xy-plane as the still water level.

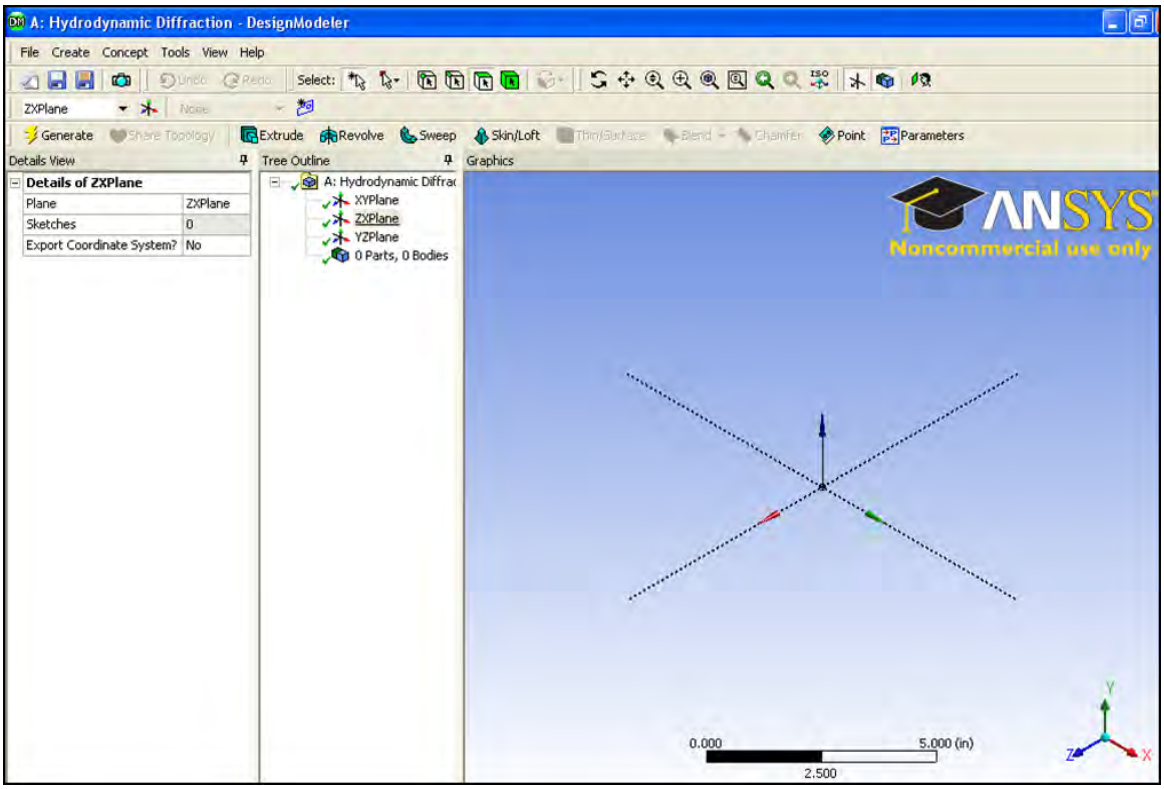

Figure 4. 4 Design Modular

4. Select the **Draw** tab and highlight **Line**, as seen in Figure 4.5.
5. Create a line and release as an H or V appears near the line to create a horizontal or vertical line, respectively, as seen in Figure 4.5. Note the x-axis appears as the vertical axis.
6. Select the **Dimensions** tab, as seen in Figure 4. 6.

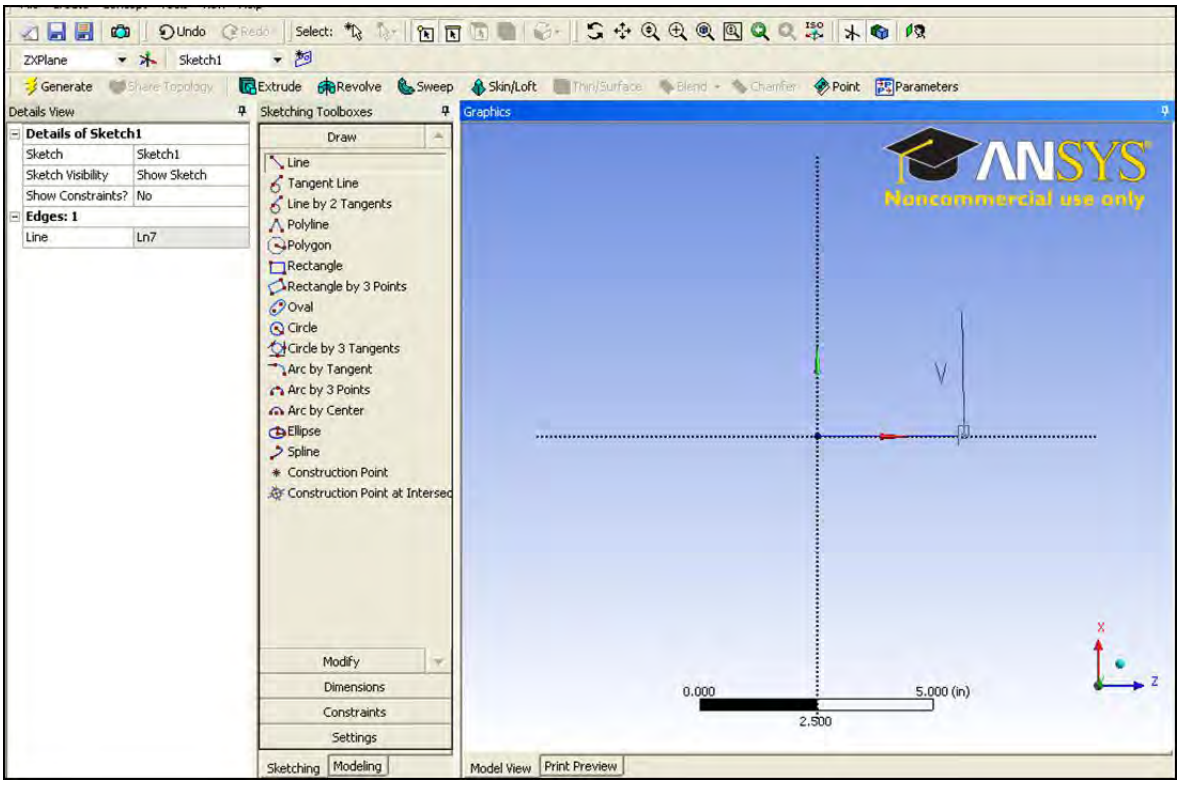

Figure 4. 5 Drawing in Design Modular

7. Highlight either **Vertical** or **Horizontal**, as seen in Figure 4.6, so as to apply an exact length to a selected line.
8. Under the **Details View** insert the desired length to the corresponding line, as seen in Figure 4.6.
9. Draw desired the shape, as seen in Figure 4.6, in increments of 0.2 in. (0.51 cm) along the z-axis. In this work all bodies have equal in drafts of 5 in. (12.7 cm) and waterline cross-sectional areas of 35.25 in.^{2} (227 cm^2).
10. Connect points along the curve using the **Spline** tool under the **Draw** tab. Note a P will appear when a point has been selected.
11. After selecting the points to connect, right-mouse click and select **Open End**, as seen in Figure 4.7.

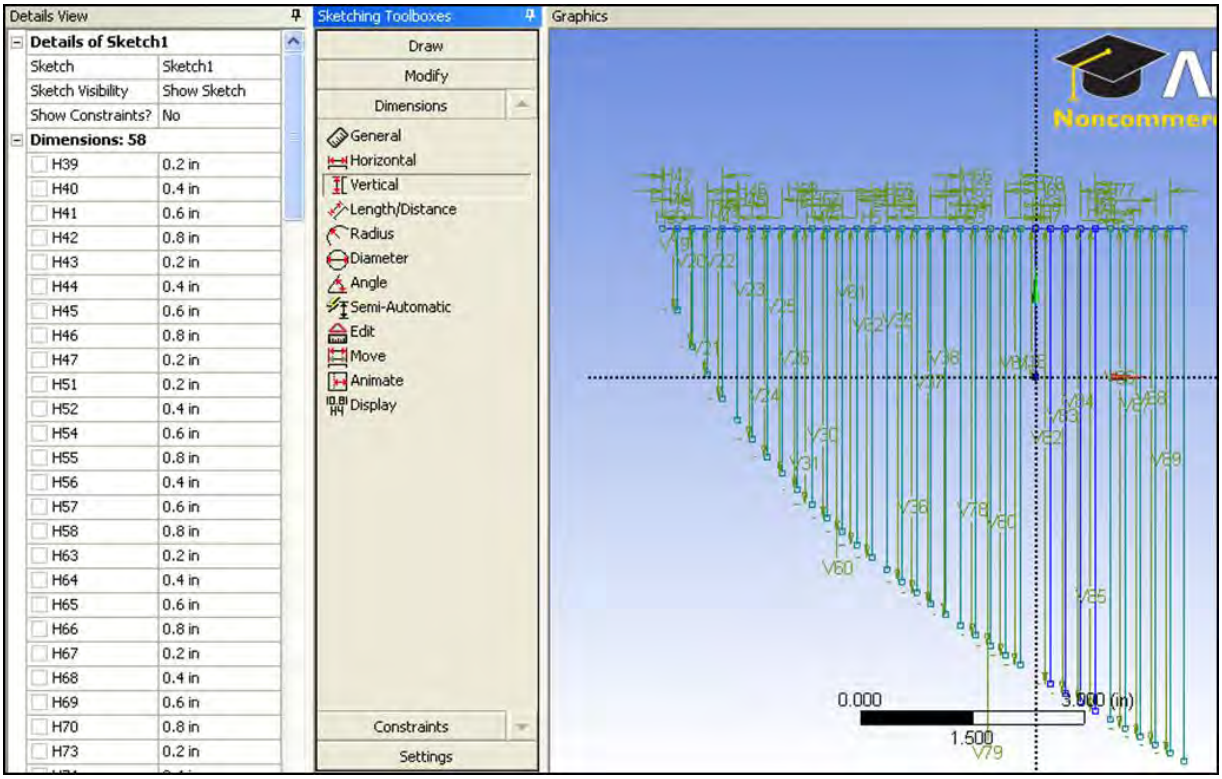

Figure 4. 6 Drawing Curved Objects

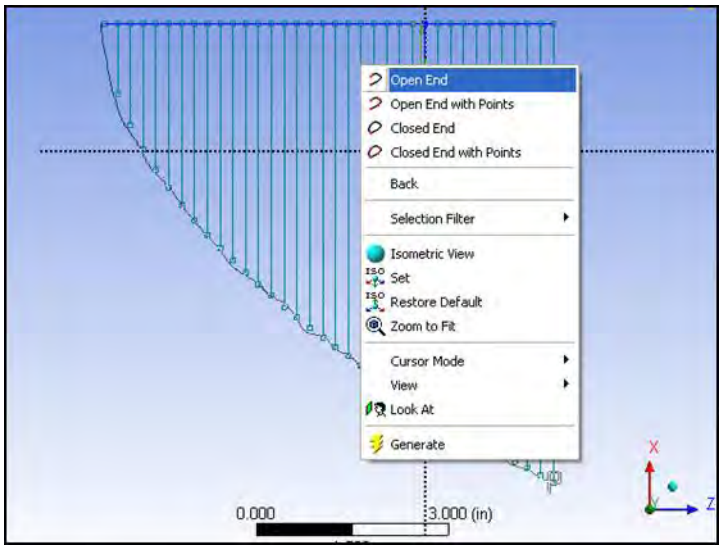

Figure 4. 7 Closing the Spline

12. Delete all lines inside the curve.

13. Return to the isometric view by selecting the 

icon.

14. Add the body's width to the body by selecting the 

icon.

15. Edit the body's width details under **Details of Extrude 1** in the **Details View**. Set the **Direction** to **Both-Symmetric**, and **Depth** to 2.9375 in. (7.46 cm), as seen in Figure 4.8.

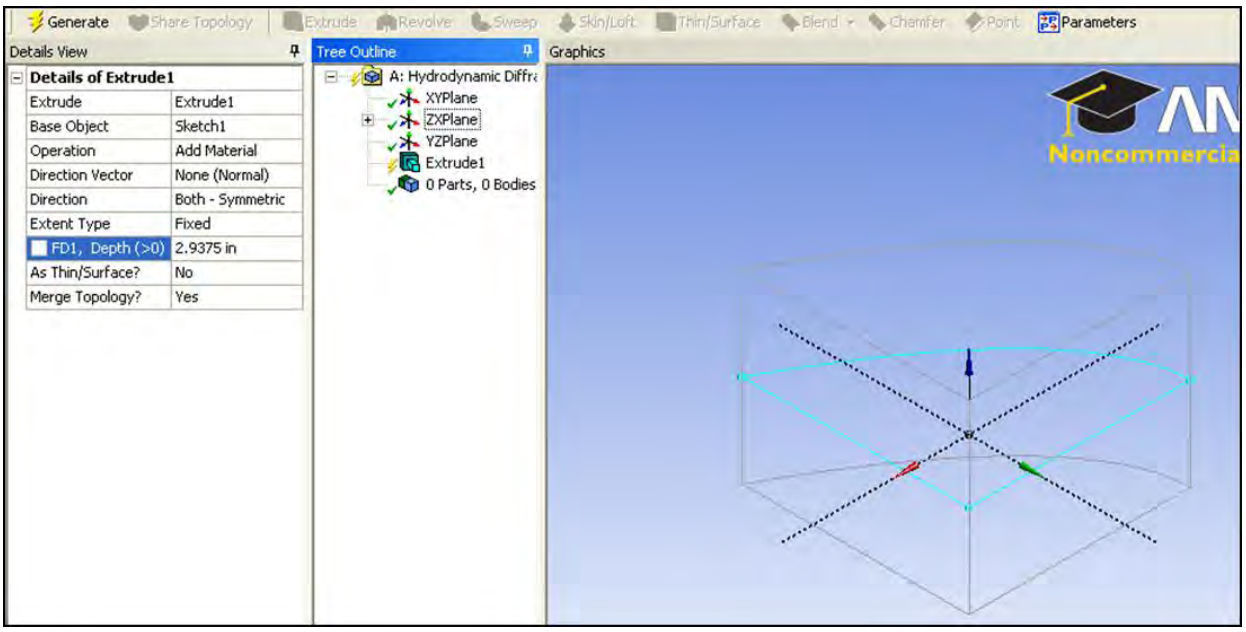

Figure 4. 8 Extruding the Body

16. After editing the **Details of the Extrude 1**, select the 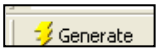

icon.

17. Create a surface rather than a body by selecting the 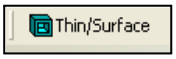

icon.

18. Edit the surface details under **Details of Thin 1**. Set the **Selection Type** to **Bodies Only**. Set the **Thickness** to 0 in., as seen in Figure 4.9. Highlight the body and select **Apply** under **Selection Type**.

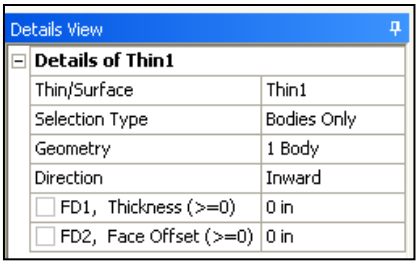

Figure 4. 9 Details of Thin

19. Select the **Generate** icon.

20. Select **Freeze** under the **Tools** menu, as seen in Figure 4.10.

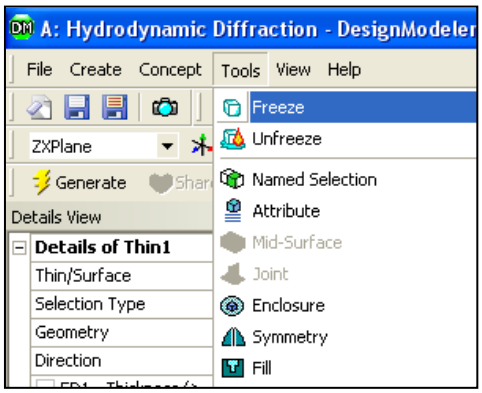

Figure 4. 10 Freezing a Body

21. Select **Slice** under the **Create** menu, as seen in Figure 4.11.

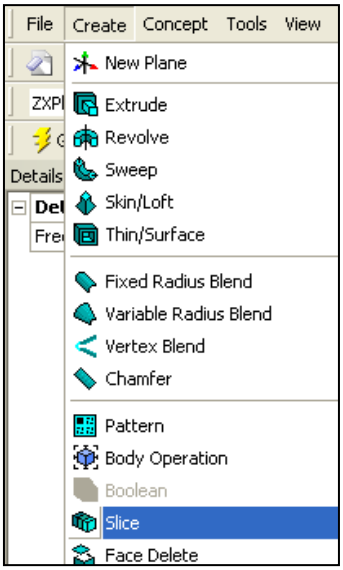

Figure 4. 11 Slicing a Body

22. Edit the details of the slice under **Details of Slice 1**. Set the **Slice Type** to **Slice by Plane**. Highlight the XY plane in the **Tree Outline** and select **Apply** under **Base Plane**, as seen in Figure 4.12. This establishes where the still water level is set.

23. Select the **Generate** icon.

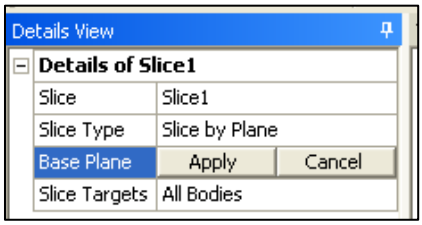

Figure 4. 12 Details of the Slice

24. Highlight the two **Surface Bodies** under **2 Parts, 2 Bodies** in the Tree Outline.

25. Right-mouse click and select **Form New Part**, as seen in Figure 4.13.

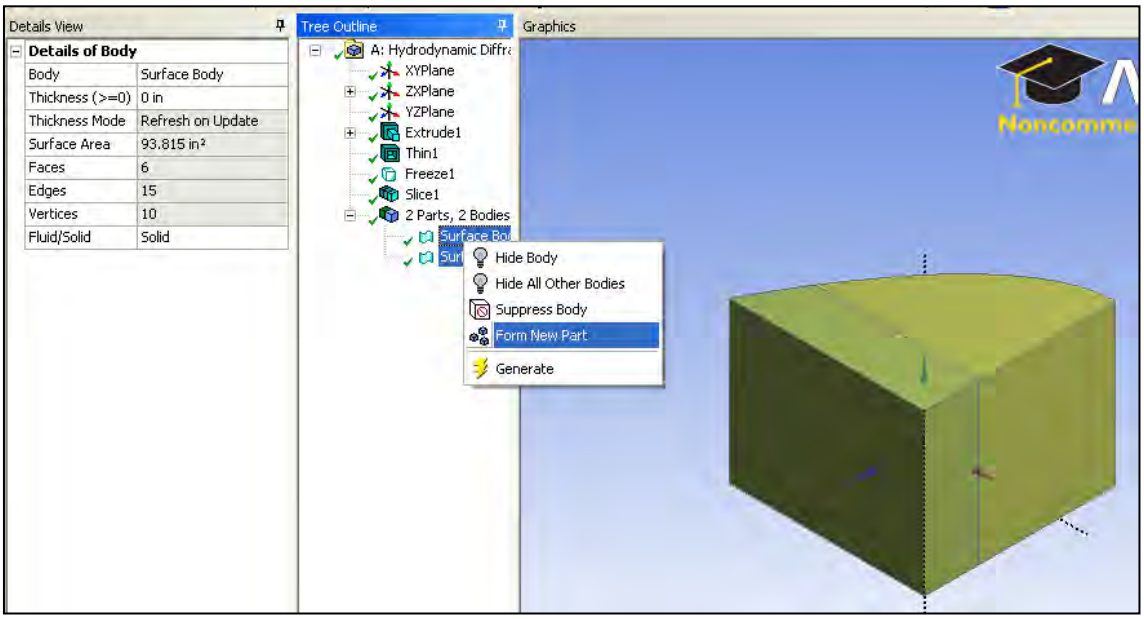

Figure 4. 13 Forming a New Part

4.2.2. Mesh Cell

1. Double-click the Mesh Cell in the Workbench to launch Hydrodynamic Diffraction (AQWA). Note the coordinate system is displayed in the lower right-hand corner.
2. Highlight **Geometry** under the Tree Outline.
3. The program will automatically import the surface body from Design Modular as indicated in **Imported Preferences** under the **Details of Geometry**, as seen in Figure 4.14.
4. Enter **Sea Geometry** details. In this work the **Sea Level** is 0 in., **Water Depth** is 11 in. (28 cm), **Water Density** is 3.7028E-2 $lb_m/in.^3$ (1025 kg/m^3), **Water Size X** is 39370 in. (100 m), and **Water Size Y** is 5.875 in. (15 cm), as seen in Figure 4.14.

Details of Geometry	
Name	Geometry
Attached Asse...	C:\Documents and Settings\cee-dell\My Do
Sea Geometry	
Water Level	0 Inches
Water Depth	11 Inches
Water Density	3.70284391823254E-02 lb/Inches³
Water Size X	39370.8 Inches
Water Size Y	5.875 Inches
Import Preferences	
Import Solid Bo...	No
Import Surface ...	Yes
Import Line Bo...	Yes

Figure 4. 14 Details of the Geometry

5. Right-mouse click on **Geometry** in the Tree Outline, which will generate a context menu, as seen in Figure 4.15. Select **Add >> Point Mass**.
6. Under **Details of Part** set **Fixity Options** to **Structure is Fixed in Place**. Thus, the program solely solves for the diffraction problem, as seen in Figure 4.15.

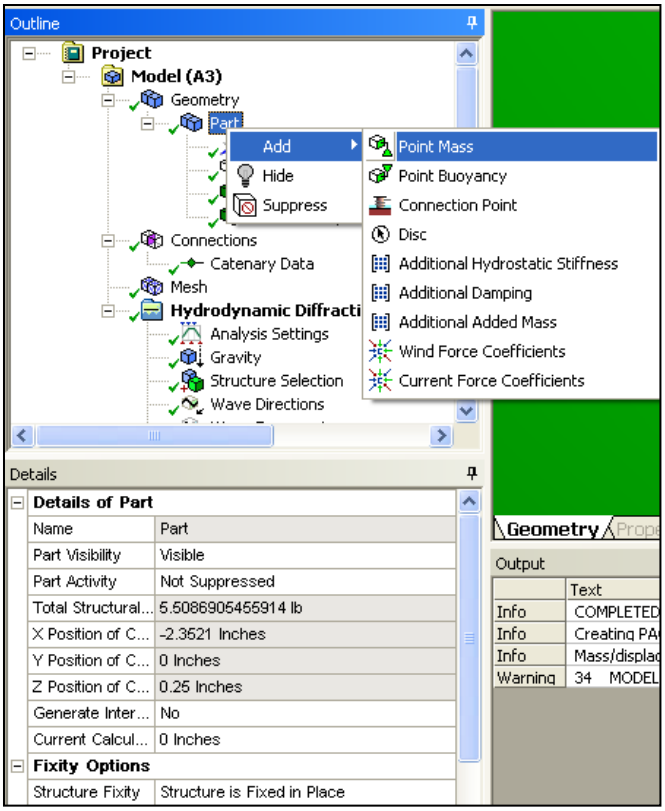

Figure 4. 15 Details of the Part

7. Highlight **Point Mass** under the Tree Outline.
8. Under **Details of Point Mass**, set **Define Mass** to **Automatic**, as seen in Figure 4.16.
9. Input the mass of the body, assuming the density of the body is 0.03417 $lb_m/in.^3$ based on the experimental bodies.
10. Under **X**, **Y**, and **Z** input the coordinates of the body's center of gravity with respect to the global coordinate system.
11. Under **Define Inertia Values By** select **Direct input of Inertia**.
12. Under $\mathbf{I_{xx}}$, $\mathbf{I_{yy}}$, and $\mathbf{I_{zz}}$ input the moments of inertia of the body rotated about the x, y, and z-axis at the center of gravity.

Note the input for moment of inertia, center of gravity position, and mass do not affect the diffraction problem. However, the user should be careful when entering these value if solving for the radiation problem.

Details of Point Mass	
Name	Point Mass
Visibility	Visible
Activity	Not Suppressed
X	-2.3521 Inches
Y	0 Inches
Z	0.25 Inches
Mass definition	Manual
Mass	5.5086905455914 lb
Define inertia v...	Direct input of Inertia
Kxx	2.70381240340129 Inches
Kyy	1.6960117207713 Inches
Kzz	1.35556465315197 Inches
Ixx	40.271841436074 lb.Inches²
Ixy	0 lb.Inches²
Ixz	0 lb.Inches²
Iyy	15.8455046333628 lb.Inches²
Iyz	0 lb.Inches²
Izz	10.122524768913 lb.Inches²

Figure 4. 16 Details of the Point Mass

13. Under **Details of Mesh** set **Defeaturing Tolearance** to 0.02 in. (0.051 cm) and **Max Allowed Frequency** to 2.1 Hz (0.47 sec), as seen in Figure 4. 17.
14. The **Max Element Size** must be less than 1/7 the largest wavelength, which is automatically updated by the program based on the Max Allowed Frequency and the depth.
15. Set **Meshing Type** to **Program Controlled**.
16. Select the 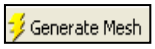

icon.

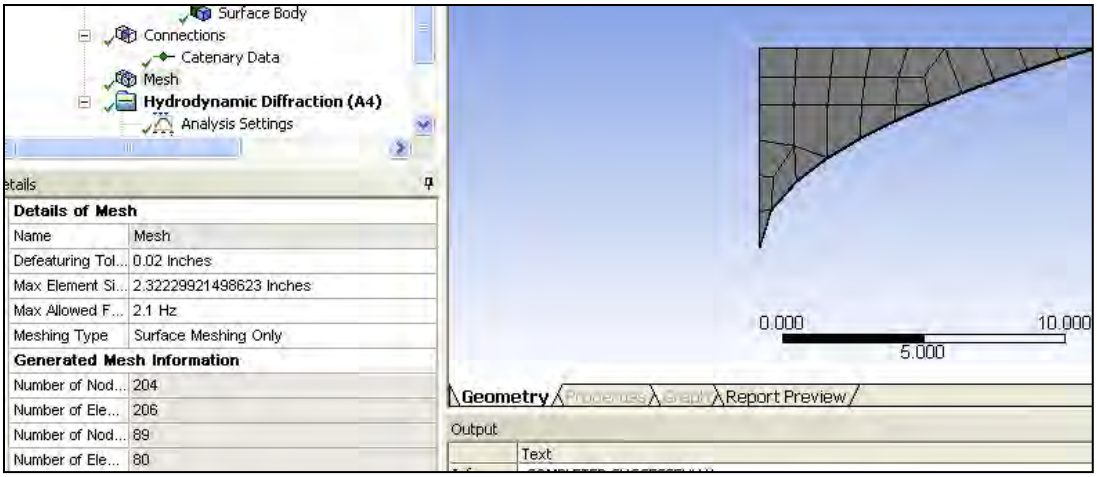

Figure 4. 17 Details of the Mesh

4.2.3 Set-up Cell

To input data for the Set-up cell remain in Hydrodynamic Diffraction (AQWA).

1. Highlight **Analysis Settings** under the Tree Outline.
2. Select **Yes** under **Ignore Modeling Rule** in the **Common Analysis Options** menu as seen in Figure 4.18. Thus, allowing the body to disregard the following numerical rules :
    a. The center of a diffraction plate should be greater than half the element characteristic radius from the seabed, which is dependent on the draft and depth. The element characteristic radius is calculated by equating the actual area to that of a circular element of equal area:

$$r_e = \sqrt{\frac{\pi}{area}}$$

    b. Adjacent diffraction plate elements, i.e. elements that have a common side, should have an area ratio greater than 1/3.

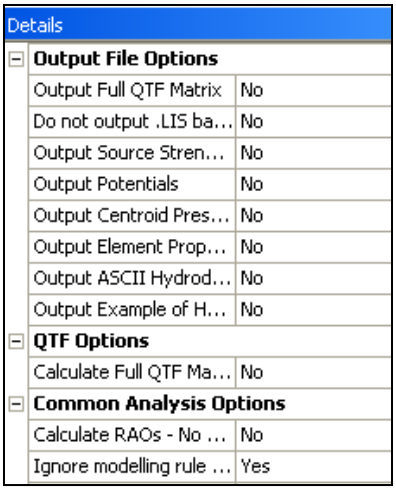

Figure 4. 18 Details of the Analysis Settings

3. Set **Gravity** to 386.09 in./sec^2 (9.81 m/sec^2), as seen in Figure 4.19.

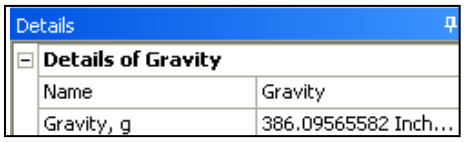

Figure 4. 19 Details of the Geometry

4. No changes are needed to **Details of Structure Selection,** as seen in Figure 4.20, the program automatcially imports the body. For future work multiple bodies may be studied by chaniging the input under Strucutre Selection.

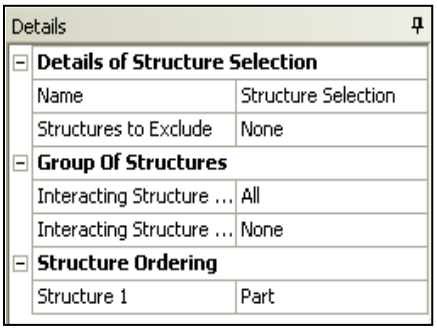

Figure 4. 20 Details of the Structure Selection

5. Under **Details of Wave Directions** set **Interval** to 180°, which will automatically update the **No. of Intermediate Directions**, as seen in Figure 4.21.

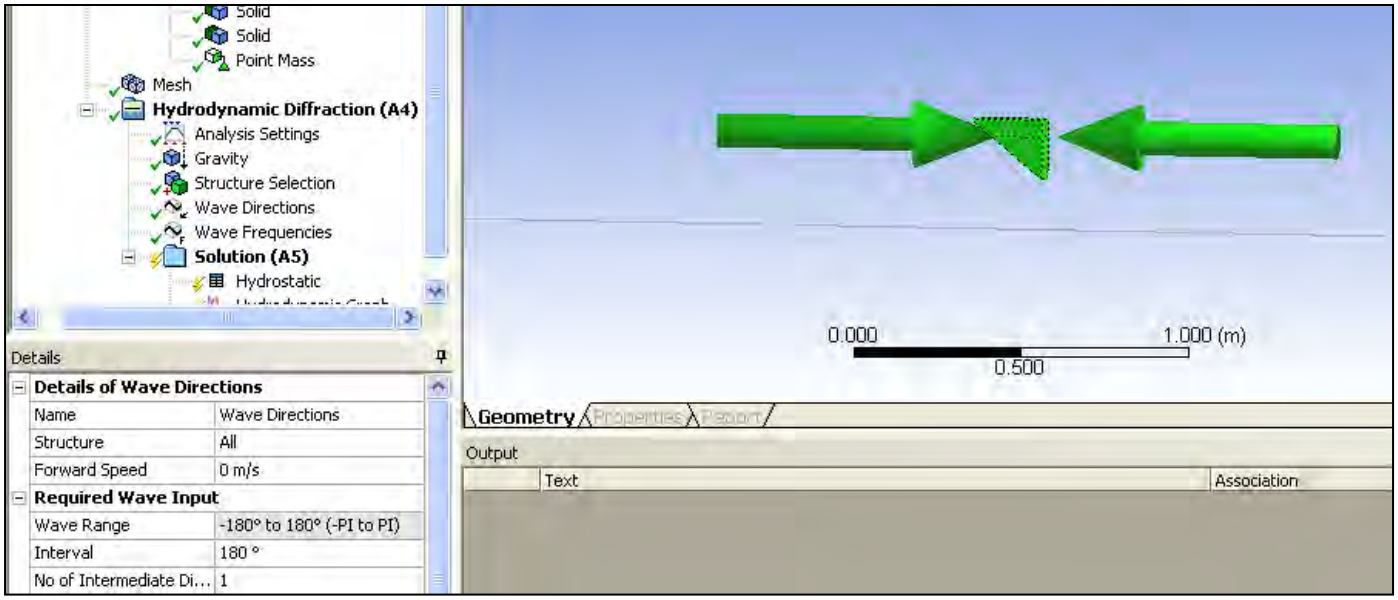

Figure 4. 21 Details of the Wave Direction

6. Under **Details of Wave Frequencies** set **Range** to **Manual Definition**, as seen in Figure 4.22.
7. Under **Definition Type** select **Range**.
8. Set the **Start Period** to 2.1 sec (0.47 Hz) and the **End Period** to 0.6 sec (1.67 Hz), as seen in Figure 4.22.
9. Set the **Interval Type** to **Period**, and set the **Interval Period** to 0.05 sec.

Details of Wave Frequencies	
Name	Wave Frequencies
Frequency / Period definition	
Range	Manual Definition
Definition Type	Range
Lowest Freque...	0.476 Hz
Longest Period	2.1 s
Highest Frequ...	1.667 Hz
Shortest Period	0.6 s
Interval Type	Period
Interval Period	0.05 s
Number of Inte...	22

Figure 4. 22 Details of the Wave Frequencies

4.2.4 Solution Cell

1. Right-mouse click on **Solutions** under the Tree Outline, as seen in Figure 4.23.
2. Select **Insert Results>> Diffraction + Froude-Krylov>> Force/Moment vs Frequency + Direction**, as seen in Figure 4.23.

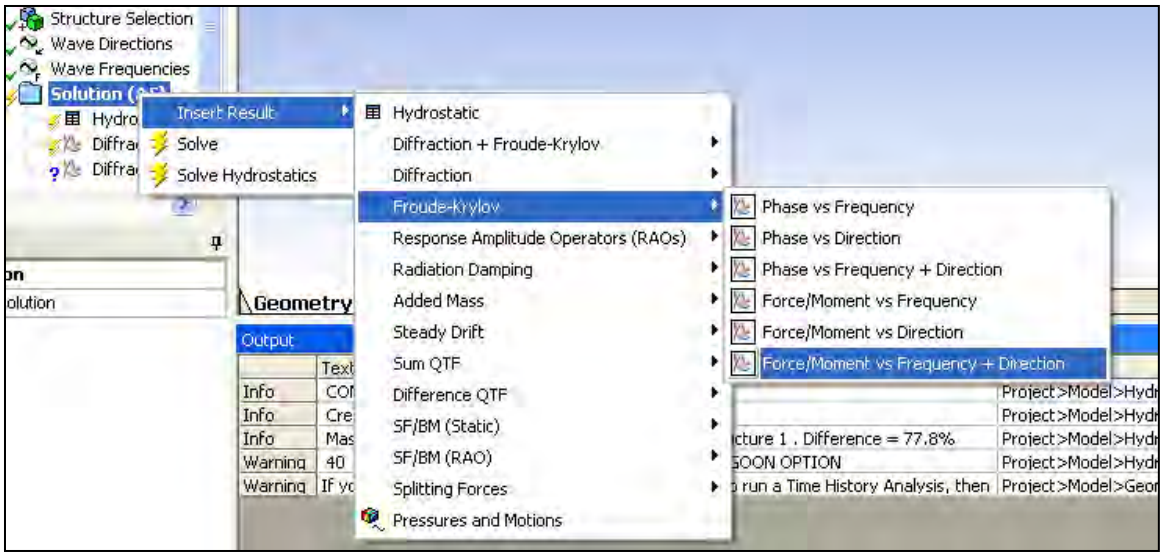

Figure 4. 23 Inserting Solutions

3. Set the **Component** to **Global Z** under **Details of Diffraction+Froude-Krylov**, as seen in Figure 4.24.

Details	
Details of Diffraction + Froude-Krylov (Force/Moment vs Frequency & Dire	
Name	Diffraction + Froude-Krylov (Force/Moment vs Frequency & Direction)
Presentation M...	Surface
Axes Selection	Force/Moment vs Frequency & Direction
Frequency or ...	Period
Surface	
Structure	Part
Type	Diffraction + Froude-Krylov
Component	Global Z

Figure 4. 24 Details of the Excitation Force Graph

4. Select the Solve icon.

5. Highlight **Diffraction + Froude-Krylov** to view results. Data under **Graph Data** may be highlighted and copied into Microsoft Excel.

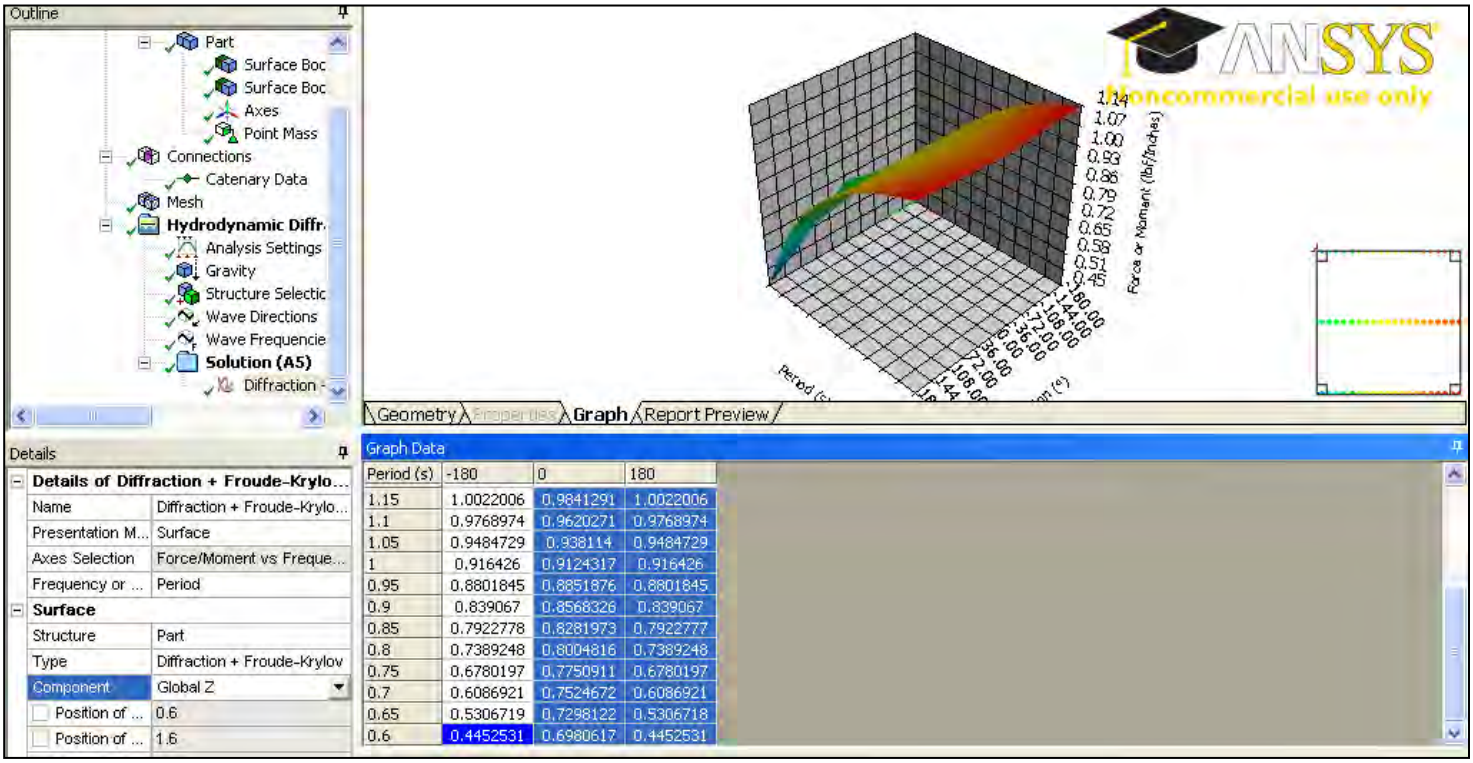

Figure 4. 25 Exciation Force Results

In the Workspace the cells should have a complete status icon, as seen in Figure 4.26.

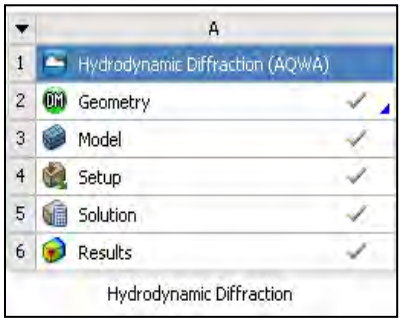

Figure 4. 26 Analysis System Complete

As seen in Figure 4.25, the forces are calculated per unit wave amplitude since the excitation force is a transfer function. To calculate the force for a particular wave height, simply

multiply the results by particular wave amplitudes. Caution is needed in doing this that the wave amplitude satisfies linear potential theory.

4.3 Numerical Validation

Results from AQWA are validated by comparing with the numerical results of Koo and Kim (2005) as well as the experimental results by Nojiri and Murayama (1975). Koo and Kim studied the diffraction problem for a two-dimensional, surface- piercing, single and dual Lewis form hull, as seen in Figure 4.27. The same single body case is analyzed with AQWA for comparison in this study. The dimensions of the body are given in Table 4.1, where B, W, and D denote the body's length, width, and draft, respectively. The width and length are taken at the still water level. The curved radius prevents turbulence from occurring. Koo and Kim used a two-dimensional numerical wave tank (NWT) based on potential theory with nonlinear free-surface boundary conditions and acceleration-potential method. Comparatively, AQWA is based on linear potential theory with linearized boundary conditions. However, for small wave amplitudes, the two models should predict the same or similar results.

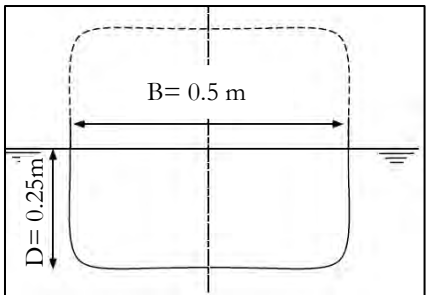

Figure 4. 27 Lewis Form Hull

Table 4.1 Body Dimensions for Numerical Validation

Length (along x-axis)	19.685 in. (0.5m)
Width (along y-axis)	39.370 in. (1.0m)
Draft	9.842 in. (0.25m)
Radius of Chamfer	2.519 in. (0.064m)

The environmental parameters tested are given in Table 4.2. Koo and Kim (2005) tested two wave heights of 0.01 m and 0.07 m to study a linear and nonlinear case, respectively. Note H_1 and H_2 denote a wave height of 0.01 m and 0.07m, respectively.

Table 4. 2 Environmental Parameters for Numerical Validation

L (m)	k (m^-1)	d (m)	ω (rad/sec)	T (sec)	H_1/L	H_2/L	B/L	ζ
7.8539	0.8000	7.8539	2.8014	2.2429	0.0013	0.0089	0.064	0.20
6.2831	1.0000	6.2831	3.1321	2.0061	0.0016	0.0111	0.080	0.25
5.2359	1.2000	5.2359	3.4310	1.8313	0.0019	0.0134	0.095	0.30
4.4879	1.4000	4.4879	3.7059	1.6954	0.0022	0.0156	0.111	0.35
3.1416	2.0000	3.1416	4.4294	1.4185	0.0032	0.0223	0.159	0.50
2.8559	2.2001	2.8559	4.6456	1.3525	0.0035	0.0245	0.175	0.55
2.6179	2.4001	2.6179	4.8522	1.2949	0.0038	0.0267	0.191	0.60
2.4166	2.6000	2.4166	5.0503	1.2441	0.0041	0.0290	0.207	0.65
2.2439	2.8001	2.2439	5.2410	1.1989	0.0045	0.0312	0.223	0.70
2.0944	3.0000	2.0944	5.4249	1.1582	0.0048	0.0334	0.239	0.75
1.5707	4.0002	1.5707	6.2642	1.0030	0.0064	0.0446	0.318	1.00
1.2566	5.0001	1.2566	7.0036	0.8971	0.0080	0.0557	0.398	1.25
1.0472	6.0000	1.0472	7.6720	0.8190	0.0095	0.0668	0.477	1.50
0.8976	7.0000	0.8976	8.2867	0.7582	0.0111	0.0780	0.557	1.75

Koo and Kim (2005) present the normalized forces versus the normalized frequencies, ζ. The normalized force is given by: $\frac{X_i}{\rho g W B (H/2)}$. The normalized frequency is given by: $\zeta = \frac{B\omega^2}{2g}$. The results from AQWA compared with the results from Koo and Kim (2005) for H_2 are given in Figure 4.28. Additionally, the results are compared with analytical results

from Maruo (1960), numerical results from Tanizawa and Minami (1998), and experimental results from Nojiri and Murayama (1975). There is an excellent agreement between the results produced by AQWA and the numerical results of Koo and Kim (2005).

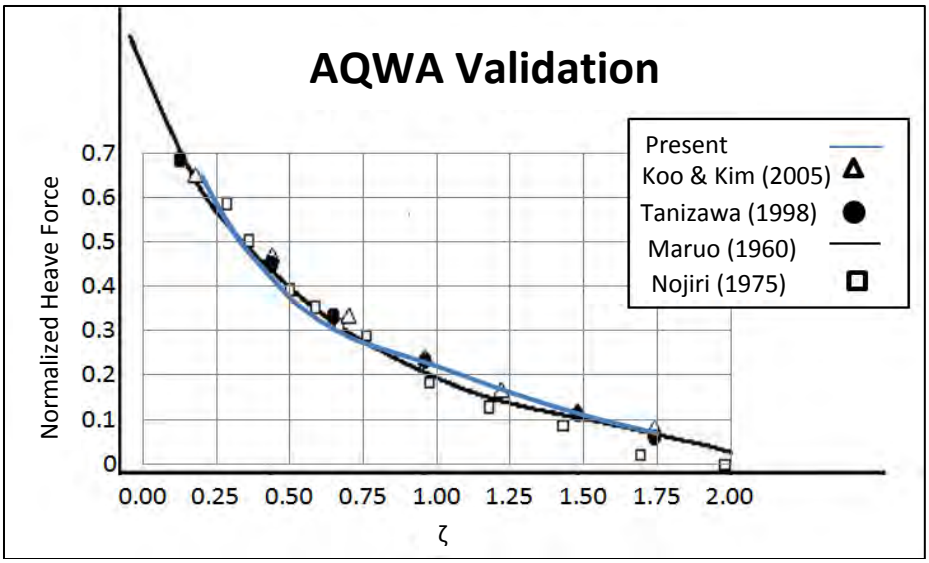

Figure 4. 28 Results for Numerical Validation

Similar to Koo and Kim's (2005) results, the present results also agree well with the experimental and analytical results for lower frequencies. There is some minor deviation between numerical and experimental results at higher frequencies. Koo and Kim (2005) attribute this deviation to viscous and other nonlinear effects, and experimental error. They also note a greater agreement with the analytical results for smaller wave heights since the second harmonic is more significant to the vertical forces as wave height increases.

4.4 Numerical Results

Numerical results given in Figure 4.29 compare the maximum power absorption efficiency with the body number, where the bodies are numbered 1 to 39 from most convex to concave. Note Body 21 is a flat edged triangular wedge. In Figure 4.29 the curve changes

concavity from concave down to concave up at Body 21. The maximum power absorption efficiency decreases more rapidly with the convex bodies than the concave. However, note from Table 4.3 and Figure 4.29 that the maximum power absorption efficiency is consistently higher for convex bodies compared to concave. At a period of 0.6 sec the maximum power absorption efficiency fall from 86.30% to 70.77% from the most convex body to the most concave body. Comparatively, at a period of 1.0 sec the maximum power absorption efficiency falls from 53.04% to 49.70% from the most convex body to the most concave body.

The wave no longer detects the shape of the body at a period of 1.0 sec (1 Hz) because the wavelengths are much greater than the body length, as seen in Figure 4.30. As previously stated for the wave to detect the body's shape the body length must span a significant portion of the wavelength. Note at a period of 1.0 sec the body spans 11% of the wavelength.

Figures 4.31 and 4.32 present the normalized heave forces versus the normalized frequencies for Bodies 1, 21, and 39 as the body is impinged at 0° and 180°, respectively. Recall the force is normalized by $\frac{X_i}{\rho g W B (H/2)}$, and the frequency is normalized by $\zeta = \frac{B\omega^2}{2g}$. Note from Figures 4.30 and 4.31 that the concave bodies consistently experience greater force than the convex bodies. Additionally, the curved faces of the bodies (0°) experience greater forces than the flat face of the bodies (180°). The percentage difference between the normalized force as the wave impinges body 1 at 0° and 180° at T = 0.6 sec is 85.91%. Comparatively ,

the percentage difference between the normalized force as the wave impinges body 1 at 0° and 180° at T = 1 sec is 6.13%. Where percentage difference is:

$$Percent\_Difference = \frac{(x-y)}{\left(\frac{(x+y)}{2}\right)}$$

Note these conclusions are restricted to the assumptions made that the waterline cross-sectional area and the draft remain constant rather than the submerged volume remaining constant. A smaller draft corresponds to larger excitation forces and greater power absorption (Backer, 2009). A smaller waterline cross-sectional area corresponds to a smaller hydrostatic resorting coefficient, and thus results in resonance occurring at a lower natural frequency, affecting the power absorption efficiency (Backer, 2009). The submerged volume will also have an effect on the hydrostatic restoring coefficient, and thus on the frequency at which resonance occurs. Thus, there is a trade-off in whether to keep the waterline cross-sectional area or the submerged volume constant. Future research should be done to further explore this issue.

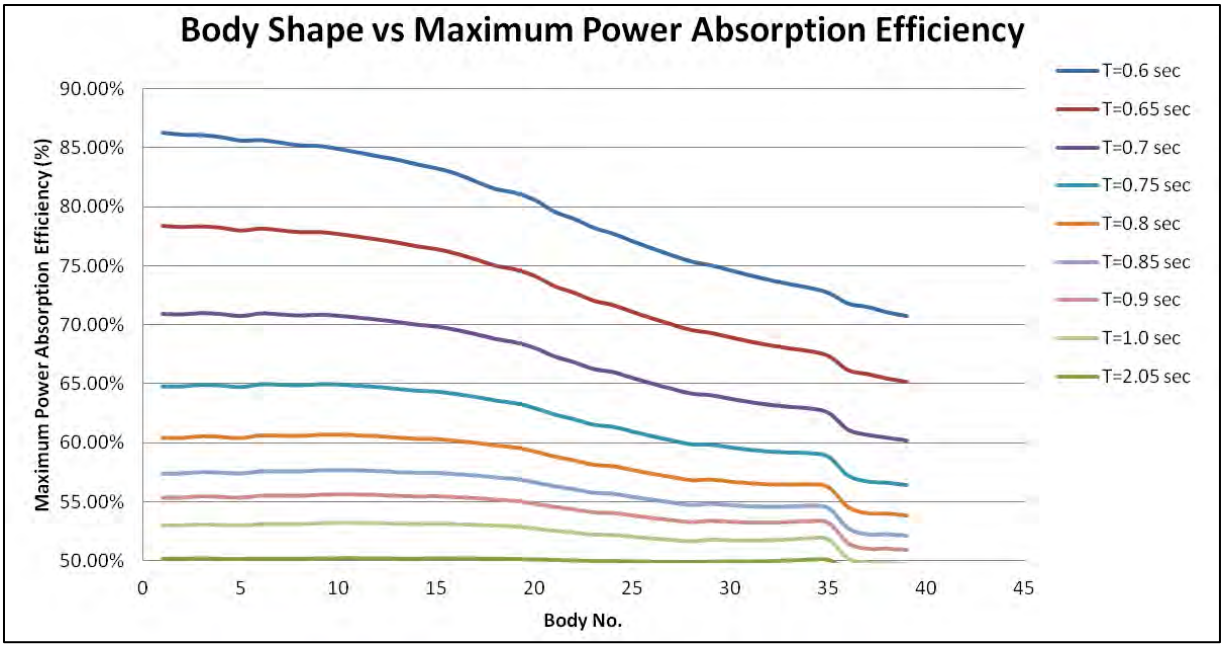

Figure 4. 29 Maximum Power Absorption Efficiency vs Body Shape

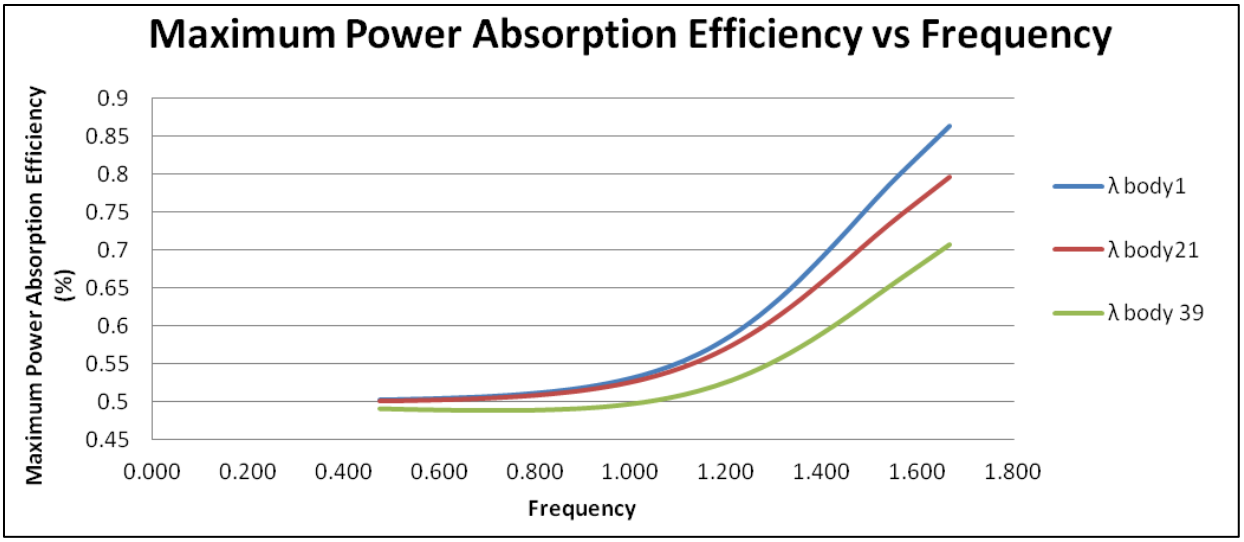

Figure 4. 30 Maximum Power Absorption Efficiency vs Frequency

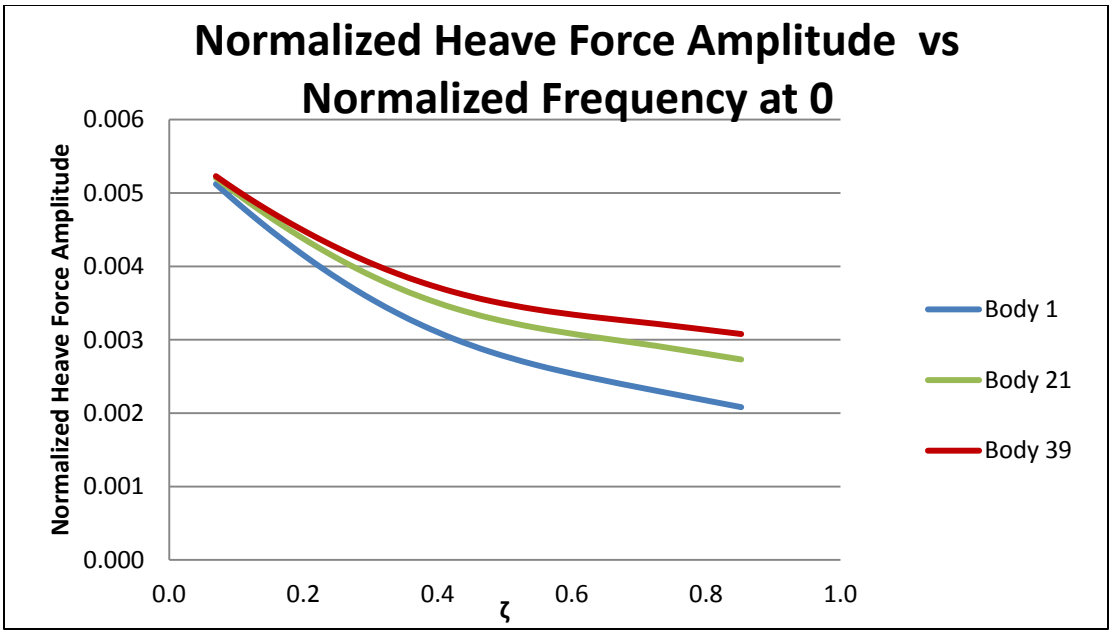

Figure 4. 31 Normalized Heave Force Amplitude vs Normalized Frequency at 0°

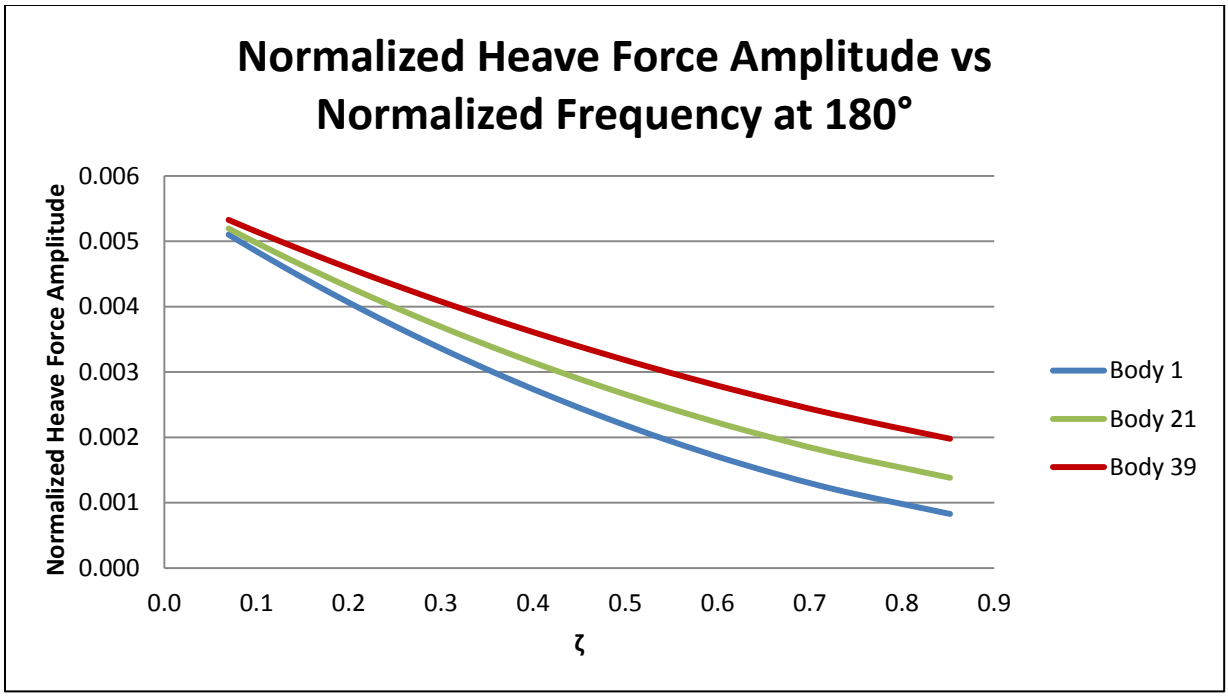

Figure 4. 32 Normalized Heave Force Amplitude vs Normalized Frequency at 180°

Table 4. 3 Numerical Results

Body No.	Body	λ at T=2.1	λ at T=1.0	λ at T=0.6	Body No.	Body	λ at T=2.1	λ at T=1.0	λ at T=0.6
1	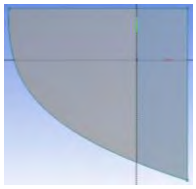	50.20%	53.04%	86.30%	8	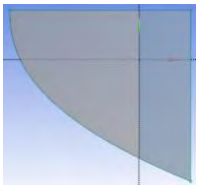	50.20%	53.16%	85.23%
2	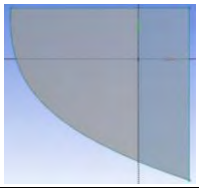	50.20%	53.05%	86.13%	9	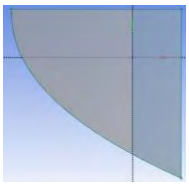	50.21%	53.23%	85.18%
3	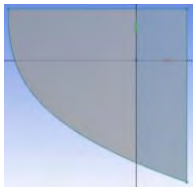	50.22%	53.14%	86.10%	10	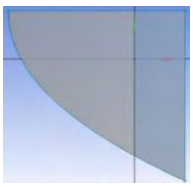	50.23%	53.27%	84.92%
4	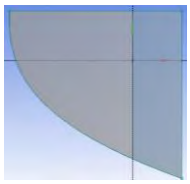	50.19%	53.08%	85.93%	11	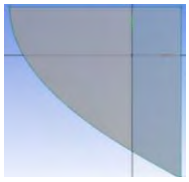	50.23%	53.25%	84.62%
5	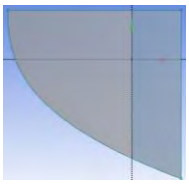	50.18%	53.04%	85.63%	12	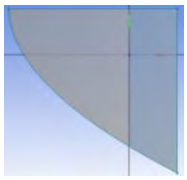	50.23%	53.24%	84.30%
6	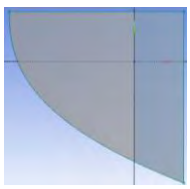	50.20%	53.16%	85.67%	13		50.21%	53.18%	84.01%
7	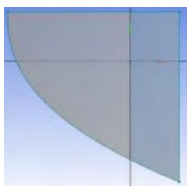	50.20%	53.16%	85.46%	14	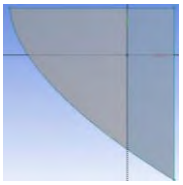	50.21%	53.16%	83.61%

Body No.	Body	λ at T=2.1	λ at T=1.0	λ at T=0.6	Body No.	Body	λ at T=2.1	λ at T=1.0	λ at T=0.6
15	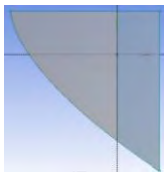	50.22%	53.19%	83.28%	22	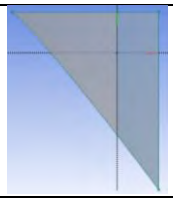	50.06%	52.42%	79.01%
16	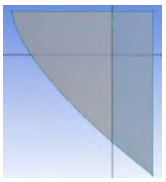	50.21%	53.14%	82.82%	23	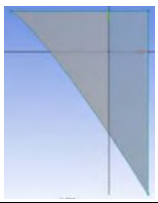	50.01%	52.24%	78.25%
17	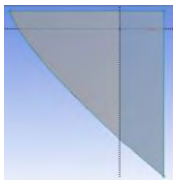	50.21%	53.09%	82.16%	24	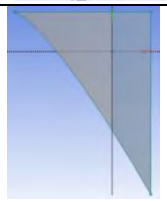	50.02%	52.22%	77.75%
18	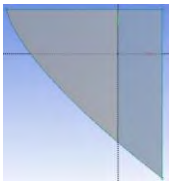	50.20%	53.01%	81.53%	25	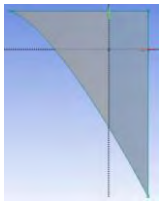	49.98%	52.06%	77.10%
19	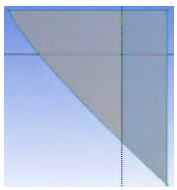	50.18%	52.94%	81.21%	26	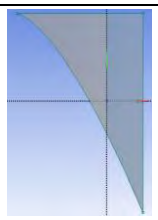	49.94%	51.91%	76.49%
20	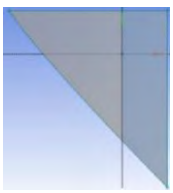	50.13%	52.75%	80.60%	27	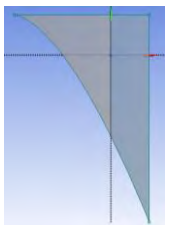	49.91%	51.78%	75.91%
21	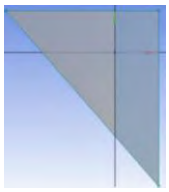	50.10%	52.58%	79.61%	28	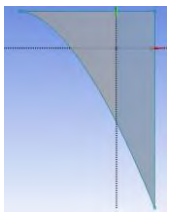	49.89%	51.67%	75.38%

Body No.	Body	λ at T=2.1	λ at T=1.0	λ at T=0.6	Body No.	Body	λ at T=2.1	λ at T=1.0	λ at T=0.6
29	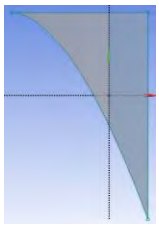	49.96%	51.81%	75.07%	35	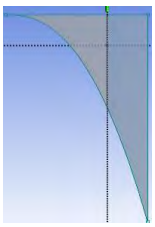	50.11%	51.83%	72.73%
30	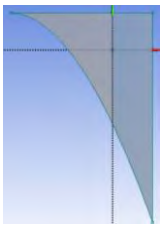	49.96%	51.75%	74.63%	36	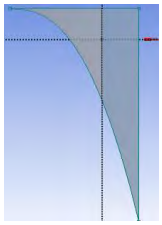	49.24%	50.15%	71.82%
31	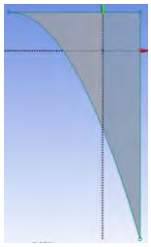	49.97%	51.73%	74.20%	37	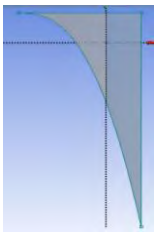	49.24%	49.82%	71.54%
32	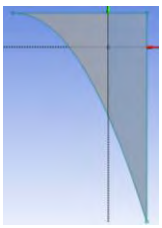	50.00%	51.75%	73.82%	38	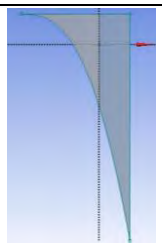	49.10%	49.78%	71.08%
33	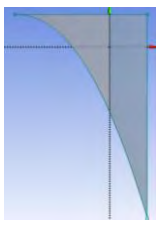	50.06%	51.83%	73.47%	39	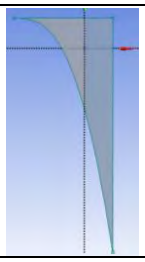	49.08%	49.70%	70.77%
34	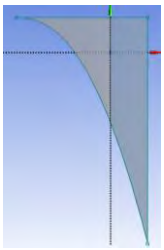	50.12%	51.93%	73.16%					

CHAPTER 5. PROPOSED EXPERIMENTAL SET-UP AND MEASUREMENT

Similar to the numerical model, the diffraction problem can be experimentally studied for a two-dimensional, single, heaving body impinged by linear, regular, harmonic waves. The experimental set-up has been assembled. However, data have not been collected due to time constraints. Therefore, the goal of this chapter is to serve as a guideline for future research in this area.

5.1 Experimental Procedure

The excitation force in the heave direction can be measured using a load cell. The excitation force measured as the body's curved face is positioned toward the wavemaker is denoted as 0°, as seen in Figure 5.1. The excitation force measured as the body's curved face is positioned away from the wavemaker is denoted 180°, as seen in Figure 5.2. The excitation force measured at 0° is used to calculate the radiated wave amplitude at positive infinity using Eq. (58). The excitation force measured at 180° is used to calculate the radiated wave amplitude at negative infinity again using Eq. (58). The maximum power absorption efficiency is calculated with the radiated wave amplitudes at positive and negative infinity using Eq. (79).

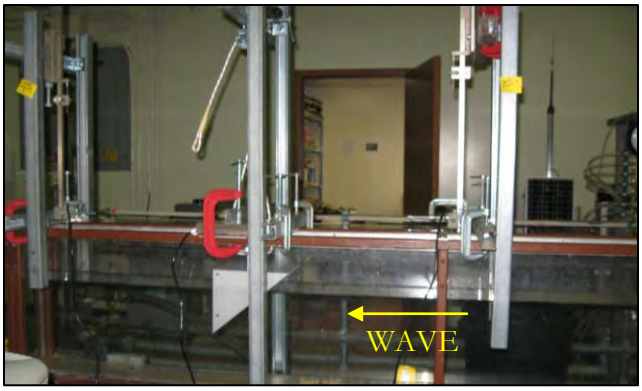

Figure 5. 1 Body Faces Wave Maker (0°)

Figure 5. 2 Body Faces Away from Wave Maker (180°)

Linear, regular, harmonic waves are produced using a computer-controlled wavemaker. The water depth is set to 11 in. (28 cm). Two wave heights are studied: 0.2 in. and 0.8 in., denoted H_1 and H_2, respectively. A wave height of 0.2 in. is considered linear provided the wave conditions are as given in Table 5.1. Comparatively, a wave height of 0.8 in. is considered nonlinear again provided the wave conditions given in Table 5.1. Periods range from 0.6 sec (1.67 Hz) to 1.0 sec (1 Hz) in 0.05 sec intervals. Wave generation lasts 30 sec with a 180 sec rest period between each trial. Additionally the body must span a significant portion of the wavelength for the wave to detect the body's geometry, as seen in Table 5.1.

Note the diffraction parameter and wave slope are comparable to those studied by Koo and Kim (2005). Two wave gages are used to monitor the wave height and frequency.

Table 5. 1 Wave Conditions

T (sec)	f (Hz)	L (in.)	H_1/L	H_2/L	B/L
0.6	1.66	22.0380	0.0091	0.0363	0.2723
0.65	1.54	25.7230	0.0078	0.0311	0.2333
0.7	1.43	29.5550	0.0068	0.0271	0.2030
0.75	1.33	33.4710	0.0060	0.0239	0.1793
0.8	1.25	37.4190	0.0053	0.0214	0.1603
0.85	1.17	41.3630	0.0048	0.0193	0.1451
0.9	1.11	45.2830	0.0044	0.0177	0.1325
0.95	1.05	49.4670	0.0040	0.0162	0.1213
1	1	53.0110	0.0038	0.0151	0.1132

5.2 Experimental Set-up

The wave flume is 32 ft. (9.75m) long and 6 in. (15cm) wide. The first wave gage is approximately 8'-3" from the wavemaker and 1'-6" from the body. The second wave gage is approximately 20'-9"from the end of the wave flume and 1'-6" from the body. Two wave absorbers are placed at the ends of the wave flume to minimize reflection. The set-up is depicted in Figure 5.3. Positioning of the wave gages and body is dictated by the flume's construction and reflection minimization.

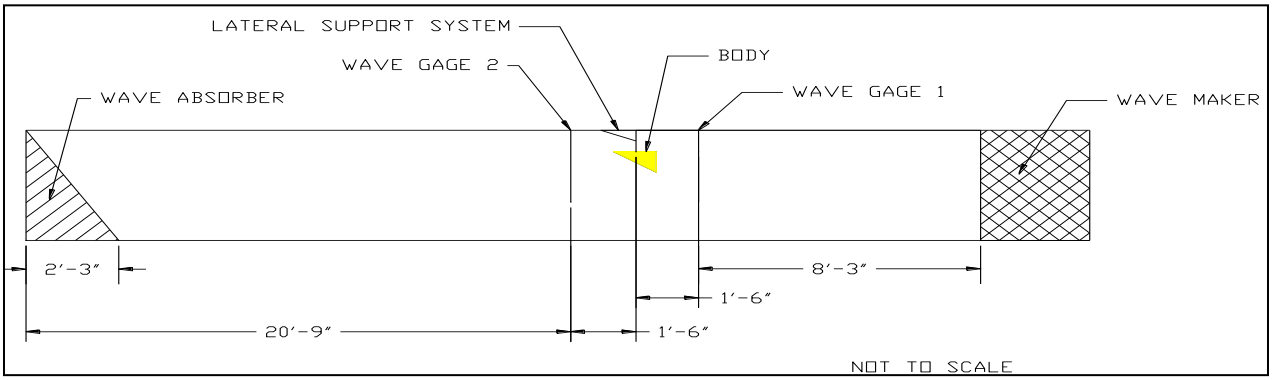

Figure 5. 3 Wave Flume Set-up

The body connects to the aluminum plate by two ½" aluminum rods 2 ½" long, as seen in Figures 5.4 and 5.5. The load cell has #6-32 male threaded studs allowing it to attach to a section of uni-strut above and an aluminum plate below, as seen in Figure 5.5. Aluminum has been used because it is lightweight and quite rigid. Additionally, a lock washer is used between the load cell and uni-strut to prevent rotation. The section of uni-strut is clamped to the top of the wave flume. A lateral support system is included, as seen in Figures 5.5 and 5.6, to dampen horizontal forces that may induce bending moments.

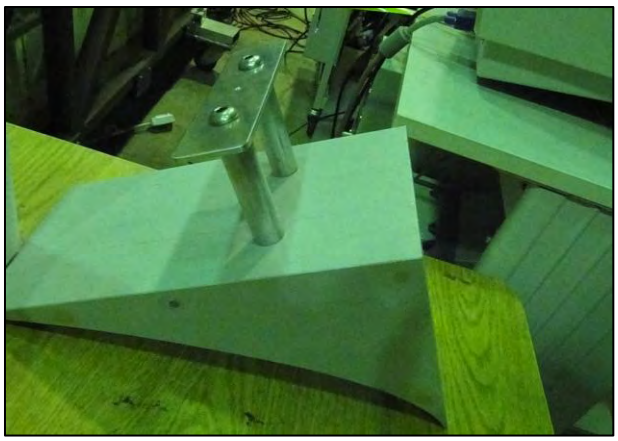

Figure 5.4 Body and Aluminum Rod and Plate Attachment

The lateral support system is constructed of an aluminum arm hinged at 10° to a section of uni-strut clamped to the top of the wave flume. At the end of the aluminum arm, an aluminum foot is hinged. The aluminum foot rests along the aluminum rods attaching the body and load cell. Note the lateral support system only makes surface contact with the aluminum rods.

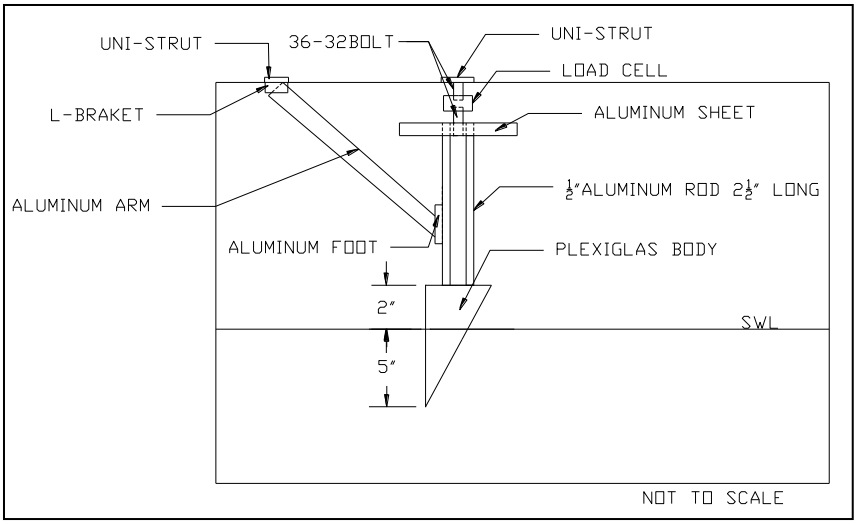

Figure 5. 5 Body Set-up

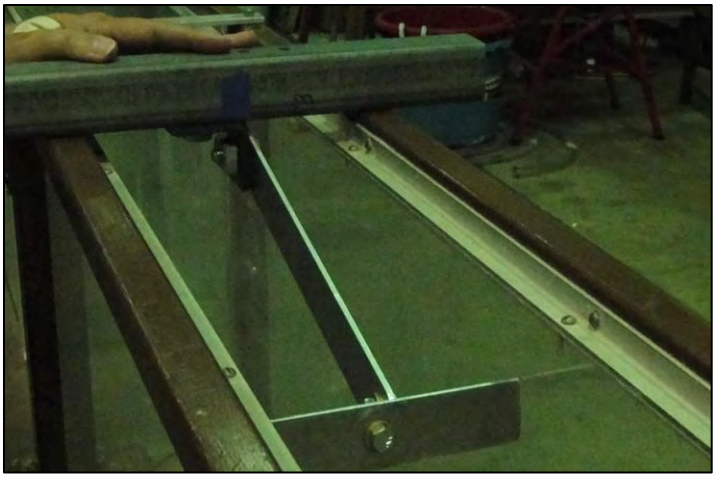

Figure 5. 6 Lateral Support System

5.3 Body Parameters

Thus far three bodies have been constructed. The bodies' widths are 5.875 in. (15 cm), nearly equal to the wave flume width into order to achieve a two-dimensional set-up. A 0.06 in. (0.16 cm) gap exists between the body and wave flume to prevent frictional forces. The bodies have equal drafts of 5 in. (12.7cm) and waterline cross-sectional areas of 35.25 in.^{2} (227cm^2). The bodies are constructed of Plexiglas to resist flexing and corrosion. Plexiglas

also allowed for flexibility in creating bodies with curved faces. In order to reduce weight, the bodies are hollow. To ensure the bodies are waterproof silicon sealant has been applied. The bodies are depicted in Table 5.2, and correspond to numerical bodies 11, 21, and 31, in descending order. To achieve neutral buoyancy, additional weight may be added to the body.

Table 5. 2 Body Parameters

Body	Body Dimensions	Weight* (lbs.)	Volume ($in.^3$)	Buoyancy Force at SWL (lbs.)
	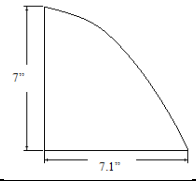	2.3005	194.65 ($3189cm^3$)	4.24
	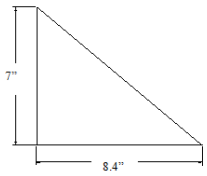	2.0315	172.725 ($2830cm^3$)	3.18
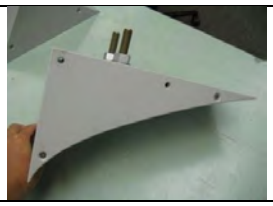	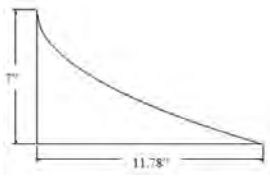	2.2070	161.21 ($2641cm^3$)	2.12

* The weight includes the aluminum rod and plate to attach to the load cell

5.4 Excitation Force Data Collection

The load cell measures the excitation force in the heave direction. A gain is applied to the signal using a signal conditioner so the data acquisition system (DAQ) accurately reads the signal. The DAQ digitizes the signal, so Signal Express can record the signal.

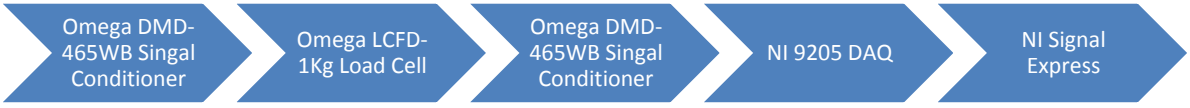

5.4.1 Signal Conditioner and Load Cell

The LCFD-1KG load cell is used to measure the tension and compression forces in the heave direction. The **rated capacity** is 2.2 lbs., with an **ultimate overload** of 300% of the capacity. The load cell is considered IP65, i.e. spray proof, which is sufficient for this experiment. The Omega DMD-465WB signal conditioner supplies the load cell with 5 V of excitation. The signal conditioner is excited via an AC chord connected to terminals 6 and 7. Connect the black and red wires from the load cell to terminals 2 and 4, respectively, as seen in Figure 5.7. Jumper terminals 1 and 2 and terminals 3 and 4 in the signal conditioner, as seen in Figure 5.7. Tune the input voltage by adjusting terminal B, and monitoring the voltage over terminals 2 and 4 using a voltmeter, as seen in Figure 5.8.

The load cell output is 1.5mV/V; this may vary for each particular load cell. The **Combined Linearity and Hysteresis Accuracy** is 0.15% and the **Repeatability** is 0.15%. Thus, the resolution and accuracy measuring a typical excitation force of 0.2 lbs. are:

Resolution

$$(5V)\left(\frac{1.5mV}{1V}\right)\left(\frac{0.2lbs}{2.2lbs}\right) = 0.6818mV$$

Accuracy

$$\varepsilon = \sqrt{0.0015^2 + 0.0015^2} = 0.21\%$$

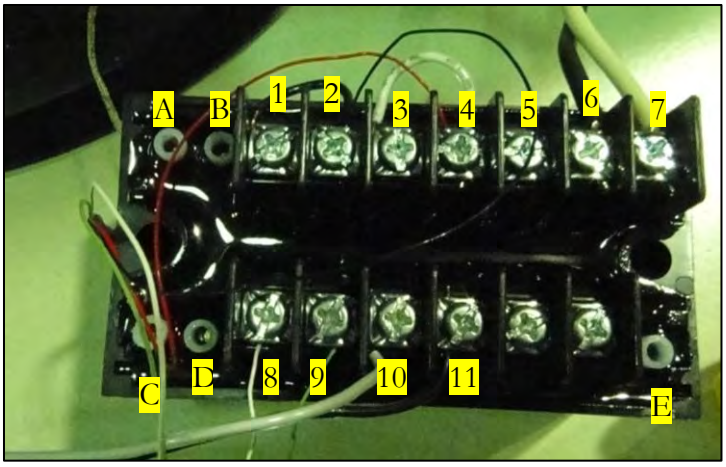

Figure 5. 7 Signal Conditioner

Figure 5. 8 Applying 5V to the Load Cell

The voltage output from the load cell is too small to be accurately read by the DAQ, thus a signal conditioner applies a 250 **gain** to the signal. Thus, the 0.6818mV input from the load cell results in an 170.45mV output. Additionally, the signal conditioner's **time-response** needs to be considered. Recall the wave periods tested range from 1 sec to 0.6 sec, i.e. 1 to 1.167 Hz. The response time is 200 msec to 99% of the final value. The breakpoint is 1 kHz, and then begins to fall at 3dB until 2kHz. Capacitors may be added to the signal conditioner to shift the break point to a lower frequency, in order to filter ambient noise. In addition the load cell may be grounded to metal along the wave flume to reduce noise.

The DMD-465WB signal conditioner offers an **output offset** from -5 to 2V. In order to apply an offset, jumper terminals 8 and 9, and adjust terminals A and E. To monitor the offset adjustment read over terminals 10 and 11 with a voltmeter. After adjusting the offset, remove the jumper between terminals 8 and 9 and adjust the gain. Tune the gain by applying a known weight to the load cell and adjust terminals C and D while monitoring terminals 10 and 11. By monitoring terminals 8 and 9 the user may check the output of the load cell, and monitoring terminals 10 and 11 the output of the signal conditioner.

Data collected indicates the current system will work. The specific output for the load cell was 1.169mV/1V. For a weight of 2.0416 lbs. the expected the load cell output is 5.42mV:

$$(5.0002V)\left(\frac{1.169mV}{1V}\right)\left(\frac{2.0416lbs.}{2.2lbs.}\right) = 5.42mV$$

For this weight the voltmeter read 5.35mV, which has an error of 1.3%.

Note the load cell should be calibrated before experimentation. A suggested method is to raise and lower the water level thereby adjusting the buoyancy force after the body has been set-up and the still water level established. The calibration curve may be calculated from the theoretical buoyancy force and the SignalExpress reading. However, this process introduces error in the accuracy of the water level, and thus error in the accuracy of the buoyancy force.

5.4.2 Data Acquisition System (DAQ)

The NI 9205 DAQ is used to read the signal from the signal conditioner into the computer. The DAQ is connected to the signal conditioner via terminals 10 and 11. The **maximum**

and minimum voltage range of the DAQ is -10/10 V and -0.2/0.2 V, respectively. Thus, the signal of the load capacity, 2.2 lbs., and a typical wave force of 0.2 lbs. fall into the range of the DAQ. Additionally, the DAQ has a **minimum voltage range accuracy** of 0.157mV. Therefore, the DAQ is able to read the signal accurately from a typical excitation force.

5.4.3 SignalExpress

SignalExpress, a data-logging software from National Instruments, is used in this work. SignalExpress projects are comprised of steps; which gather, process, analyze, generate, and store signals. To add a step either: right-mouse click on the left panel, as seen in Figure 5.9; select **Add Step**>> **Acquire Signal** in the tool bar, as seen in Figure 5.10; or select the 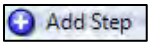

icon from the tool bar to generate a context menu. The initial step is to acquire the signal from the NI 9205 DAQ. Select **Acquire Signal**>> **DAQmx Acquire**>> **Analog Input**>> **Voltage**, as seen in Figure 5.9. Once a step has been added to the project it is indicated in the left panel, as seen in Figure 5.11.

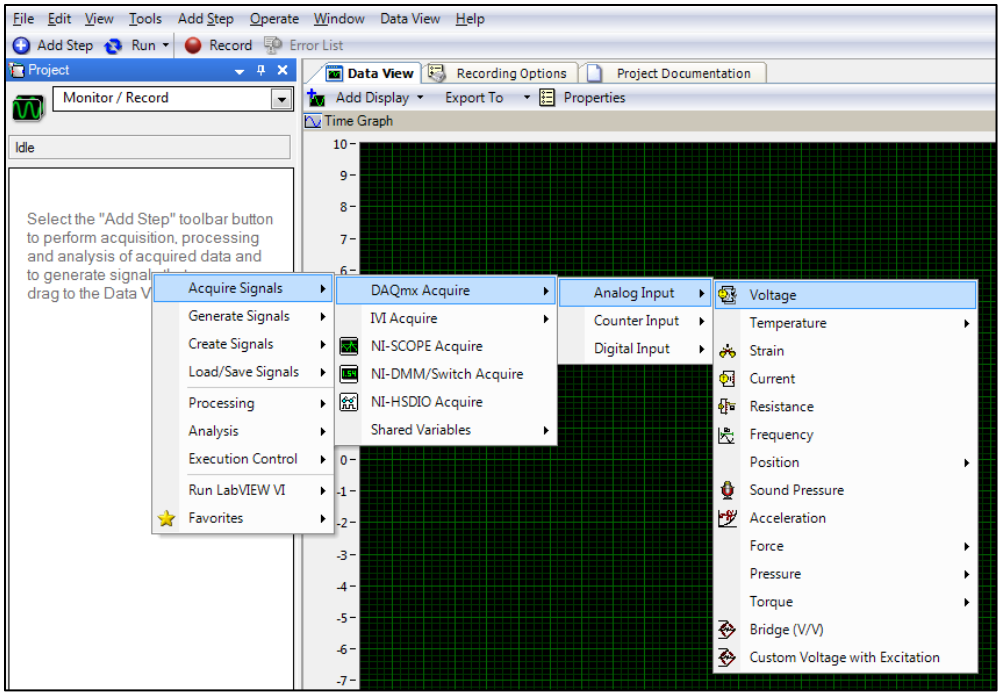

Figure 5. 9 Acquiring Signal Via Right-Mouse Click in Left Panel

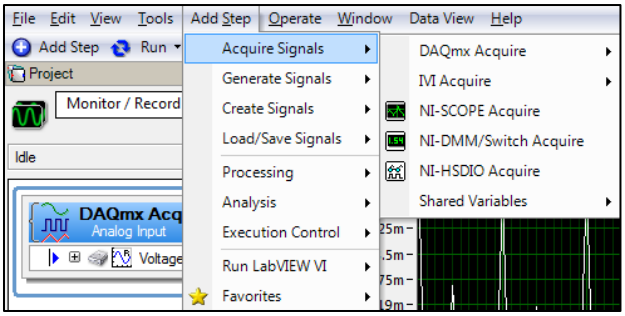

Figure 5. 10 Acquiring Signal Via Add Step Tab

To delete a step highlight the step in the left panel, right-mouse click, and select **Delete**, as seen in Figure 5.11, or select **Edit>> Delete Selected Step**. When deleting steps, be cautious that the step deleted is not an input for a downstream step. The steps will be listed in order of operations in the left panel, i.e. the **Project View**, as seen in Figure 5.11.

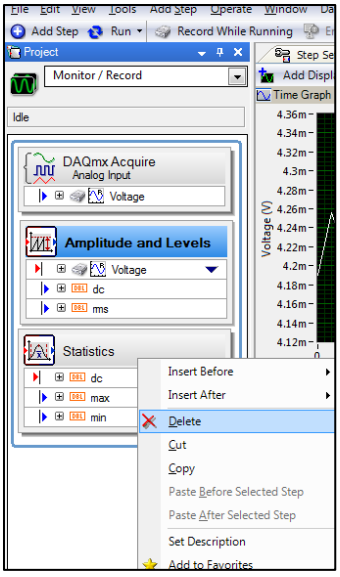

Figure 5. 11 Deleting a Step from Left Panel

Note in Figure 5.11 a blue box is drawn around the multiple steps, i.e. the **Execution Loop**. The Execution loop encloses an **Execution Group**, a group of communicating steps. When a step is added the loop is automatically redrawn to include the new step. To configure a step, highlight it in the left panel and select the **Step Setup** tab. The Step Setup will be further discussed for individual steps.

As stated, the **DAQmx Acquire** step acquires the signal from the 9205 DAQ. The Step Setup tab used to configure the DAQmx Acquire step is presented in Figure 5.12. Set the **Sample Rate** to 100 Hz, **Samples to Read** to 100, and the **Application Mode** to **Continuously**. The **Max** and **Min Input Ranges** are set to 1.875 V and -1.875 V, based on the loaded capacity. The **Scaled Units** is set to **Voltage**, and the **Terminal Configuration** is set to **Differential**. In the **Configuration** tab a **Preview** screen appears, as seen Figure 5.13, allowing the user to view the signal in real time.

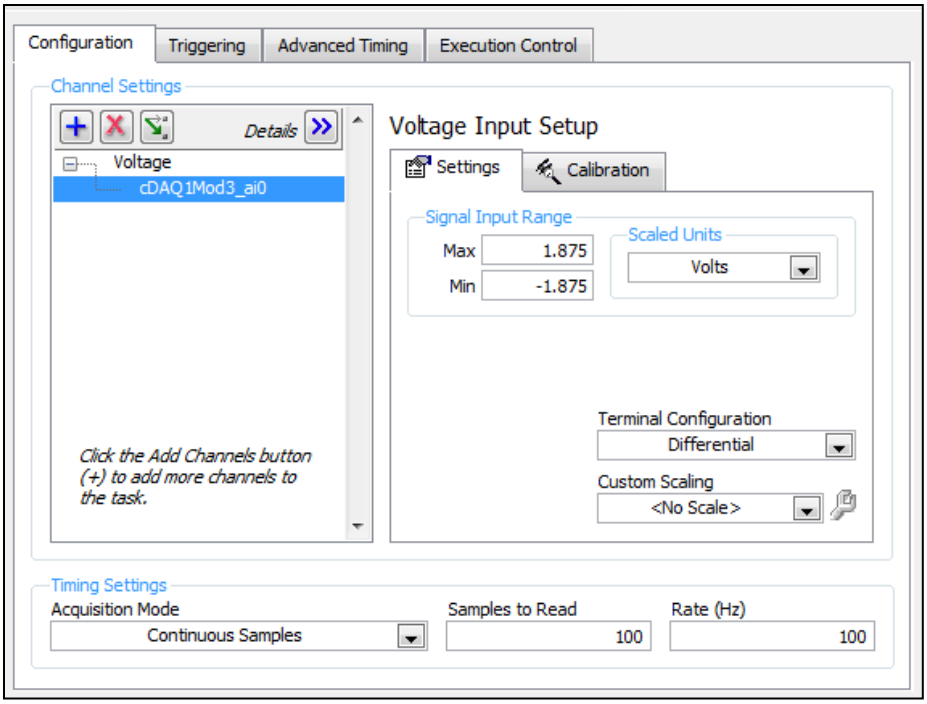

Figure 5. 12 Step Set-up for DAQmx Acquire Step

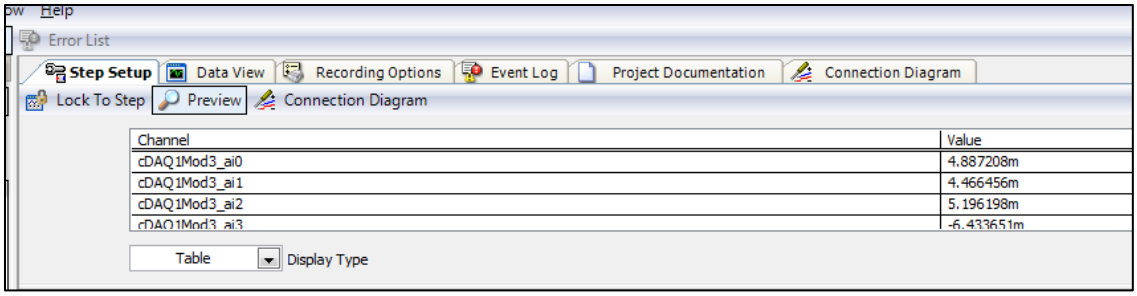

Figure 5. 13 Preview for DAQmx Acquire Step in Table Format

To record data select the **Record Options** tab, highlight **Signal Selection**, and select the steps to be recorded, as seen in Figure 5.14. As a step is added to the project, the user must select it to be recorded in the Record Options tab; it will not be included automatically. Prior to running the program select the 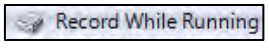

icon in the toolbar.

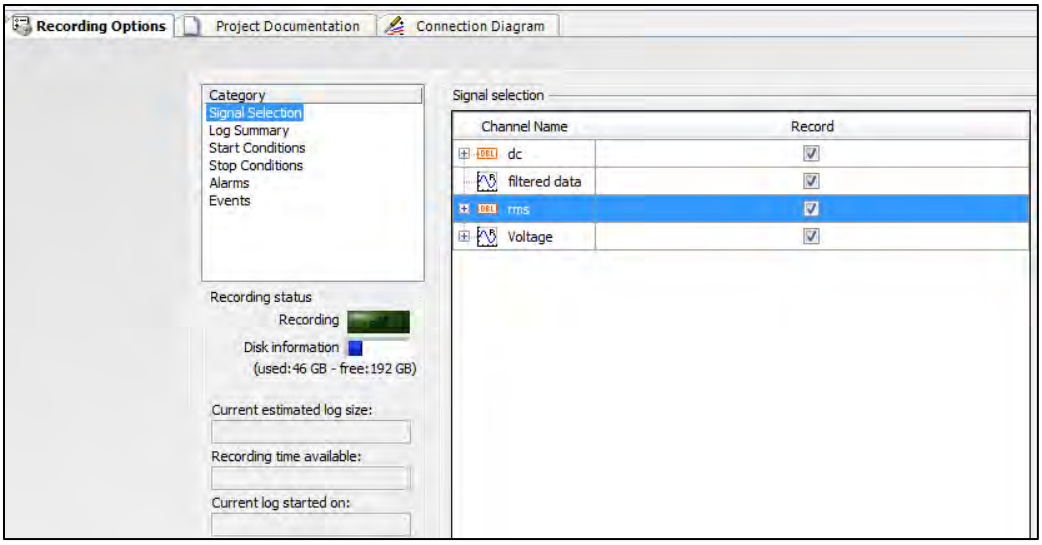

Figure 5. 14 Recording Options, Signal Selection

In the Recording Options tab, select **Log Summary** to name a file in the **Log Title**, as seen in Figure 5.15. The log title will add a counter to the file name for multiple runs. Select the  icon, and input the file's directory.

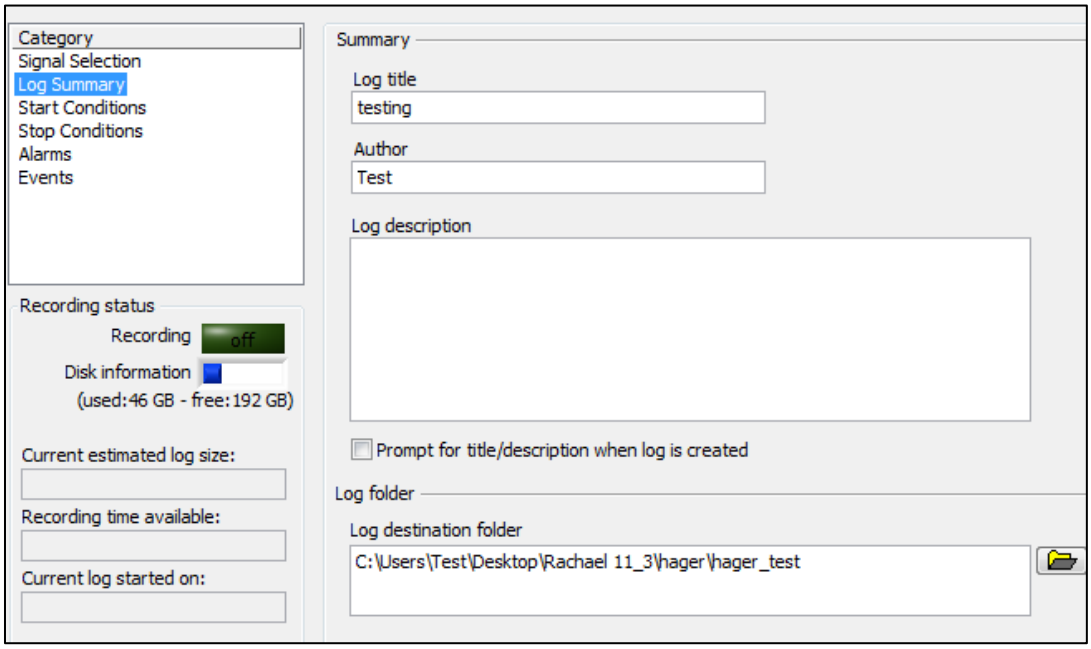

Figure 5. 15 Recording Options, Log Summary

To create graphs and tables select the **Data View** tab. For a desired graph or table, select **Data View>> Add Display**, as seen in Figure 5.16; or expand the 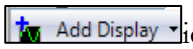

icon. Simply double-clicking the 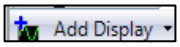

icon will initiate a Time XY graph.

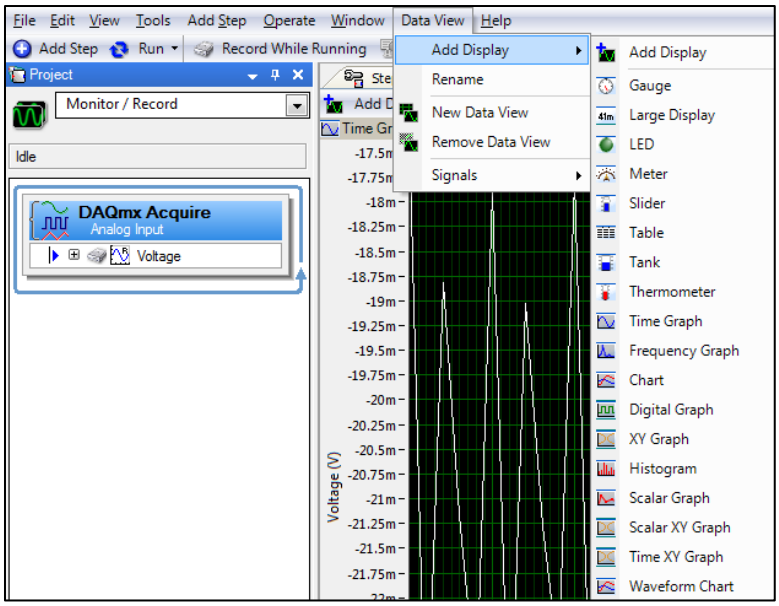

Figure 5. 16 Adding a Graph or Table

In order to select the desired signal for a graph or table, right-mouse click on the graph and select **Signal>> Add Signal,** as seen in Figure 5.17. A window such as the one in Figure 5.18 will appear to select the signal. As steps are created they are not automatically included into graphs or tables; they must be added.

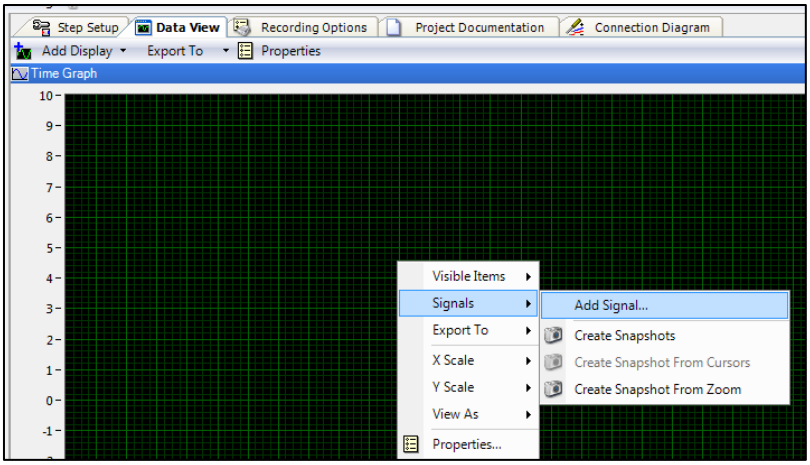

Figure 5. 17 Right-mouse Click on the Graph

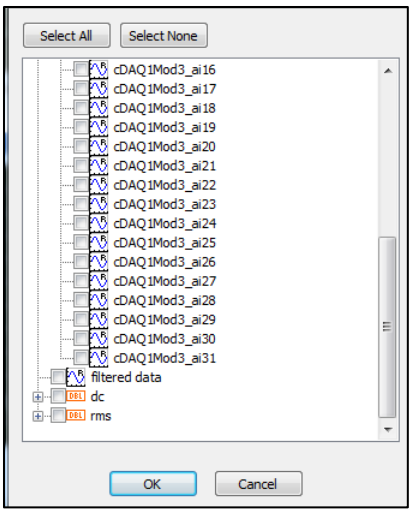

Figure 5. 18 Select Signals Window for a Graph or Table

To change a graph's properties either right-mouse click on the graph and select **Properties** from the context menu, or select **View>> Operator Interface>> Properties**, as seen in Figure 5.19. The X and Y scales may also be altered by right-mouse clicking on the graph, and selecting **X Scale** or **Y Scale**.

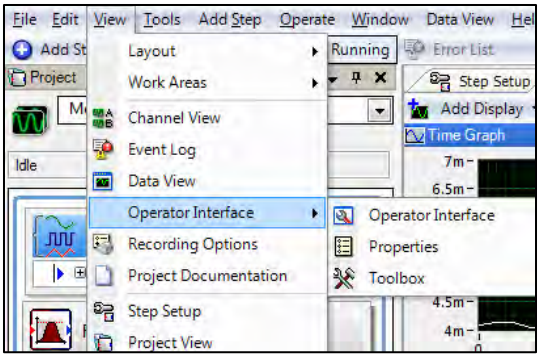

Figure 5. 19 Data View from the Toolbar

SingalExpress has two execution modes **Run** and **Run Once**. Run will executes all steps in the project continuously until it is stopped which is used in this project. To Run SignalExpress either select the 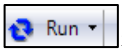

icon or **Operate**>> **Run**, as seen in Figure 5.20. The stop button

will appear in place of the run button as a project runs.

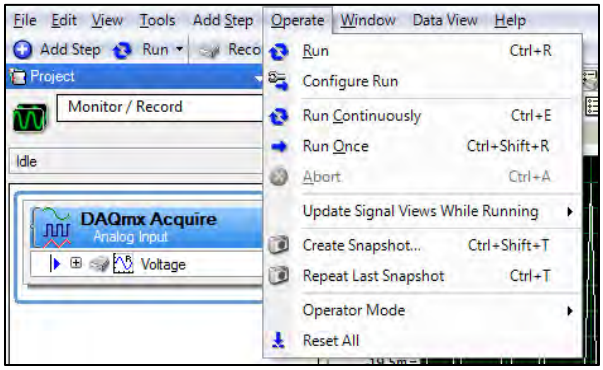

Figure 5. 20 Run and Run Continuously from Operate in the Toolbar

Steps are further categorized as a process or analysis step. To add a Process or Analysis step right-mouse clicking in the left panel and select **Processing** or **Analysis**, respectively, as seen in Figure 5.21. This project uses a Zero-Offset, Filter, and Formula step sequentially.

Zero-Offset

The **Zero-Offset** step removes an offset from the signal. In the **Input/Output** tab select **Export offsets?**, which returns the offset signal as an output. The **Input and Output Signals** graph, as seen in Figure 5.22, displays the input values versus the Zero-Offset values.

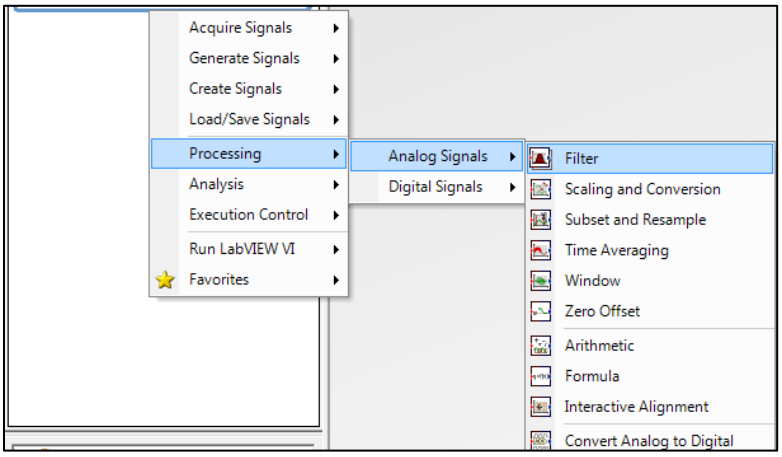

Figure 5. 21 Adding a Process Step

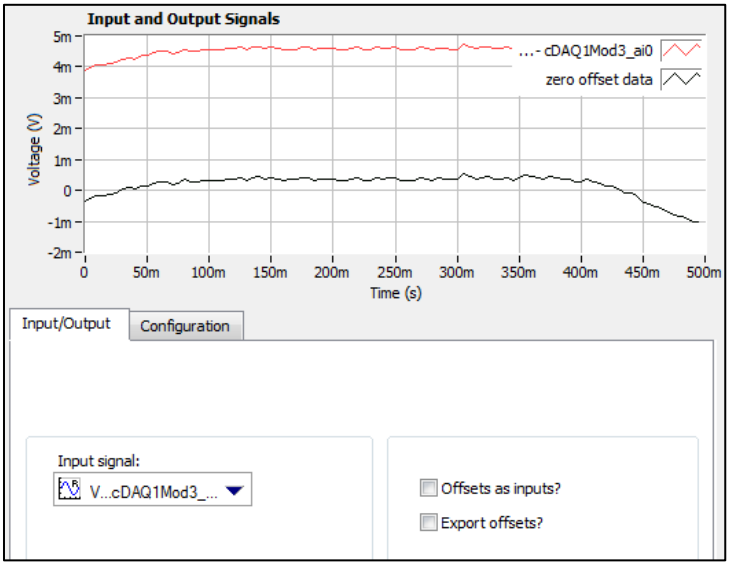

Figure 5. 22 Zero Offset Step Set-up/Output Tab

Set **Setup Type** to **Manual**, as seen in Figure 5.23.Thus, the user approximates the value that will offset the signal. The **Offsets Table** lists the offset for each input signal.

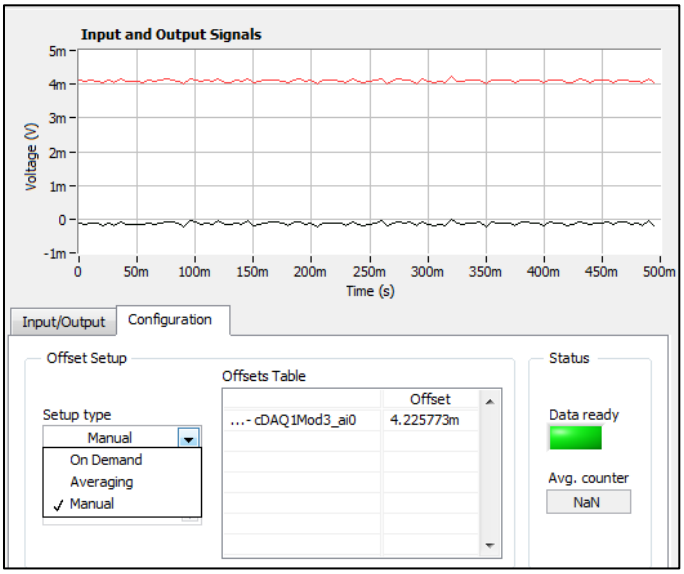

Figure 5. 23 Configuration of Offset

Filter

The **Filter** step continuously attenuates unwanted frequencies from a time signal. Highlight the Filter step in the left panel and select the Step Setup tab prompting a window such as the one seen in Figure 5.24. Under the **Input** tab, select the appropriate channel via **Input Signal>> Voltage>> Voltage>> Zero Offset Data**. Select the **Configuration** tab in the Step Setup prompting a window such as the one seen in Figure 5.24. Set **Mode** to **IIR Filter**, **Type** to **Lowpass**, and **Topology** to **Butterworth**. A lowpass filter attenuates frequencies greater than the lower cutoff. The lower cutoff is set to 2 Hz (0.5 sec) since all incident waves have lower frequencies.

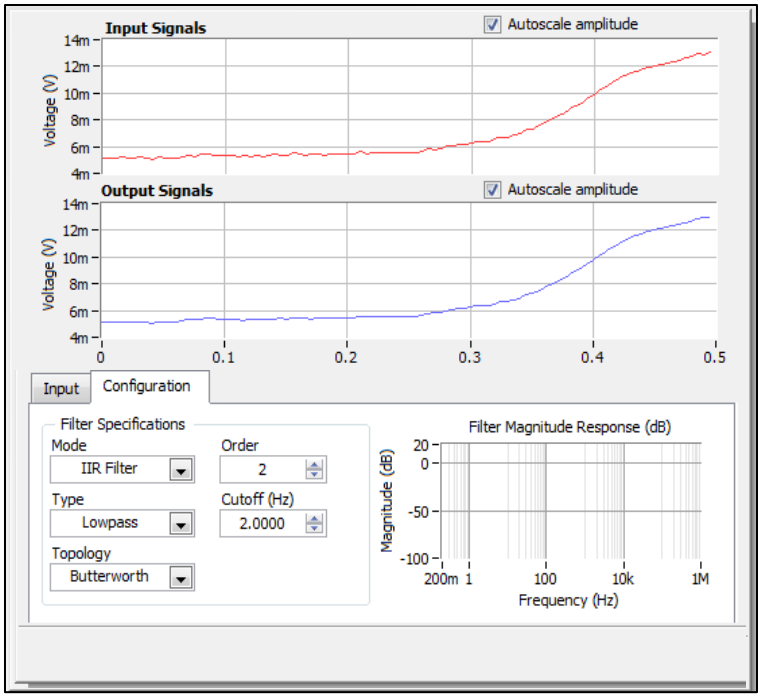

Figure 5. 24 Filter Step Set-up, Configuration Tab

Formula

The **Formula** step is added to the Execution Group so as to apply the calibration curve to the voltage readings for a final output in pounds, as seen in Figure 5.25. The calibration curve applied is based on the following calculation:

$$\frac{\left(\frac{xlbs.}{2.2lbs.}\right)(5V)\left(\frac{1.5mV}{1V}\right)(250)}{1000} = yVolts$$

$$xlbs. * 0.852 = yVolts$$

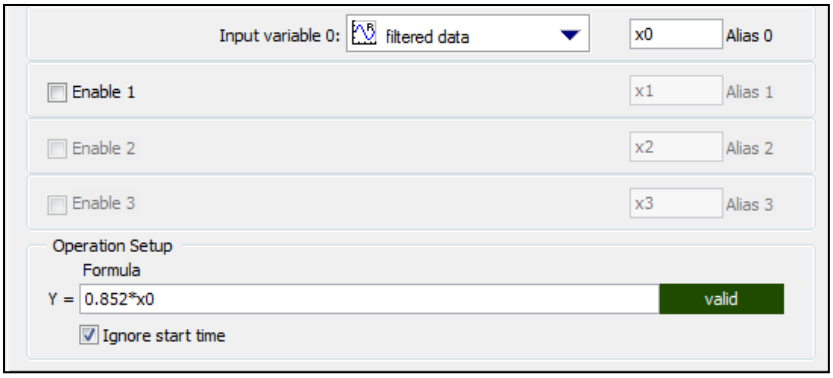

Figure 5. 25 Formula Set-up

5.5 Wave Gage Data Collection

Two wave gages are used to monitor wave heights near the body. The wave gages are connected to two Wheatstone bridge circuits, which are fed a 4.5 V, 2600 Hz, sine wave from an HP 33120A function generator. The circuits are also connected to an AC/DC converter, which digitizes the signal to be read in Labview. The wave gages collect 20 readings per second with a gain of 100, as seen in Figure 5.26. The wave gages are calibrated assuming a linear relationship between 9 water levels and their averaged voltage readings.

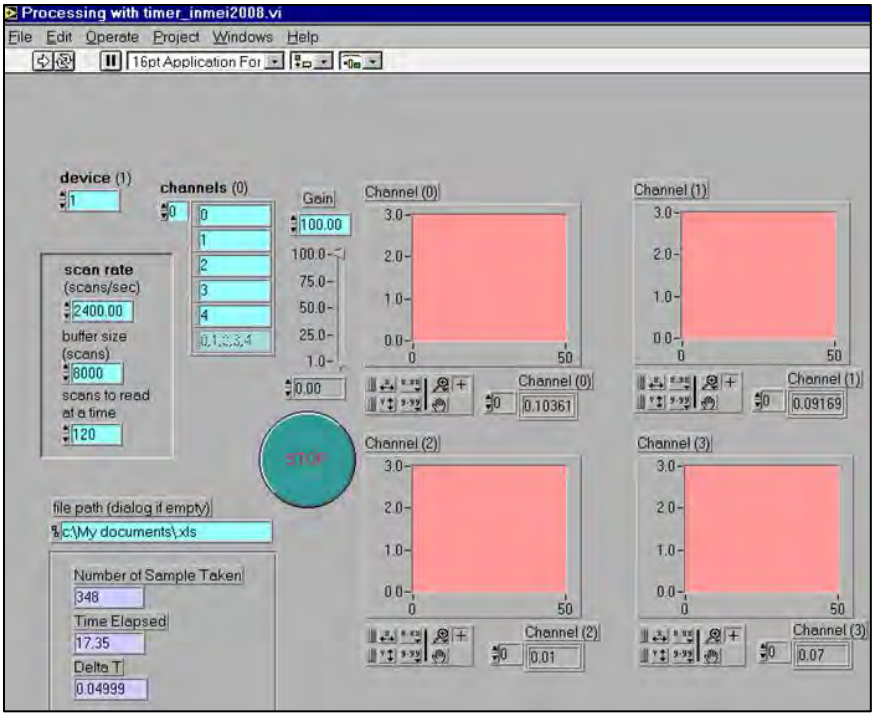

Figure 5. 26 Wave Gage Labview Set-up

5.6 Data Processing

Apply a Fast Fourier Transformation to the time-series force data in order to assess the amplitude of the excitation force. The Matlab code used to apply the Fast Fourier Transformation is given in Appendix B.

5.7 Experimental Validation

Experimental validation should be carried out; Froude scaling the numerical model of Koo and Kim (2005) may be used for this. A Lewis form hull body has been constructed, as seen in Figure 5.27. The Lewis form hull has also been modeled in AQWA, as seen in Figure 5.28. The experimental body has been constructed of acrylic rectangles epoxied together. Perma Oxy is used to prevent seepage. The corners are rounded to reduce turbulence. The body has a width of 5 $^{7}/_{8}$", length of 7 $^{3}/_{8}$", and draft of 3".

Figure 5. 27 Experimental Lewis Form Hull Body

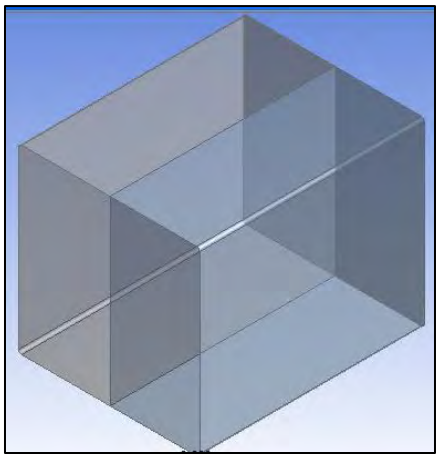

Figure 5. 28 Numerical Model of Lewis Form Hull

Again no data have been collected. It is recommended for future students to carry out the experimental validation before proceeding with the proposed experiment. Future students should begin with the wave conditions given in Table 5.1.

5.8 Experimental Discussion

As mentioned, data have not been collected for the most recent experiment set-up. Again the hope is this chapter will act as a reference for future students in this field.

5.8.1 Experimental Considerations

Originally, an Omega LCCA-25 S-Beam load cell was used. A function generator supplied 15 V to the load cell, which had a rated output of 3 mV/V. For a typical excitation force of 0.2 lbs. the signal output was:

$$(15V)\left(\frac{3mV}{1V}\right)\left(\frac{0.2}{25}\right) = 0.36mV$$

The NI 9212 DAQ was originally used, which has a minimum voltage range accuracy of 0.157 mV, and thus was unable to read the signal accurately. Additionally an S-beam load cell was a poor choice for this set-up because it introduced bending moments. This set-up should not be repeated by future students.

In constructing the bodies, the following was considered: waterproofing, corrosion resistance, weight, flexing resistance, and flexibility in creating curved shapes. Materials considered were Plexiglas, aluminum, Fiberglas cloth hardened with rosin applied to a Styrofoam or wood frame, and a foam sealant poured into a wooden frame. Ultimately, Plexiglas was the most suitable material.

During experimentation, three types of beaches were used to dampen wave reflection from the end of the wave flume: a sand beach, a Plexiglas sheet with a 1:10 slope, and foam wave absorber. The foam wave absorber has performed the best as expected.

5.8.2 Environmental Sources of Error

To detect the effects of geometry on maximum power absorption efficiency the body must span a significant portion of the wavelength. With the body dimensions introduced in Chapter 5.5 periods greater than 1 sec are too long to detect the body's shape. However, linear theory pertains to waves where H<< L. Thus, small wave amplitudes are desired; however, the wave maker is less accurate when producing smaller wave amplitudes. Thus, the user must monitor the actual wave heights produced.

The flume's construction also presents errors. The depth and width fluctuates along the flume. The flume also leaks, which is amplified with greater water depth, such as that used in this work. Finally, as mentioned, reflection from the walls of the wave flume introduces error.

Ambient and internal noise also present error. In order to minimize ambient noise: ground the load cell, apply capacitors to the signal conditioner, and minimize electronic use during experimentation. To minimize internal noise use high grade wire to jumper terminals on the signal conditioner.

5.8.3 Suggestions for Future Research

For future research, it is suggested to create larger bodies, thus allowing longer waves and greater wave heights. Thus, the wavemaker will be able to more accurately create the desired wave, and greater excitation forces will be experienced by the body. Large bodies would present a greater risk in breaking the load cell while being attached. Therefore, it is suggested one uses two load cells and superimpose the forces measured, or measure the excitation force with a different system, such as a laser system. Additionally, future points to be studied include whether the submerged volume or waterline cross-sectional area should remain constant, the effects of a three-dimensional body on maximum power absorption efficiency, the effects of the body moving with various degrees of freedom, the effects of multiple bodies interacting, and the applicability to the Hawaiian coast.

B_{ij} for a Two-Dimensional, Single, Heaving Body

At the Free-Surface

$$\eta = -\frac{1}{g}\frac{\partial \Phi}{\partial t} = \frac{i\omega\phi}{g}$$

$$\frac{\partial \phi}{\partial z} = \frac{\partial \eta}{\partial t} = i\omega\eta = \frac{\omega^2\phi}{g}$$

$$\iint \left(\phi \frac{\partial \psi}{\partial n} - \psi \frac{\partial \phi}{\partial n} \right) dl \to \frac{\omega^2}{g}\phi\psi - \frac{\omega^2}{g}\phi\psi = 0$$

At the Body

$$\iint_S \left\{ \frac{\partial \bar{\phi}_R}{\partial n}\phi_R - \frac{\partial \phi_R}{\partial n}\bar{\phi}_R \right\} dS$$

$$\frac{\partial \phi_R}{\partial n} = i\omega n_z \quad \text{and} \quad \frac{\partial \bar{\phi}_R}{\partial n} = -i\omega n_z$$

$$\iint_S \left\{ (-i\omega n_z)\phi_R - (i\omega n_z)\bar{\phi}_R \right\} dS$$

$$-i\omega \iint_S (\phi_R + \bar{\phi}_R) n_z dS = -i\omega 2 \iint_S \Re\{\phi_R\} n_z dS$$

By definition,

$$B_{ij} = \rho \Re\left\{ \iint \phi_R n_z dl \right\}$$

$$-i\omega 2 \iint R\{\phi_R\} n_z dl = \frac{-i\omega 2 B_{ij}}{\rho}$$

At +∞

$$\phi_{R,x\to+\infty} = \frac{-\alpha_+ ig}{\omega}\frac{\cosh(k(z+d))}{\cosh(kd)}e^{-ikx}$$

$$\bar{\phi}_{R,x\to+\infty} = \frac{\bar{\alpha}_+ ig}{\omega}\frac{\cosh(k(z+d))}{\cosh(kd)}e^{ikx}$$

$$\frac{\partial \phi_{R,x\to+\infty}}{\partial n} = -\frac{\alpha_+ kg}{\omega}\frac{\cosh(k(z+d))}{\cosh(kd)}e^{-ikx}$$

$$\frac{\partial \bar{\phi}_{R,x\to+\infty}}{\partial n} = -\frac{\bar{\alpha}_+ gk}{\omega}\frac{\cosh(k(z+d))}{\cosh(kd)}e^{ikx}$$

Applying Gauss' Theorem

$$\int_{-d}^{0}\left\{\frac{\partial \bar{\phi}_R}{\partial n}\phi_R - \frac{\partial \phi_R}{\partial n}\bar{\phi}_R\right\}dz$$

$$= \int_{-d}^{0}\left(\frac{2|\alpha_+|^2 ig^2 k}{\omega^2}\frac{\cosh^2(k(z+d))}{\cosh^2(kd)}\right)dz$$

$$= \frac{2|\alpha_+|^2 ig^2}{\omega^2}\frac{\tanh(kd)}{2}\left(1+\frac{2kd}{\sinh(2kd)}\right)$$

$$= \frac{2|\alpha_+|^2 igC_g}{\omega}$$

At -∞

$$\phi_{R,x\to-\infty} = \frac{-\alpha_- ig}{\omega}\frac{\cosh(k(z+d))}{\cosh(kd)}e^{ikx}$$

$$\bar{\phi}_{R,x\to-\infty} = \frac{\bar{\alpha}_- ig}{\omega}\frac{\cosh(k(z+d))}{\cosh(kd)}e^{-ikx}$$

$$\frac{\partial \phi_{R,x\to-\infty}}{\partial n} = \frac{\alpha_- gk}{\omega}\frac{\cosh(k(z+d))}{\cosh(kd)}e^{ikx}$$

$$\frac{\partial \bar{\phi}_{R,x\to-\infty}}{\partial n} = \frac{\bar{\alpha}_- gk}{\omega}\frac{\cosh(k(z+d))}{\cosh(kd)}e^{-ikx}$$

Applying Gauss' Theorem

$$= \int_{-\infty}^{0}\left(\frac{2|\alpha_-|^2 ig^2 k}{\omega^2}\frac{\cosh^2(k(z+d))}{\cosh^2(kd)}\right)dz$$

$$= \frac{2|\alpha_-|^2 ig^2}{\omega^2}\frac{\tanh(kd)}{2}\left(1+\frac{2kd}{\sinh(2kd)}\right)$$

$$= \frac{2|\alpha_-|^2 igC_g}{\omega}$$

Summing Components

$$0 = 0 + \frac{i\omega 2B_{ij}}{\rho} + \frac{2|\alpha_+|^2 igC_g}{\omega} + \frac{2|\alpha_-|^2 igC_g}{\omega}$$

$$B_{ij} = \frac{\rho g C_g}{\omega^2}\left(|\alpha_+|^2 + |\alpha_-|^2\right)$$

X_i for a Two-Dimensional, Single, Heaving Body

$$X_i = -\rho \iint_S \left(\phi_R \frac{\partial \phi_I}{\partial n} - \phi_I \frac{\partial \phi_R}{\partial n}\right) dS$$

$$\phi_I = \frac{-gAi}{\omega}\frac{\cosh(k(z+d))}{\cosh(kd)} e^{ikx}$$

$$\phi_R = \frac{-g\alpha_+ i}{\omega}\frac{\cosh(k(z+d))}{\cosh(kd)} e^{-ikx}$$

$$\frac{\partial \phi_I}{\partial n} = \frac{\partial \phi_I}{\partial x} = \frac{gAk}{\omega}\frac{\cosh(k(z+d))}{\cosh(kd)} e^{ikx}$$

$$\frac{\partial \phi_R}{\partial n} = \frac{\partial \phi_R}{\partial x} = \frac{-g\alpha_+ k}{\omega}\frac{\cosh(k(z+d))}{\cosh(kd)} e^{-ikx}$$

$$X_i = -\rho \int_{-d}^{0} \frac{-2iA\alpha g^2 k}{\omega}\frac{\cosh(k(z+d))}{\cosh(kd)} dz$$

$$X_i = \frac{2\rho A\alpha_+ g^2 ki}{\omega^2}\frac{\tanh(kd)}{2}\left(1 + \frac{2kd}{\sinh(2kd)}\right)$$

$$C_g = \frac{g}{2\omega}\tanh(kd)\left(1 + \frac{2kd}{\sinh(2kd)}\right)$$

$$|X_i| = \frac{2\rho A\alpha_+ gC_g i}{\omega}$$

Proof M_{ij} and B_{ij} are Symmetric Tensors

Recall Green's 2nd Identity

$$0 = \int_S \left(\phi_j \frac{\partial \phi_i}{\partial n} - \phi_i \frac{\partial \phi_j}{\partial n} \right) dS$$

$$\int_S \phi_j \frac{\partial \phi_i}{\partial n} dS = \int_S \phi_i \frac{\partial \phi_j}{\partial n} dS$$

Recall

$$M_{ij} = \rho \int_S \phi_i \frac{\partial \phi_j}{\partial n} dS \quad \text{And} \quad M_{ji} = \rho \int_S \phi_j \frac{\partial \phi_i}{\partial n} dS$$

Thus, it is clear M_{ij} is a symmetric tensor. Similarly, recall

$$B_{ij} = \rho\omega \int_S \phi_j \frac{\partial \phi_i}{\partial n} dS \quad \text{And} \quad B_{ji} = \rho\omega \int_S \phi_i \frac{\partial \phi_j}{\partial n} dS$$

Thus, it is also clear B_{ij} is a symmetric tensor.

APPENDIX B: FAST FOURIER TRANSFORM MATLAB CODE

```
% Read in Force Data

newData1 = importdata('Data Sheet_4_19_12_body3_180deg_wc1to18.txt', '\t');

% Data Processing for the truncated set

% note this is for only one trial, for multiple trials the code must be
% modified
trial1 = newData1(2000:1:3000,1);
trial2 = detrend(trial1);

dt1t = 1/100; % [s] time step of data
tend1t = length(trial1)*dt1t; %[s] length of time signal
F_s1t = 1/dt1t; %[Hz] Sample rate of data
t1t = 0:dt1t:tend1t-dt1t; % [s] length of trials


trial3 = fftshift(trial2);
trial4_fftt = abs(trial3);
trial5_fftt = max(trial4_fftt)

Nt = length(trial4_fftt);


t1t2 = length(trial1)*dt1t; % total length of time series
fr = 1-1/t1t2;


plot(fr,trial4_fftt);
```

BIBILIOGRAPHY

ANSYS. (n.d.). ANSYS AQWA User's Manual. Canonsburg, PA: ANSYS Inc., 2010.
ANSYS. (n.d.). ANSYS Workbench User's Manual. Canonsburg, PA: ANSYS Inc., 2010.
ANSYS. (n.d.). AQWQ LINE Manual United Kingdom: ANSYS Inc., 2010.
Backer, G. D. (2009). Hydrodynamic Design Optimization of Wave Energy Converters Consisting of Heaving Point Absorbers Ph.D. Thesis. University of Ghent.
Bedard, R. a. (n.d.). *Offshore Wave Energy Conversion Devices. E2I EPRI.* Retrieved from http://www.energy.ca.gov/oceanenergy/E2I_EPRI_REPORT_WAVE_ENERGY.PDF.
Bergdahl, L. C. (1979). Wave Energy in Swedish Waters . *Symposium on Ocean Wave Energy Utilization*, (pp. 222-252).
Brooke, J. (2003). *Wave-Energy Conversion.* Oxford: Elsevier Science Ltd.
Budal, K. (1977). Theory for Absorption of wave Power by a System of Interacting Bodies . *Journal of Ship Research 21(4)*, 248-253.
Budal, K. a. (1975). A Resonant Point Absorber of Ocean-Wave Power. *Nature 256*, 478-479.
Budal, K. a. (1977). Optimum Operation of Improved Wave-Power Converter. *J. Marine Science Communication 3(2)*, 133-150.
Budal, K. a. (1978). Wave-Power Conversion by Point Absorbers. *Norweigan Maritime Research 6(4)*, 2-11.
Budal, K. Falnes,J. Kyllingstad,A. and Oltedal, G. (1979). Experiments with Point Absorbers. *Symposium on Ocean Wave Energy Utilization*, (pp. 253-280).
Callaway, E. ". (2007). To Catch a Wave . *Nature 450 (8)*, 156-159.
Campus, A. (n.d.). *http://www.jeron.je/anglia/learn/sec/science/sn005/page02.htm.* Retrieved from Energy from the Sea.
Carter, R. (2005). *Wave Energy Converters and a Submerged Horizontal Plate* . Master's Thesis, University of Hawaii.
Clément, A. M. (2002). Renewable Sustainable Energy Review. *Wave Energy in Europe: Current Status and Perspectives 6(5)* , 405-431.
Cohen, K. a. (2008). *Fluid Mechanics.* Elsevier Inc.
Cruz, J. (2008). *Ocean Wave Energy: Current Status and Future Perspectives* . Springer-Verlag .
DesignModeler User's Manual. Canonsburg, P. A. (n.d.).
Drew, B. P. (2009). A Review of Wave-Energy Converter Technology. *Journal of Power and Energy 223*, 887-902.
Ertekin, C. (2012). ORE 609 Hydrodynamics of Fluid-Body Interaction .
Ertekin, R., Wang, S., Che, X., & and Riggs, H. (1995). On the Application of the Haskind-Hanaoka Relations. *Marine Structures*, 617-629.
Evans, D. (1976). A Theory for Wave-Power Absorption by Oscillating Bodies . *Journal of Fluid Mechanics 77(1)* , 1-25.
Evans, D. (1979). Some Theoretical Aspects of Three-Dimensional Wave-Energy Absorbers . *Symposium on Ocean Wave Energy Utilization*, (pp. 78-112).
Evans, D. (n.d.). Theory for Wave Power Absorption by Oscillating Bodies . *Proc. 11th Symposium Naval Hydrodynamics.* London.
Falcão, A. (2010). Renewable Sustainable Energy Review. *Wave Energy Utilization: A Review of the Technologies 14*, 899-918.
Falnes, J. (2007). A Review of Wave Energy Extraction. *Marine Structures 20*, 185-201.

Feasibility of Developing Wave Power as a Renewable Energy Resource for Hawaii. (n.d.). Retrieved 7/29/2011, from Department of Business Economic Development, and Tourism: http://hawaii.gov/dbedt/info/energy/publications/wavereport02.pdf
Fujita, R. a. (2002). Renewable Energy from the Ocean. *Marine Policy 26*, 471-479.
Glasgow, U. o. (2002, 5). *http://www.esru.strath.ac.uk*. Retrieved from Wave Power.
Inc., W. P. (2010, 2 1). *http://ikionrenewableenergy.wordpress.com/category/uncategorized/*. Retrieved from Ocean Energy Classification.
Koo, W.C. and Kim,M.H. (2007). Fully nonlinear wave-body interactions with surface-piercing bodies. *Ocean Engieenering*, 1000-1012.
Ltd., W. (2012, 3 23). *http://www.wavegen.co.uk/contact.htm*. Retrieved from Voith Hyrdro Wavegen Limpet.
MacKay, D. j. (2009). *http://www.inference.phy.cam.ac.uk/sustainable/book/tex/cft.pdf*. Retrieved from Sustainable Energy without the Hot Air .
Maruo, H. (1960). On the Increase of the Resistance of a Ship in Rough Seas. *Journal of Zosen Kiokai*.
McCormick, M. and Ertekin, R.C. (2009, May). Renewable Sea Power. *Mechanical Engineering* , ASME,
McGrath, J. H. (2012). *http://science.howstuffworks.com*. Retrieved from How Wave Energy Works.
Mei C.C. and Newman, J. (1979). Wave Power Extraction by Floating Bodies. *Symposium on Ocean Wave Energy Utilization*, (pp. 1-28).
Mei, C. (1976). Power Extraction from Water Waves. *Journal of Ship Research 20(2)*, 63-66.
Mei, C. C. (1989). *The Applied Dynamics of Ocean Surface Waves*. World Scientific.
Newman, J. (1962). The Damping of an Oscillating Ellipsoid Near a Free Surface. *Journal of Ship Research 5(3)*, 10-17.
Newman, J. (1962). The Exciting Forces on Fixed Bodies in Waves. *Journal of Ship Research*, 10-17.
Newman, J. (1977). *Marine Hydrodynamic*. M.I.T Press.
Nihous, G. (2011). ORE 677 Marine Renewable Energy.
Nojiri, N. a. (1975). A Study on the Drift Force on Two-Dimensional. *Transactions of the West-Japan Society Naval Architect* , 131-152.
OcraFelx User Manual Version 9.4a. Daltongate, C. U. (n.d.).
Panagiotopoulos, J. a. (n.d.). *Ocean Energy Glossary*. Retrieved 29 7, 2011, from Wave Energy Centre: http://www.oreg.ca/web_documents/ocean_energy_glossary_dec_2007.pdf
Price, A. (2009). *New Perspectives on Wave Energy Converter Control* . Ph.D. Thesis, University of Edinburgh .
Rahman, M. (1995). *Water Waves*. Oxford Science Publications.
Ross, D. (1995). *Power from the Waves*. Oxford: Oxford University Press.
Salter, S. (1974). Wave Power. *Nature 249*, 720-723.
Shaw, R. (1982). *Wave Energy: A Design Challenge*. Chichester: Ellis Horwood.
Suzuk, G. a. (n.d.). Estimation of Incident and Reflected Waves in Random Wave Experiments. *Proc. 15th Coastal Engineering Conference*. Hawaii.
Tanizawa, K. and Minami, M. (1998). On the Accuracy of NWT for Radiation and Diffraction Problem. *6th Symposium on Nonlinear and Free-Surface Flow*.
Thorpe, T. (1999). *A Brief Review of Wave-Energy*. The UK Department of Trade and Industry.

Trust, C. (2011). *Capital, Operating, and Maintenance Costs*. Retrieved from Carbon Trust: http://www.carbontrust.co.uk/SiteCollectionDocuments/Various/Emerging%20technologies/Technology%20Directory/Marine/cost%20of%20energy/Capital,%20operating%20and%20maintenance%20costs.pdf

Vantorre, B. a. (2004). Modeling of Hydraulic Performance and Wave-Energy Extraction by a Point Absorber in Heave. *Applied Ocean Research 26*, 61-72.

Vincent, Z. D. (2002, 4 30). *Water Wave Mechanics EM 1110-2-1100 (PartII)*. Retrieved 7 20, 2011, from http://www.marine.tmd.go.th/Part-II-Chap1.pdf